International Journal of Antennas and Propagation

5G MIMO Antenna Design and Integration in Futuristic Wireless Devices

Lead Guest Editor: Chow-Yen-Desmond Sim
Guest Editors: Abdullah Alharbi, Jayshri Kulkarni, and Ravi Kumar Gangwar

5G MIMO Antenna Design and Integration in Futuristic Wireless Devices

International Journal of Antennas and Propagation

5G MIMO Antenna Design and Integration in Futuristic Wireless Devices

Lead Guest Editor: Chow-Yen-Desmond Sim
Guest Editors: Abdullah Alharbi, Jayshri Kulkarni, and Ravi Kumar Gangwar

Chief Editor

Associate Editors

Academic Editors

Contents

Hindawi
International Journal of Antennas and Propagation
Volume 2024, Article ID 2945195, 15 pages
https://doi.org/10.1155/2024/2945195

Research Article

Design of Microstrip Antenna Arrays with Rotated Elements Using Wilkinson Power Dividers for 5 G Customer Premise Equipment Applications

Ting-Yi Huang and Yun-Jhang Lee

Department of Electrical Engineering, Feng Chia University, Taichung 407102, Taiwan

Correspondence should be addressed to Ting-Yi Huang; tyihuang@fcu.edu.tw

Received 13 September 2022; Revised 19 March 2024; Accepted 23 March 2024; Published 12 April 2024

Academic Editor: Hervé Aubert

Microstrip antenna arrays are proposed in this paper for the customer premise equipment (CPE) applications in the frequency range 1 (FR1) of the 5th generation (5 G) mobile networks. The proposed antenna arrays consist of three FR4 substrates. Antenna elements and feeding networks are optimized separately through parameter studies and then combined to form the proposed antenna arrays. Bandwidth-enhancing parasitic elements on the top substrate are broadside coupled to the microstrip antennas in the middle substrate, which are probe-fed by the microstrip feeding network using Wilkinson power dividers realized in the bottom substrate through the ground plane and the stud supporting air layer between the lower two substrates. Two antenna arrays, with four and eight antenna elements, are proposed for different gain specifications, 10 dBi and 12 dBi, respectively. Bandwidths of 10-dB return loss for both arrays fully covered the 5 G n78 frequency band (3.3–3.8 GHz). 20 dB isolation between antenna elements can also be achieved using the proposed layouts with rotated elements. The dimensions, radiation gain, and efficiency of the proposed antenna units, four-element array, and eight-element array are $65 \times 65 \times 11.4$, $115 \times 115 \times 11.4$, and $115 \times 215 \times 11.4$ mm^3, 6.2, 10.5, and 13 dBi, 74%, 56%, and 50%, respectively. The proposed antenna arrays exhibit the advantages of simple, low-cost, low-profile, and high-gain characteristics, which is potentially applicable to 5 G CPE outdoor unit (ODU)-related devices.

1. Introduction

The development of wireless communication systems has progressed rapidly in recent decades. The fifth generation new radio (5 G NR) system has been proposed to further enhance the bandwidth and capacity of the mobile communication system, including three major application scenarios defined as enhanced mobile broadband (eMBB), massive machine-type communications (mMTCs), and ultrareliable and low-latency communications (uRLLCs). To achieve the bandwidth enhancement, higher operation frequency bands were introduced, such as those in the sub-6 GHz frequencies (frequency range 1, FR1) or those in the even higher millimeter-wave frequencies (frequency range 2, FR2). On the other hand, capacity expansion is accomplished by smaller cell sizes that reduce the power of base stations to make frequency reuse more efficient and flexible. Compared to predecessor systems, the density of base stations in 5 G is significantly increased to complete the coverage of a certain area. The concept of customer premises equipment (CPE) is then proposed to ease the distribution of base stations, especially in metropolitan areas, by introducing customized, flexible, low-cost, and high bandwidth outdoor and/or indoor units (ODUs/IDUs) that bridge/route the 5 G mobile signals and the wireless local area networks (WLANs) without the need for wired connection.

A wide range of antennas and arrays can be found in the literature that are suitable for 5 G FR1 CPE ODU applications. Dual polarized antennas and arrays in the sub-6 GHz frequency bands can be used in cross polarized uplink/downlink configurations [1–4]. A 3–4.6 GHz dual

polarization antenna has been proposed using two orthogonal magneto-electric dipole antennas with an L-shaped feeding structure [1]. Isolation and half-power beamwidth were increased by adjusting dipole spacing and chamfered edge, respectively. 9 dBi peak gain and 20 dB front-to-back ratio have been achieved for a dual-polarized radiation pattern. A miniaturized microstrip antenna with a U-shaped parasitic element using coupled feeding has been proposed to decrease horizontal dimensions [2]. Broadside-coupled parasitic elements at certain height above the antenna have been proposed for the gain enhancement of a dual feed microstrip 2×2 antenna array [3]. A $\pm 45^{\circ}$ dual-polarized planar antenna array has been proposed for the applications of 2G/3G base stations using four folded dipoles [4].

Various techniques have been proposed to increase resonant modes, antenna gains, and directivities using parasitic elements [5–18]. Multiple stacked parasitic elements between the patch antenna and its ground plane can be used to achieve multipassband characteristics [5]. 8-dBi peak gain and 14-dB front-to-back ratio over a wide frequency band have been presented by adding parasitic elements around the patch antenna [6]. High-gain antennas such as a three-layer stacked patch antenna with 8.2-dBi peak gain and 21 dB front-to-back ratio in a small volume [7], probe-fed three-layer stacked patch antenna with 9.55 average gain and 26.5% fractional bandwidth [8], and a circularly polarized stacked patch antenna with 10.5 dBi gain [9] have also been proposed. Slot-coupled circularly polarized 2×2 antenna array with increased modes and directivity using four parasitic elements achieved gain enhancement of up to 10.5 dBi [10]. 2×2 antenna arrays using cross-shaped slot [11] and chamfered edge [12] for circular polarization also presented high gain characteristics, 11.6 and 17 dBi, respectively, using parasitic elements above their antennas. The gain increased from 18.7 to 20.5 dBi in the 4×4 antenna array proposed in [13] by stacking three layers of parasitic elements above its patch antenna array. Stacks of multilayer parasitic elements are also found in millimeter-wave antenna such as [14, 15] for high gain application. Multiple parasitic elements placed on the periphery of patch antenna have been proposed to form a 2×2 antenna array [16] and a 1×8 array [17]. A wideband patch antenna is accomplished by placing a parasitic element in the elliptic slot on the patch to increase the resonant modes and bandwidth [18].

Antenna arrays are commonly used in high-gain applications. L-band feeding networks using conventional Wilkinson power dividers with different dividing ratios from 2 : 1 to 16 : 1 have been proposed [19]. A low-profile 4×4 high gain antenna array in [20] presented a 1 dBi gain within a 1.6 mm thick substrate. 17 dBi gain is achieved in the 28-GHz frequency band using a 4×4 antenna array with vertical and horizontal half-power beamwidths 13.3° and 16.6°, respectively [21]. A left-hand circularly polarized 2×2 magneto-electric dipole array with a fractional bandwidth of 27.6% and a peak gain of 14 dBi at 29 GHz is proposed in [22]. A 4×4 coupled-fed multilayered antenna array using an L-shape feeding structure demonstrated a peak gain of 19.65 dBi [23]. Another 4×4 antenna array has been proposed to lower the side lobe level from −11.9 dB to −26.8 dB by adjusting the feeding network while maintaining its gain degradation within 0.6 dB [24]. A Chebyshev array has been proposed to minimize its side lobe level below −23.8 dB with a peak gain 24 dBi [25].

Research works related to the isolation between elements of antenna arrays are also important when dealing with miniaturization [26–30]. Decoupling vias are proposed in [26] which increase element-wise isolation such that the array size can be effectively reduced. A sequential phase feed network is proposed to achieve wide bandwidths for both impedance matching and axial ratio while reducing the coupling between antenna elements [27]. Different isolation structures such as electric bandgap structures, defected ground structures, capacitive elements, and neutralization lines have been studied in [28] to realize a MIMO antenna system with an isolation as high as 65 dB. An antenna array designed for the applications of base stations proposed in [29] decoupled two linear polarized antennas in H-plane and E-plane using metasurface such that the isolation levels were increased by 15 dB. Another base station antenna with compact size and dual-polarized broadband characteristic presented an isolation design using two symmetric shorting pins with respect to the feeding cable that improved the isolation between dual polarization to 40 dB [30]. A four-element stringray-shaped MIMO antenna system using rotated element and an isolation-improving structure at the center has also been proposed with improved spatial diversity and reduced mutual coupling for UWB applications [31].

Antennas and arrays for CPE applications in the sub-6 GHz frequency band are also popular recently [32–35]. Ultra-wideband monopole antenna [32] and planar trapezoidal monopole antenna [33] were proposed with isotropic radiation patterns for TVWS CPE. A dual-band antenna system using a two-element slot meander patch antenna is proposed to operate at 1.8 GHz and 2.6 GHz for LTE-WLAN CPE [34]. Another dual-band CPE application in the sub-6 GHz frequency band using slot antenna array can also be found in [35]. A hybrid antenna-in-package (AiP) system that covers multiple frequency bands in both sub-6 GHz and millimeter frequencies using slot antenna and an 8×8 antenna array, respectively, is presented for CPE IDU [36]. In 5 G CPE applications, 45° linearly polarized antennas are typically used. Dual polarized antennas with $\pm 45^{\circ}$ linear polarization are also proposed for diversity [37].

This paper proposes the design of simple, low-cost, and low-profile antenna arrays for 5 G CPE ODU applications using microstrip antennas with parasitic elements and feeding networks using Wilkinson power dividers, which provide 10–13 dBi gains in 5 G FR1 n78 (3.3–3.8 GHz) frequency band. Design of the proposed antenna is described in Section 2, including a description of the structure and parametric studies of the antenna element, the feeding network, and the proposed arrays with the aid of 3-dimensional full-wave solver Ansys HFSS. Comparison of simulated results and experimental verification and further discussion will be presented in Section 3, followed by a few conclusion remarks in the last section.

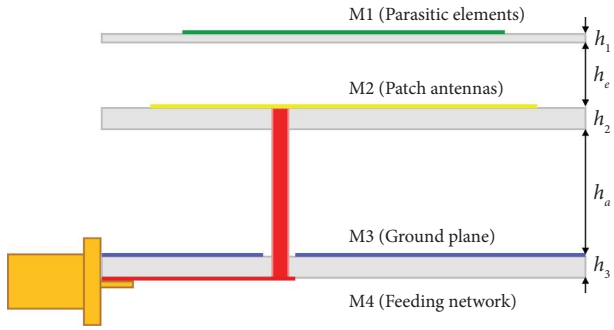

Figure 1: Layer stack up of the proposed antenna arrays (not in scale).

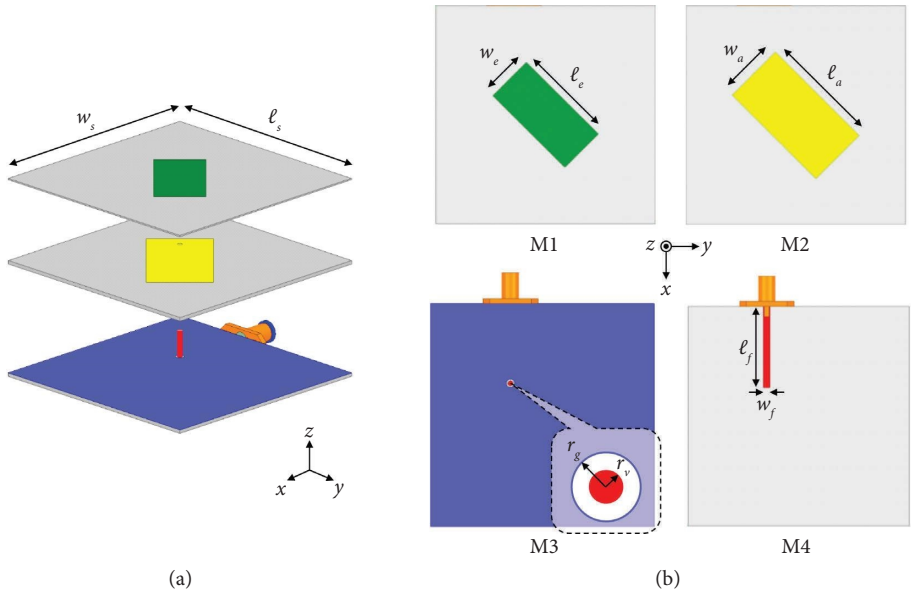

Figure 2: Structure of the proposed antenna unit. (a) Three-dimensional view. (b) Layouts at each metal layer.

2. Design of the Proposed Antenna Arrays

The proposed antenna arrays are realized in a layered structure consisting of three FR4 PCB substrate layers with air gaps supported by Nylon posts between the adjacent substrate layers, as shown in Figure 1. Four metal layers are used for the layouts of the proposed antenna arrays. The first metal layer, M1, on the upper side of the top substrate is used for parasitic elements. The microstrip patch antenna elements are placed in the second metal layer, M2, on the upper side of the center substrate. The third and fourth metal layers, M3 and M4, are the upper and lower sides of the bottom substrate, respectively. M3 is a fully covered metal layer acting as the common ground plane for both the patch antennas at M2 and the feeding network at M4. There are also through vias from M4 to M2 to perform the probe feeding from the feeding network to the antenna elements. The layer stack up has been optimized by following a similar procedure described in [38]. Design of the proposed antenna arrays consists of three parts. The design of proposed antenna units is presented first, followed by the design of feeding networks. A configuration of 45° rotated antenna units in the antenna arrays is also proposed to reduce mutual couplings without increasing the sizes of the arrays. Design results of the antenna unit with reduced mutual couplings and the feeding networks are then combined to realize the proposed antenna arrays.

2.1. Antenna Unit. As shown in Figure 2, the proposed antenna unit is formed by a microstrip rectangular patch antenna at M2 which broadside couples to another rectangular patch parasitic element right above it. The microstrip patch antenna is probe-fed using a cylindrical via structure through the antipad aperture in the ground plane (M3). The through via is then connected to a 50-Ω microstrip feeding transmission line at the bottom metal layer (M4), which is terminated by a surface mount adaptor (SMA) for experimental verification. The microstrip feeding transmission line will come from one of the output ports of the feeding networks in the design of antenna arrays. Related dimensions of the probe feeding structure are designed in a similar manner proposed by [38]. Parametric studies for the key design parameters of the proposed antenna unit are shown in Figures 3 and 4. Lengths of the microstrip patch antenna and the parasitic element, ℓ_a and ℓ_e, respectively,

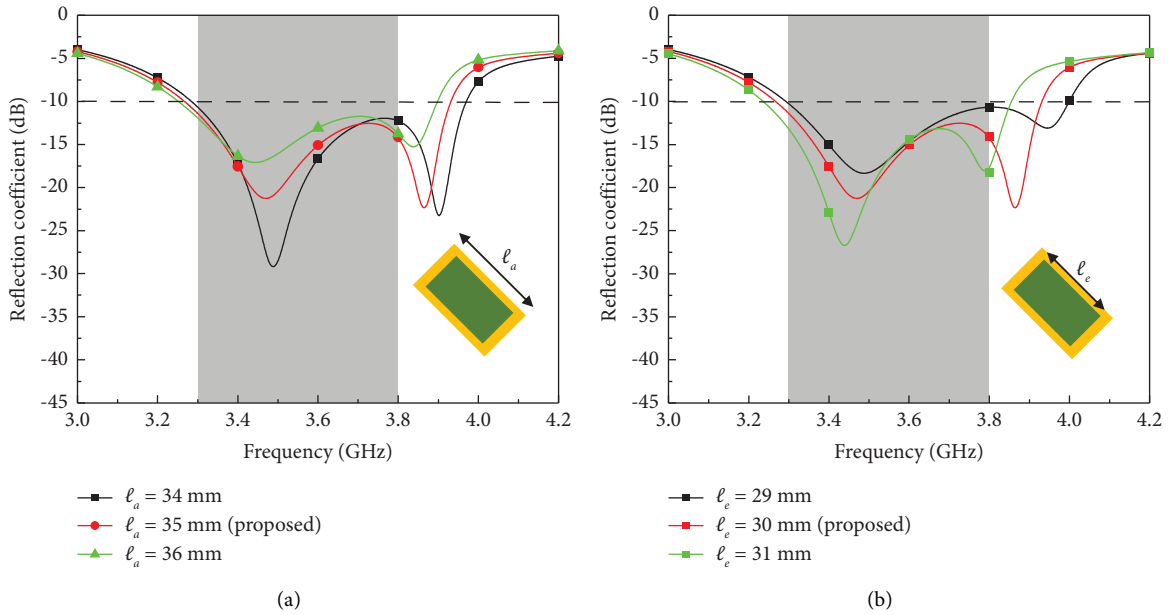

Figure 3: Adjusting the resonant modes by changing the lengths of (a) the microstrip patch antenna and (b) the parasitic element.

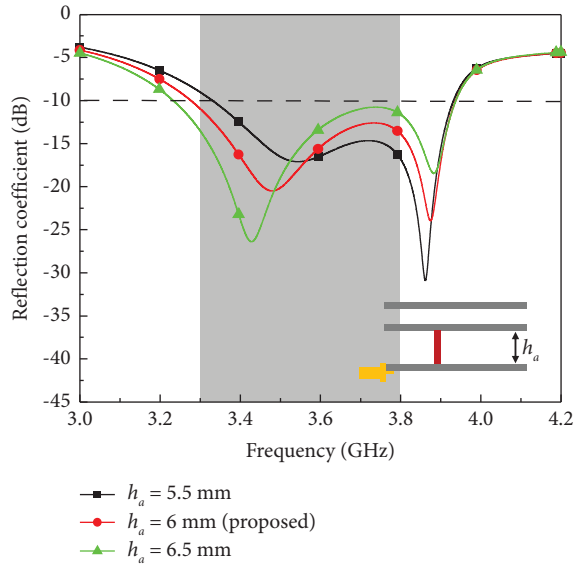

Figure 4: Adjusting the impedance matching by changing the separation between the microstrip patch antenna and its ground plane.

can be adjusted to control the lower and higher resonant modes of the proposed antenna unit. The separation between the antenna and its ground plane, h_a, can then be tuned to achieve impedance matching. The final design parameters are listed in Table 1.

2.2. Feeding Network. The feeding network of the proposed antenna arrays consist of successive power dividing stages. The Wilkinson power divider shown in Figure 5 is used as a basic building block, which are realized by following conventional design procedures [39]. Each of the output ports, port 2 and 3, is connected to another power divider in the next stage. Two- and three-stage H-tree patterns can thus be constructed for the feeding networks of the proposed 4-element (2×2) and 8-element (4×2) antenna arrays, respectively. As shown in Figure 5, return loss more than 20 dB, insertion loss less than 0.7 dB, and isolation below 25 dB can be achieved throughout the entire n78 frequency band.

2.3. Antenna Array. The proposed antenna arrays are realized by combining the previous design results. The feeding microstrip lines of the antenna units are connected to the output ports of the feeding structure. The mutual coupling between antenna units can be reduced by rotating individual antenna unit with respect to its feeding

Table 1: Final design parameters of the proposed antenna unit.

Parameter	Value (mm)
h_1	0.4
h_2	1.0
h_3	1.0
h_e	3.0
h_a	6.0
l_s	65
l_a	35
w_a	18
l_e	30
w_e	14
l_f	24
w_f	1.9
r_v	0.7
r_g	1.2

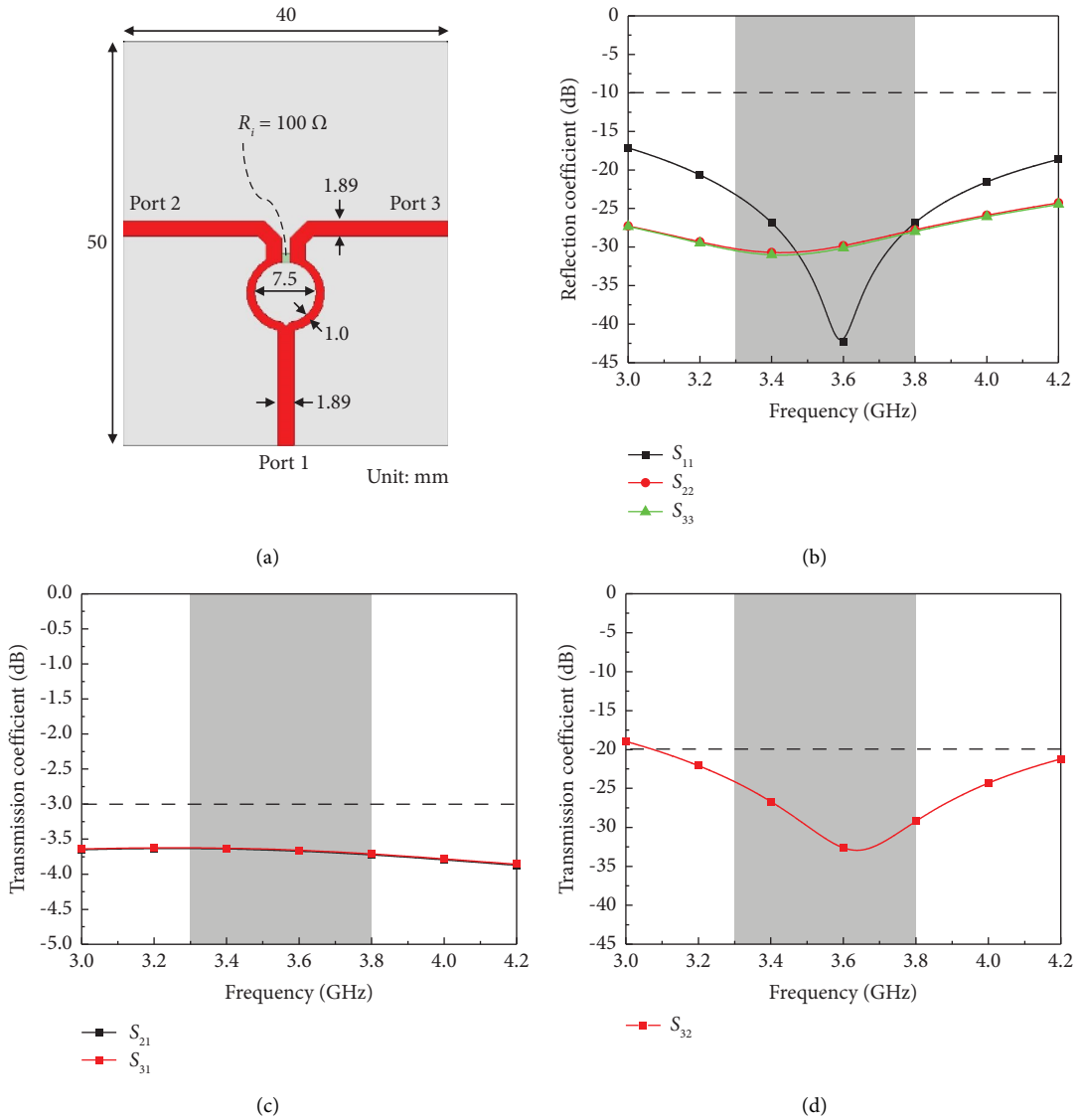

Figure 5: Wilkinson power divider used in the feeding network of the proposed antenna arrays. (a) Layouts and dimensions; (b) return loss; (c) insertion loss; and (d) isolation.

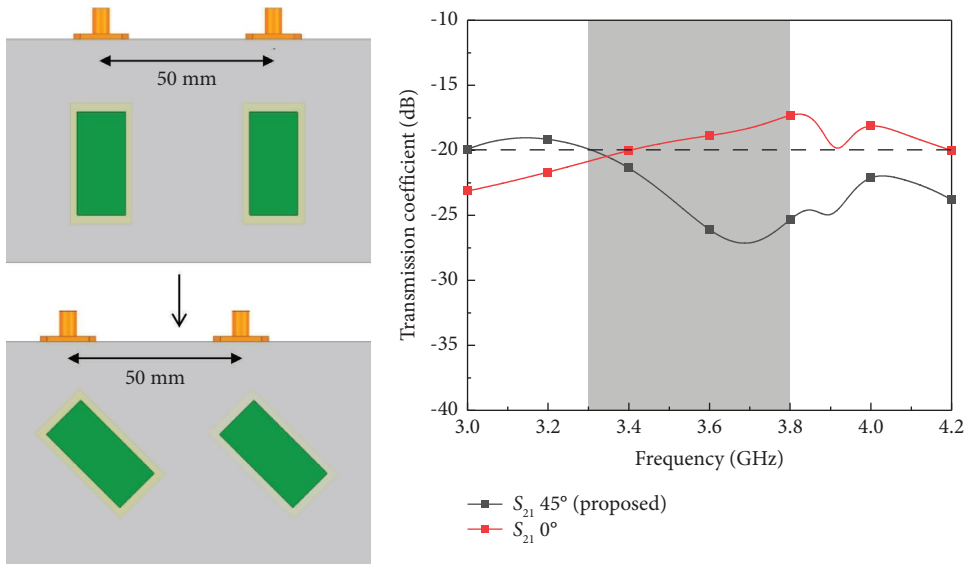

(a) (b)

Figure 6: (a) Rotating the antenna units in the antenna array to reduce mutual coupling. (b) Simulated results for different rotating angles.

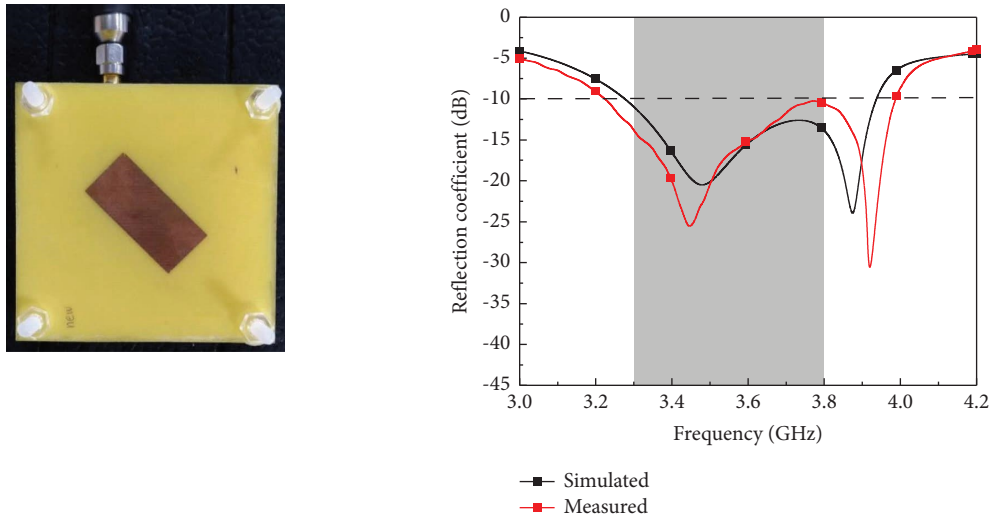

(a) (b)

Figure 7: Continued.

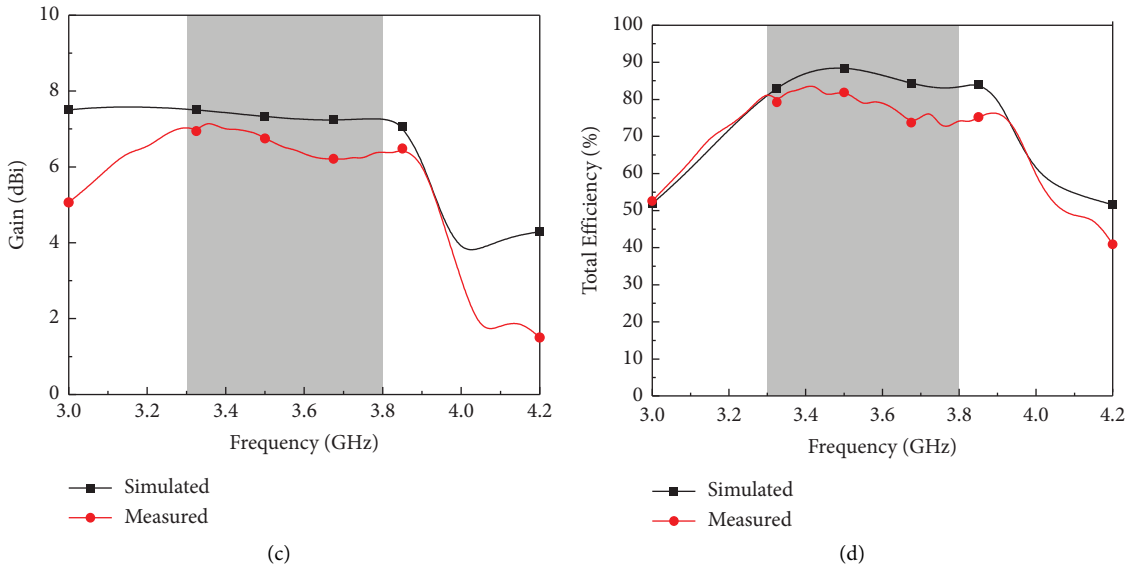

Figure 7: (a) Photo of the proposed antenna and its simulated and measured (b) return loss, (c) gain, and (d) efficiency.

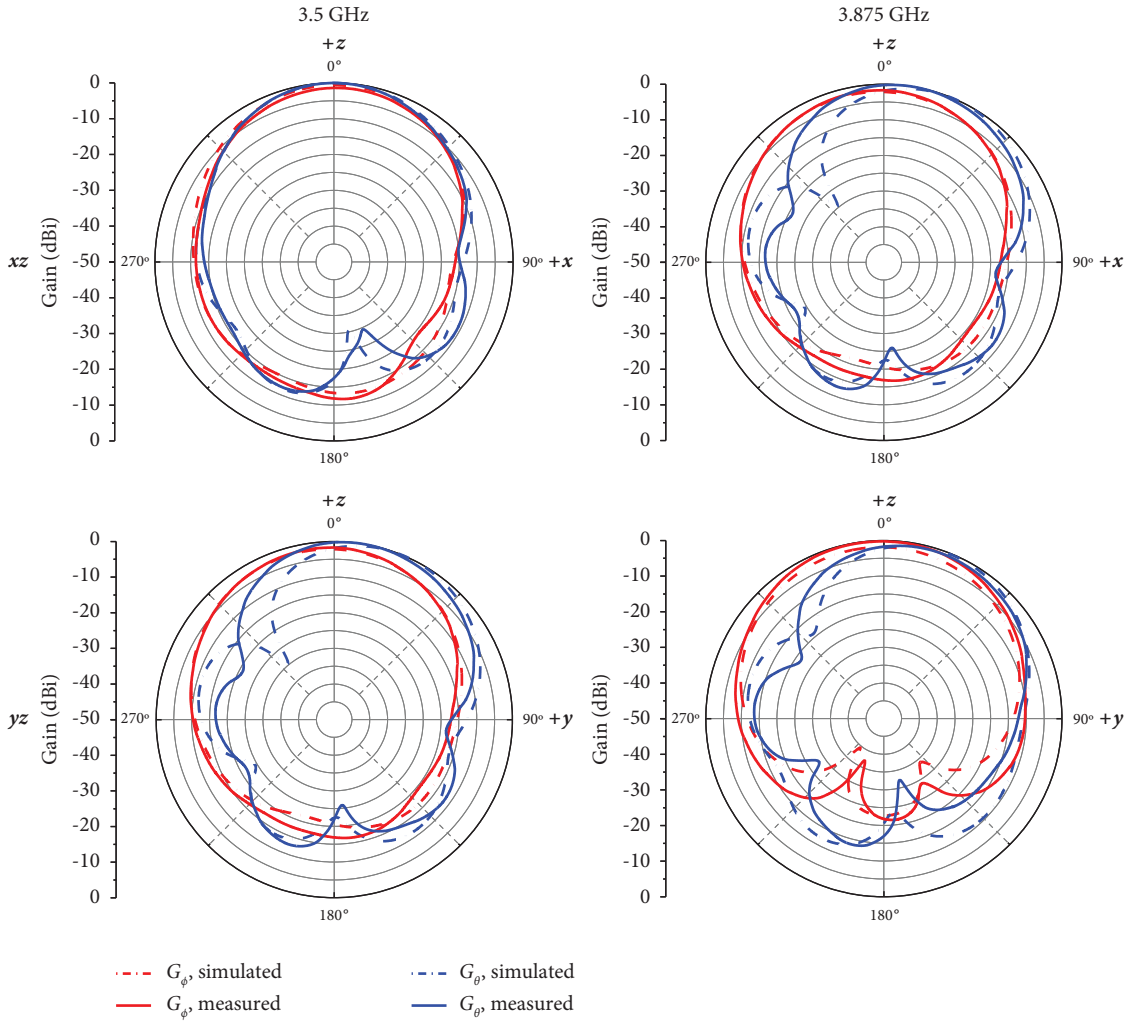

Figure 8: Simulated and measured radiation patterns of the proposed antenna at different planes and frequencies.

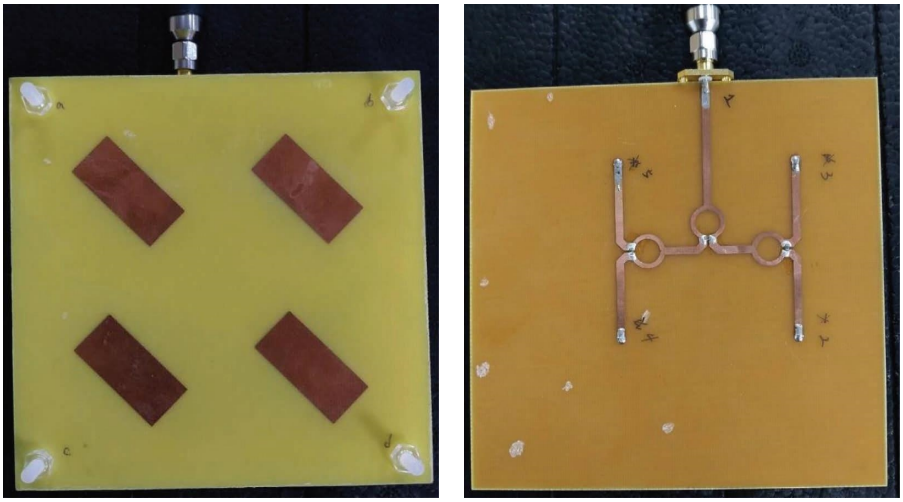

(a) (b)

Figure 9: Photo of the proposed 4-element antenna array on (a) the top side and (b) the bottom side.

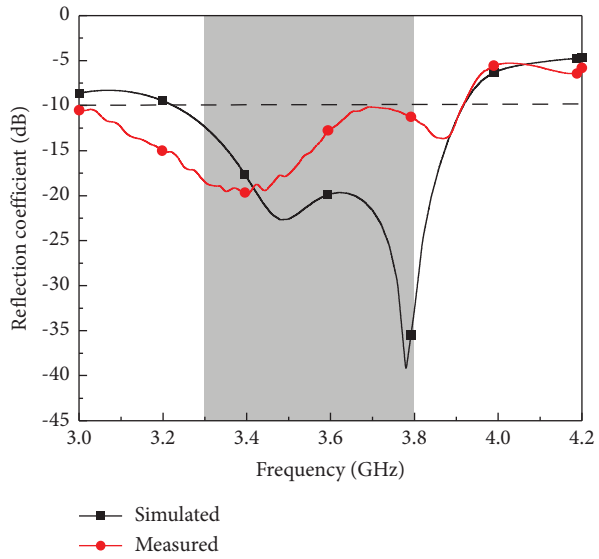

Figure 10: Simulated and measured reflection coefficients of the proposed 4-element antenna array.

probe, as shown in Figure 6(a), the minimum edge-to-edge distances between the units can be intuitively increased by a factor of $\sqrt{2}$ while the spacing between antenna units and the total sizes of the proposed arrays remain approximately the same, and the mutual thus coupling between adjacent units can be effectively reduced. Figure 6(b) shows that after a 45° rotation, the mutual coupling between the antenna units become less than 20 dB in the frequency range of interest.

3. Experimental Verification and Discussion

The proposed antenna unit, a four-element (2 × 2) array and an eight-element (4 × 2) array were fabricated to perform experimental verifications. Antenna gain and total efficiency have been measured using an automated over-the-air (OTA) compact antenna test range (CATR) measurement system [40], which was calculated in the same way as mentioned in [41–44]. The gain was calculated using Friss formula as follows:

$$G_2\ (\mathrm{dB}) = 20 \log_{10}\left(\frac{4\pi r}{\lambda}\right) + 10 \log_{10}\left(\frac{P_2}{P_1}\right) - G_1\ (\mathrm{dB}), \quad (1)$$

where G_2 and G_1 are the gains of the antenna under test and reference antenna, respectively. r is the distance between the antennas. λ is the wavelength. P_2 and P_1 are the received and transmitted power of the antenna under test and reference antenna, respectively. Total efficiency is calculated by

$$\text{Total efficiency} = \text{Radiation efficiency} \times \left(1 - |S_{11}|^2\right), \quad (2)$$

where

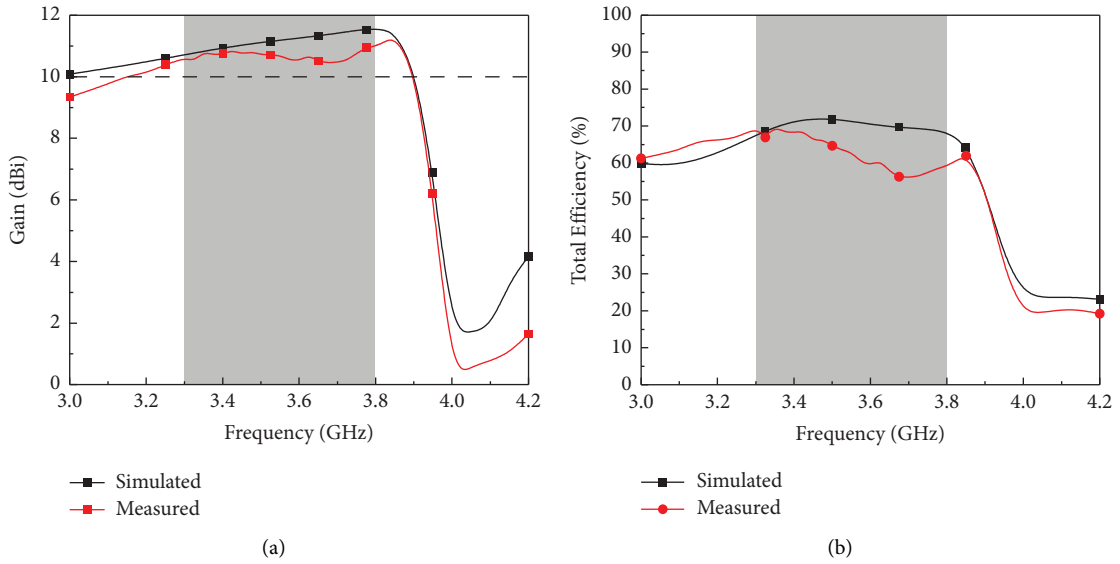

Figure 11: Simulated and measured (a) gain and (b) efficiency of the proposed 4-element antenna array.

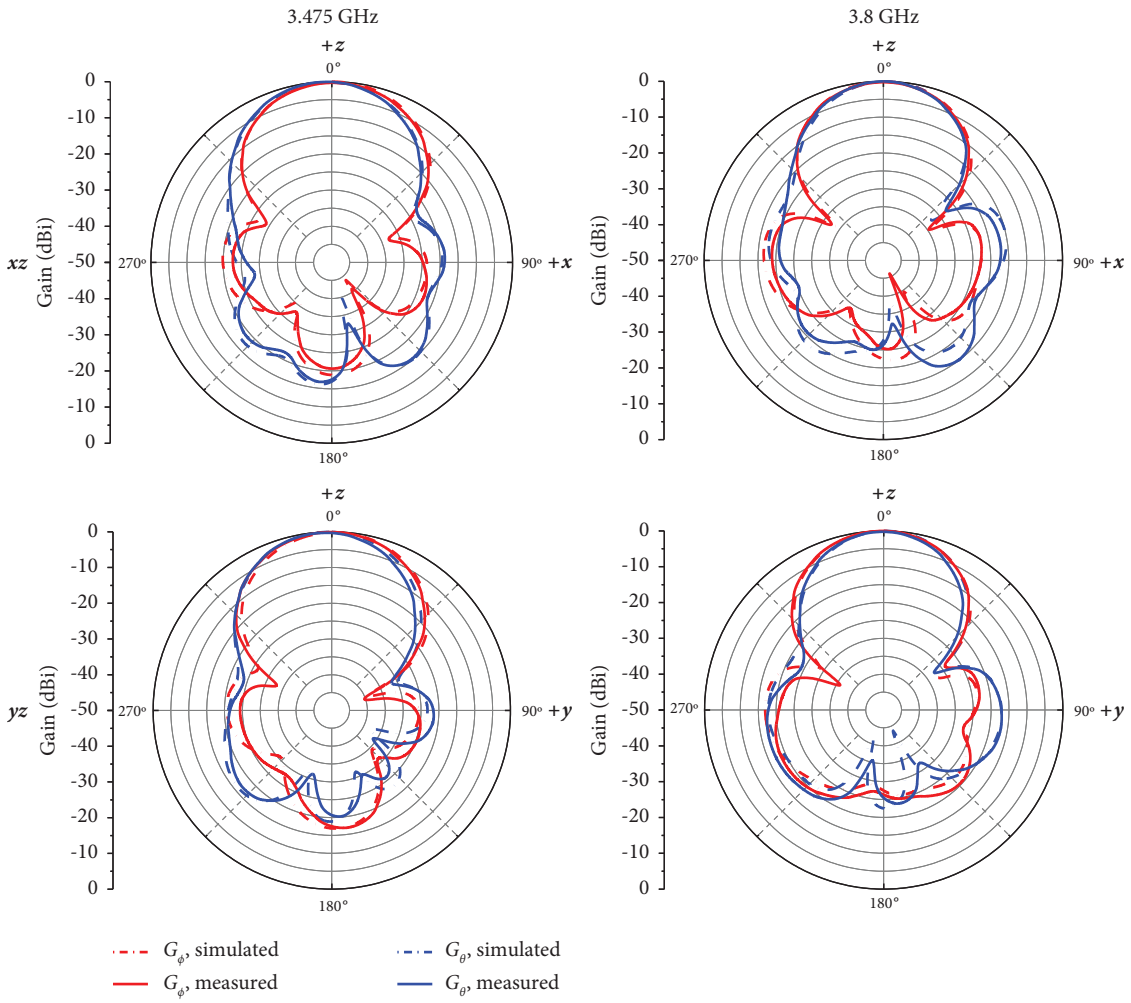

Figure 12: Simulated and measured radiation patterns of the proposed 4-element antenna array at different planes and frequencies.

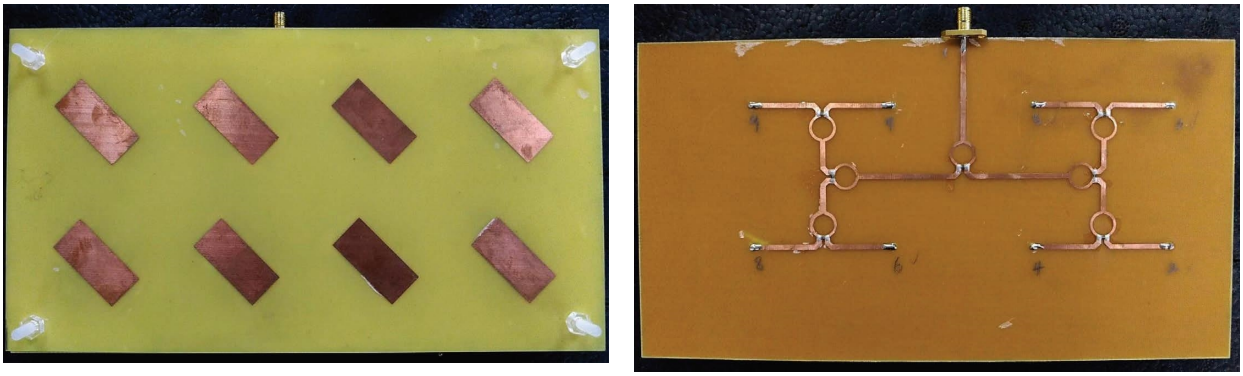

(a) (b)

Figure 13: Photo of the proposed 8-element antenna array at (a) the top side and (b) the bottom side.

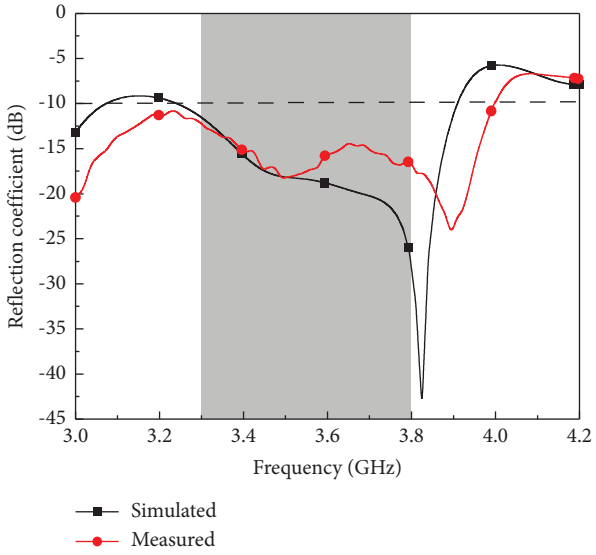

Figure 14: Simulated and measured reflection coefficients of the proposed 8-element antenna array.

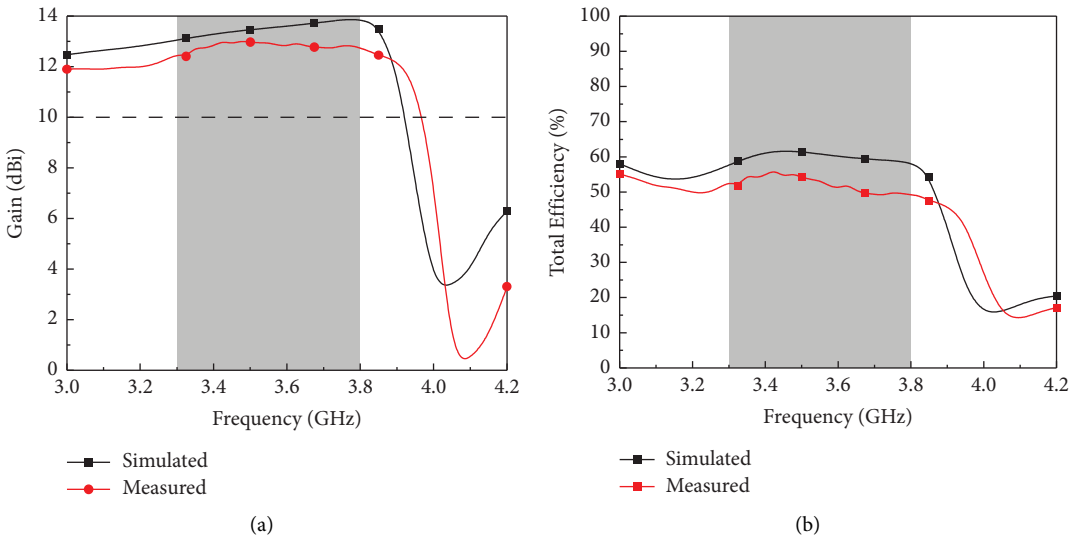

(a) (b)

Figure 15: Simulated and measured (a) gain and (b) efficiency of the proposed 8-element antenna array.

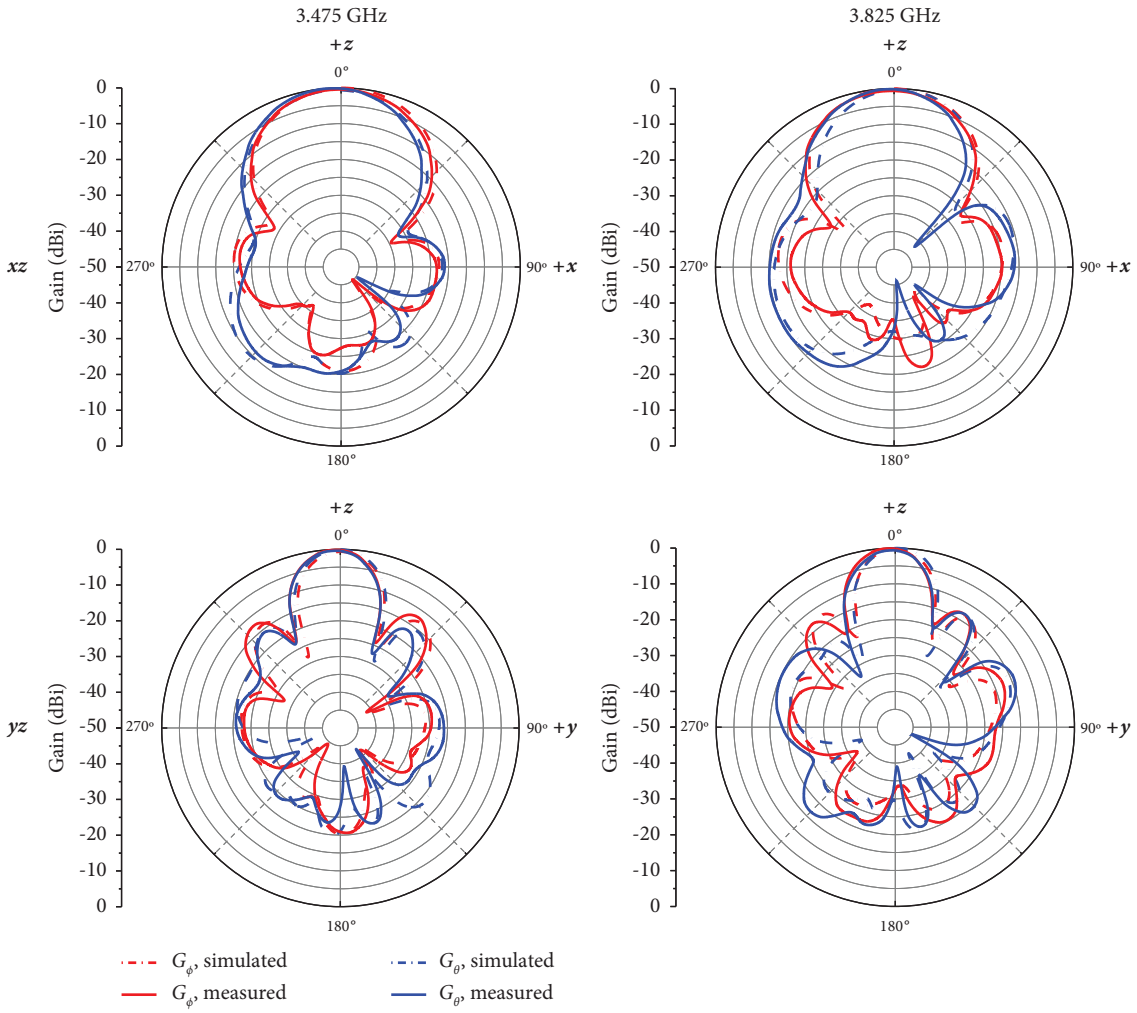

Figure 16: Simulated and measured radiation patterns of the proposed 8-element antenna array at different planes and frequencies.

$$\text{Radiation Efficiency (\%)} = \frac{\text{Gain}}{\text{Directivity}} \times 100. \quad (3)$$

Photos of the antenna unit and arrays as well as the comparison between simulated and measured results, including return losses, gain, radiation efficiency, and radiation patterns are presented with brief discussions as follows.

3.1. Antenna Unit. Figure 7 shows the photo of the proposed antenna and its simulated and measured return loss, gain, and efficiency. The overall dimension is 65 mm × 65 mm × 11.4 mm. As shown in the figure, bandwidth of 10-dB return loss from 3.23 to 3.97 GHz or a fractional bandwidth of 20.6% has been achieved. Compared to simulated data, separation between the lower and higher resonant mode has been enlarged, resulting a degradation of impedance around 3.8 GHz, which could be attributed to the fabrication error of slightly increased substrate spacing owing to PCB warpage, which is in consistent with the parameter study shown in Figure 4. 6.2 dBi gain and 74% efficiency has been achieved in the entire n78 frequency band. The measured peak gain 7.18 dBi and maximum efficiency of 82% around 3.4 GHz has been obtained. Good coherences were also obtained in the radiation patterns, as shown in Figure 8.

3.2. Four-Element Antenna Array. Figure 9 shows the photo of the proposed 4-element antenna array. The overall dimension is 115 mm × 115 mm × 11.4 mm. The simulated and measured return losses are shown in Figure 10. As shown in the figure, bandwidth of 10-dB return loss from 3.22 to 3.92 GHz, or a fractional bandwidth of 19.6% has been achieved. Figure 11 shows that 10.5 dBi gain and 56% efficiency has been achieved in the entire n78 frequency band. Measured peak gain 11 dBi around 3.8 GHz and maximum efficiency of 82% around 3.5 GHz has been obtained. Good coherences were also obtained in the radiation patterns, as shown in Figure 12.

3.3. Eight-Element Antenna Array. Figure 13 shows the photo of the proposed 4-element antenna array. The overall dimension is 115 mm × 215 mm × 11.4 mm. The simulated and measured return loss is shown in Figure 14. As shown in the figure, bandwidth of 10-dB return loss from 3.2 to

Table 2: Comparison of key parameters and performance.

Antenna	Applied design method	Number of radiation elements	Size (mm^3 (λ_0^3))	Edge-to-edge distance, mm (λ_0)	Bandwidth (GHz)	Peak gain (dBi)	Radiation efficiency (%)	Isolation (dB)	Design complexity	Practical applications
[6]	Multiple parasitic patches	4 (2 × 2)	160 × 160 × 3.5 (1.76 × 1.76 × 0.038)	~4 (~0.044)	3.35–3.9510-dB	13.6	—	>20	Low	Scanning phased arrays
[14]	Parasitic strips	4 (2 × 2)	6.4 × 5 × 0.1 (1.29 × 1.01 × 0.020)	~1.2 (~0.24)	57–6310-dB	5.7	—	—	Low	WPAN
[16]	Opposite side feeding	4 (2 × 2)	26 × 16.5 × 0.76 (2.42 × 1.54 × 0.071)	3.8 (0.35)	26.75–29.610-dB	10.35	—	—	Low	LMDS
[28]	EBG, DSG, neutral lines	4 (2 × 2)	46 × 46 × 1.6 (0.58 × 0.58 × 0.020)	8.8 (0.11)	3.1–5.510-dB	9	92(max)	>20	Low	5 G FR1
[29]	Metasurface	4 (2 × 2)	100 × 100 × 38 (1.17 × 1.17 × 0.44)	4.5 (0.053)	3.3–3.715-dB	7.2	90	>25	Low	5 G base stations
[30]	Dielectric cavity	8 (2 × 4), dual pol	101 × 170 × 14 (1.16 × 1.96 × 0.16)	40 (0.46)	3.2–3.915-dB	6.8	—	>40	Low	5 G, MIMO
Proposed antenna	Probe-fed, parasitic element, Wilkinson power divider	1	65 × 65 × 11.4 (0.74 × 0.74 × 0.13)	—	3.23–3.9910-dB	7.18	74	—	Low	5 G FR1 CPE
Proposed 4-element array		4 (2 × 2)	115 × 115 × 11.4 (1.30 × 1.30 × 0.13)	17.9 (0.20)	3.0–3.9210-dB	11	56	>24	Low	5 G FR1 CPE
Proposed 8-element array		8 (2 × 4)	115 × 215 × 11.4 (1.30 × 2.44 × 0.13)	17.9 (0.20)	3.0–3.9910-dB	13.01	50	>20	Low	5 G FR1 CPE

4.0 GHz or a fractional bandwidth of 22.2% has been achieved. Figure 15 shows that a 12 dBi gain and 50% efficiency have been achieved in the entire n78 frequency band. Measured peak gain 13.8 dBi around 3.8 GHz and maximum efficiency of 56% around 3.4 GHz has been obtained. Good coherences were also obtained in the radiation patterns, as shown in Figure 16.

4. Conclusions

A microstrip patch antenna with parasitic element has been proposed to build two antenna arrays of different sizes for CPE ODU applications in the n78 frequency band of 5 G NR FR1. The antenna unit has achieved a bandwidth of 10-dB return loss from 3.23 to 3.29 GHz which fully covered the desired frequency band. 6.2 dBi gain and 74% efficiency have been achieved in the entire n78 frequency band with a peak gain of 7.18 dBi and a maximum efficiency of 82%. Wilkinson power-divider-based feeding networks are used to realize the proposed four-element and eight-element arrays. Rotated antenna units with respect to their feeding points were also proposed to reduce mutual coupling to below −20 dB without increasing the separations between antenna units and overall array sizes. The proposed four-element and eight-element arrays exhibited average gains around 10.5 dBi and 13 dBi, respectively, and more than 10 dB return loss throughout the entire n78 frequency band. The comparison of key parameters and performance for different antennas is listed in Table 2, where λ_0 is the wavelength at the first resonance frequency of respective antenna element in free space. The proposed method is easily extended for the realization of array antennas with element numbers in the powers of 2. For element numbers that are not multiples of 2, n-way Wilkinson power dividers are also available but not as trivial [39]. For large arrays the loss of the transmission line segments in the FR4 substrate will significantly reduce the gain of increasing element numbers, thus low loss substrates must be used instead. The proposed antenna arrays have demonstrated the advantages of simple, low-cost, low profile, as well as high gain characteristics over the entire n78 frequency band, which is potentially applicable to 5 G CPE outdoor unit (ODU)-related devices.

Data Availability

The simulated and measured data used to support the findings of this study are available from the corresponding author upon request.

Conflicts of Interest

The authors declare that they have no conflicts of interestr.

Acknowledgments

The authors would like to acknowledge BWant Co. Ltd. for the help on the experimental verification of the proposed antenna arrays with their automated OTA measurement system. This paper was supported in part by the Ministry of Science and Technology, under Grant MOST 110-2221-E-035-023-.

References

[1] J. Sun, J. Li, and L. Xia, "A dual-polarized magneto-electric dipole antenna for application to n77/n78 band," *IEEE Access*, vol. 7, pp. 161708–161715, 2019.

[2] S. Wi, Y. Lee, and J. Yook, "Wideband microstrip patch antenna with U-shaped parasitic elements," *IEEE Transactions on Antennas and Propagation*, vol. 55, no. 4, pp. 1196–1199, 2007.

[3] H. Satow, E. Nishiyama, and I. Toyoda, "Gain enhancement of a dual feed microstrip array antenna using parasitic elements," in *Proceedings of the 2015 International Symposium on Antennas and Propagation (ISAP)*, pp. 1–4, Hobart, TAS, Australia, November 2015.

[4] D. Wen, D. Zheng, and Q. Chu, "A dual-polarized planar antenna using four folded dipoles and its array for base stations," *IEEE Transactions on Antennas and Propagation*, vol. 64, no. 12, pp. 5536–5542, 2016.

[5] J. Anguera, G. Font, C. Puente, C. Borja, and J. Soler, "Multifrequency microstrip patch antenna using multiple stacked elements," *IEEE Microwave and Wireless Components Letters*, vol. 13, no. 3, pp. 123-124, 2003.

[6] K. D. Xu, J. Zhu, S. Liao, and Q. Xue, "Wideband patch antenna using multiple parasitic patches and its array application with mutual coupling reduction," *IEEE Access*, vol. 6, pp. 42497–42506, 2018.

[7] A. Katyal and A. Basu, "Compact and broadband stacked microstrip patch antenna for target scanning applications," *IEEE Antennas and Wireless Propagation Letters*, vol. 16, pp. 381–384, 2017.

[8] J. Wang, J. Shi, and Q. Cao, "A high-gain broadband stacked patch antenna with finite ground," in *Proceedings of the 2017 Sixth Asia-Pacific Conference on Antennas and Propagation*, pp. 1–3, APCAP, Xi'an, China, October 2017.

[9] V. S. Kraanthi, "High gain circularly polarized stacked patch antenna at c-band for geo satellite telemetry application," in *Proceedings of the 2019 IEEE Indian Conference on Antennas and Propogation*, pp. 1–4, Ahmedabad, India, December 2019.

[10] M. Akbari, M. Farahani, A. R. Sebak, and T. A. Denidni, "A 30GHz high-gain circularly-polarized pattem-steerable antenna based on parasitic patches," in *Proceedings of the 2017 11th European Conference on Antennas and Propagation (EUCAP)*, pp. 3044–3046, Paris, France, March 2017.

[11] K. Lee, J. Oh, and S. Yi, "Stacked microstrip patch antenna array with high-gain and improved thermal-stability for microwave power transmission applications," in *Proceedings of the 2018 Asia-Pacific Microwave Conference (APMC)*, pp. 1432–1434, Kyoto, Japan, November 2018.

[12] M. Saad Khan and F. A. Tahir, "A circularly polarized stacked patch antenna array for tracking applications in S-band," in *Proceedings of the 2015 9th European Conference on Antennas and Propagation (EuCAP)*, pp. 1–4, Lisbon, Portugal, April 2015.

[13] L. Wang, J. Wang, and J. Shi, "Design of 4×4 meandering-fed stacked patch antenna array," in *Proceedings of the 2018 International Workshop on Antenna Technology (iWAT)*, pp. 1–3, Nanjing, China, March 2018.

[14] H. Jin, W. Che, W. Yang, and K.-. Chin, "High-gain 60-GHz patch antenna array using GaN MMIC technology," in *Proceedings of the 2015 IEEE 4th Asia-Pacific Conference on Antennas and Propagation (APCAP)*, pp. 150-151, Bali, Indonesia, July 2015.

[15] M. U. Raza and S. Yan, "Dual band millimeter wave phased array antenna for 5G mobile communications," in *Proceedings*

of the 2020 IEEE 3rd International Conference on Electronic Information and Communication Technology (ICEICT), pp. 247-248, Shenzhen, China, December 2020.

[16] K.-S. Chin, H.-T. Chang, J.-A. Liu, H.-C. Chiu, J. S. Fu, and S.-H. Chao, "28-GHz patch antenna arrays with PCB and LTCC substrates," in *Proceedings of the 2011 Cross Strait Quad-Regional Radio Science and Wireless Technology Conference*, pp. 355–358, Harbin, China, July 2011.

[17] M. Wang et al., "A Ka-band high-gain dual-polarized microstrip antenna array for 5G application," in *Proceedings of the 2019 International Conference on Microwave and Millimeter Wave Technology (ICMMT)*, pp. 1–3, Guangzhou, China, May 2019.

[18] Z. Ling, C. Liu, and H. Li, "Wideband patch antenna array for 5G terminal devices," in *Proceedings of the 2020 IEEE 3rd International Conference on Electronic Information and Communication Technology (ICEICT)*, pp. 610–612, Shenzhen, Chin, November 2020.

[19] D. De, A. Prakash, N. Chattoraj, P. K. Sahu, and A. Verma, "Design and analysis of various Wilkinson power divider networks for L band applications," in *Proceedings of the 2016 3rd International Conference on Signal Processing and Integrated Networks (SPIN)*, pp. 67–72, Noida, India, February 2016.

[20] G. M. Aji, M. A. Wibisono, and A. Munir, "High gain 2.4 GHz patch antenna array for rural area application," in *Proceedings of the 2016 22nd Asia-Pacific Conference on Communications (APCC)*, pp. 319–322, Yogyakarta, August 2016.

[21] J. Xiao, T. Ding, and Q. Ye, "High-gain multilayer patch antenna array," in *Proceedings of the 2020 9th Asia-Pacific Conference on Antennas and Propagation (APCAP)*, pp. 1-2, Xiamen, China, August 2020.

[22] H. Wang, K. E. Kedze, and I. Park, "Microstrip patch array antenna using a parallel and series combination feed network," in *Proceedings of the 2018 International Symposium on Antennas and Propagation (ISAP)*, pp. 1-2, Busan, Korea (South), October 2018.

[23] D. N. Arizaca-Cusicuna, J. Luis Arizaca-Cusicuna, and M. Clemente-Arenas, "High gain 4×4 rectangular patch antenna array at 28GHz for future 5G applications," in *Proceedings of the 2018 IEEE XXV International Conference on Electronics, Electrical Engineering and Computing (INTERCON)*, pp. 1–4, Lima, August 2018.

[24] K.-X. Li, Y.-W. Wu, and Z.-C. Hao, "A 5G millimeter-wave circularly polarized planar antenna array," in *Proceedings of the 2020 9th Asia-Pacific Conference on Antennas and Propagation (APCAP)*, pp. 1-2, Xiamen, China, August 2020.

[25] B. P. A. Mahatmanto and C. Apriono, "Planar microstrip array antenna with rectangular configuration fed with Chebyshev power distribution for C-band satellite application," in *Proceedings of the 2019 IEEE International Conference on Innovative Research and Development (ICIRD)*, pp. 1–4, Jakarta, Indonesia, June 2019.

[26] L. Chen, W. Yang, W. Che, and Q. Xue, "High-isolation dual-polarized patch antenna array," in *Proceedings of the 2020 IEEE MTT-S International Microwave Workshop Series on Advanced Materials and Processes for RF and THz Applications (IMWS-AMP)*, pp. 1–3, Suzhou, China, July 2020.

[27] S. Mohammadi-Asl, J. Nourinia, C. Ghobadi, and M. Majidzadeh, "Wideband compact circularly polarized sequentially rotated array antenna with sequential-phase feed network," *IEEE Antennas and Wireless Propagation Letters*, vol. 16, pp. 3176–3179, 2017.

[28] A. A. Megahed, M. Abdelazim, E. H. Abdelhay, and H. Y. M. Soliman, "Sub-6 GHz highly isolated wideband MIMO antenna arrays," *IEEE Access*, vol. 10, pp. 19875–19889, 2022.

[29] J. Guo, F. Liu, L. Zhao, Y. Yin, G.-L. Huang, and Y. Li, "Metasurface antenna array decoupling designs for two linear polarized antennas coupled in H-plane and E-plane," *IEEE Access*, vol. 7, pp. 100442–100452, 2019.

[30] M. Li, X. Chen, A. Zhang, and A. A. Kishk, "Dual-polarized broadband base station antenna backed with dielectric cavity for 5G communications," *IEEE Antennas and Wireless Propagation Letters*, vol. 18, no. 10, pp. 2051–2055, 2019.

[31] H. Ş. Savcı, "A four element stringray-shaped MIMO antenna system for UWB applications," *Micromachines*, vol. 14, no. 10, pp. 1944–1963, 2023.

[32] A. K. Singh and M. Ranjan Tripathy, "M-shaped ultra wide band monopole antenna for TVWS CPE," in *Proceedings of the 2018 5th International Conference on Signal Processing and Integrated Networks (SPIN)*, pp. 240–243, Noida, India, February 2018.

[33] A. K. Singh and M. R. Tripathy, "Planar trapezoidal monopole antenna for TVWS CPE," in *Proceedings of the 2018 3rd International Conference for Convergence in Technology (I2CT)*, pp. 1–3, Mangalore, India, April 2018.

[34] N. I. M. Elamin and T. A. Rahman, "2-Element slot meander patch antenna system for LTE-WLAN customer premise equipment," in *Proceedings of the 2015 IEEE-APS Topical Conference on Antennas and Propagation in Wireless Communications (APWC)*, pp. 993–996, Turin, Italy, September 2015.

[35] J.-H. Lu, B.-M. Chen, and W.-R. Chuang, "Design of dual-band slot antenna array for 5G sub-6 GHz CPE," in *Proceedings of the 2021 International Symposium on Antennas and Propagation (ISAP)*, Taipei, Taiwan, November 2021.

[36] R. Zhang, Z. Yi, Y. Chen, L. Zhu, H. Jin, and G. Yang, "A hybrid antenna system for 5G-WLAN customer premise equipment (CPE) application," in *Proceedings of the 2019 International Applied Computational Electromagnetics Society Symposium-China (ACES)*, pp. 1-2, Nanjing, China, August 2019.

[37] X. Tang, H. Chen, B. Yu, W. Che, and Q. Xue, "Bandwidth enhancement of a compact dual-polarized antenna for Sub-6G 5G CPE," *IEEE Antennas and Wireless Propagation Letters*, vol. 21, no. 10, pp. 2015–2019, 2022.

[38] R. B. Waterhouse, "Design of probe-fed stacked patches," *IEEE Transactions on Antennas and Propagation*, vol. 47, no. 12, pp. 1780–1784, 1999.

[39] D. M. Pozar, *Microwave Engineering*, Wiley, New York, NY, USA, 2011.

[40] Bwant Co Ltd, "CATR automated OTA measurement system," https://www.bw-ant.com/en/product.html.

[41] J. Kulkarni, N. Kulkarni, and A. Desai, "Development of "H-Shaped" monopole antenna for IEEE 802.11a and HIPERLAN 2 applications in the laptop computer," *International Journal of RF and Microwave Computer-Aided Engineering*, vol. 30, no. 7, 2020.

[42] J. Kulkarni, "Multi-band printed monopole antenna conforming bandwidth requirement of GSM/WLAN/WiMAX standards," *Progress In Electromagnetics Research Letters*, vol. 91, pp. 59–66, 2020.

[43] J. Kulkarni and C. Y. D. Sim, "Wideband CPW-fed oval-shaped monopole antenna for wi-fi5 and wi-fi6 applications," *Progress in Electromagnetics Research C*, vol. 107, pp. 173–182, 2021.

[44] J. S. Kulkarni, "Design and development of ultra-thin monopole antenna for WLAN and WiMAX operations in the next-generation laptop computer," in *Proceedings of the 2019 International Conference on Radar, Antenna, Microwave, Electronics, and Telecommunications (ICRAMET)*, pp. 79–83, Tangerang, Indonesia, October 2019.

Hindawi
International Journal of Antennas and Propagation
Volume 2023, Article ID 1384388, 17 pages
https://doi.org/10.1155/2023/1384388

Research Article

A Single-Layer S/X- Band Shared Aperture Antenna with MIMO Characteristics at X-Band for Airborne Synthetic Aperture Radar Applications

Raja Babu Bandi,[1] **Venkata Kishore Kothapudi**,[1] **Lakshman Pappula**,[2] **Rajkumar Kalimuthu**,[3] **and Srinivasa Kiran Gottapu**[4]

[1]*Center of Excellence Advanced RF Microwave and Wireless Communications, Department of Electronics and Communication Engineering, School of Electrical, Electronics and Communication Engineering, Vignan's Foundation for Science, Technology, and Research (VFSTR Deemed to be University), Vadlamudi, Guntur 522213, Andhra Pradesh, India*
[2]*Department of ECE, Koneru Lakshmaiah Education Foundation, Vaddeswaram, Guntur 522302, Andhra Pradesh, India*
[3]*School of Computer Science&Information Technology, DMI-St. John the Baptist University, Lilongwe, Malawi*
[4]*Department of Electrical Engineering, University of North Texas, Denton, Texas, USA*

Correspondence should be addressed to Rajkumar Kalimuthu; rajkumar@dmisjbu.edu.mw

Received 5 October 2022; Revised 15 October 2022; Accepted 24 November 2022; Published 30 March 2023

Academic Editor: Chow-Yen-Desmond Sim

New frequencies can be supported with very effective space use by using the shared aperture antenna This work presents on designing a dual-banddual-polarized (DBDP) S/X-band shared aperture antenna (SAA) for synthetic aperture radar (SAR) applications operating at S-band frequency (3.2 GHz) and X-band frequency (9.65 GHz). The single-layer SAA DBDP S-band antenna is designed in a square-shaped patch with coaxial feeding in both vertical and horizontal polarization. The X-band antenna design is in 1×3 vertical series with microstrip feeding and arranged at four corners of the proposed antenna. The S-band antenna is mainly used for airborne applications such as air traffic control and surface ship radar. In contrast, the X-band antenna application is maritime vessel traffic control, defense tracking, and vehicle speed detection for law enforcement. To verify the antenna, a prototype is fabricated and measured with s-parameters. The proposed design exhibits that the gain of the S-band is 7.2 dB and for the X-band is 12.4 dB, and the isolation is achieved more than −35 dB, and for this antenna, we achieved a bandwidth of 0.12 GHz for S-band and 0.27 GHz for X-band. However, the X-band antenna is a multi-input and multioutput antenna that is to be validated by using MIMO characteristic parameters such as envelope correlation coefficient (ECC), diversity gain (DG), channel capacity loss (CCL), mean effective gain, and mutual coupling. The MIMO characteristic parameter of X-band antenna values is found to be in a similar manner to both simulated and measured values. For this X-Band antenna, ECC, DG, CCL, and mutual coupling were achieved as below 0.05, 9.5 dB, 0.5 bps/Hz, and −30 dB to −55 dB, respectively. The total size of the antenna is 100 mm × 100 mm × 1.6 mm.

1. Introduction

For the last several years, research tending toward the multipolarization direction. A single polarized antenna responds only to one orientation of polarization, either horizontal or vertical. Thus, radio waves that are received or transmitted by a single polarized antenna will be either horizontal or vertical polarized. Whereas coming dual-polarized, it can respond to both horizontally and vertically polarized radio waves.

By using strip-line technology and resonant field phenomena, we can get better results in achieving a medium gain of the antenna over satisfied bandwidth [1]. The configuration of the microstrip antenna is in such a way that a combination of microstrip dipoles and square patches with a 1 : 3 frequency ratio [2–4]. To achieve the design of an S/X array antenna, X-band needs to be a series-fed configuration. In contrast, the S-band in other configurations achieves higher radiation aperture and gain by using two different

ports, which are orthogonal and result in high isolation [3]. For the S/X-band array antenna, we can increase the impedance bandwidth for the X-band by varying the electromagnetic coupling between prominent and parasitic patches. Whereas coming to the S-band antenna, to increase its bandwidth, we can use modified coupling feeding and perforated patches [5]. For better results, a novel design approach in both S/X-bands to achieve it by frequency ratio is 1 : 3.3, and for a higher frequency, X-Band is used to radiate such high frequency for lower frequency S-band antenna is used [6]. To suppress higher-order modes, we used to integrate microstrip LPF within the patch antenna, which radiates at a lower frequency [7]. We need to use different polarization to achieve high isolation in dual polarized and dual wideband antenna. For S-band, we used to use circular polarization. For X-band, we used to use linear polarization [8]. While comparing a normal antenna and a shared aperture antenna, it shows that the SAR antenna has more advantages [9]. For achieving narrow FBW in S-band and X-band in the SAR antenna, the S-band antenna is in the microstrip antenna, which is a dual-polarized subarray of the antenna used for X-band Radiation [10]. The study tells that for SAR application which is used at 9.65 GHz frequency, a dual -a polarized array antenna is best to achieve high gain by placing six ports. Thus, arranging it in such a way, we can get better impedance matching bandwidth, and −25 dB isolation is achieved between inter- and intraport polarization at all ports [11]. Dual-polarizedseries-fed antenna radiation characteristics can be increased by series feeding, which has an interconnection between patches [12]. To design the radar application and for better results, we used to design the antenna using Chebyshev amplitude distribution (CAD) and uniform amplitude distribution (UAD) [13]. Gain and front-to-back ratio are improved in series-fed linear array antenna, which is useful in Radar-X-band applications [14]. Using the Chebyshev technique with a width-controlled patch antenna to incorporate both X-band and K-band to achieve better results, we can use linear or circular polarization within a single-layer [15]. A study shows that corporate feeding is introduced at both vertical and horizontal polarization and used at X-band frequency for implementing the shared aperture dual-banddual-polarized multilayer antenna. A cross-shaped element is used to differentiate between the elements [16]. Using a neutralization line can reduce the mutual coupling in the antenna structure by using meander microstrip lines. It provides flexibility for the antenna [17]. For achieving better MIMO characteristics like broader bandwidth and higher isolation in an antenna, the authors use a ring resonator-based coplanar waveguide to feed the ports [18]. To achieve wideband bandwidth and resonates at the lower band (LTE bands 42/43–N77–N78), the higher band (LTE 46) and the intermediate band (N79) antenna were designed in predesigned shape like Hexa decagon polygon not only for that it also achieves better MIMO characteristics [19]. The antenna pattern is more considerable when we analyze the MIMO characters, such as the ground's height and the antenna's location, which are directly affected by the radiation pattern [20]. To increase the bore side gain for sub −6 GHz with two port configurations, the authors proposed a circular-shaped antenna with an inner circular slot and a rectangular slot at the edges by obeying the traditional value of <2 W/kg for any 10 g of tissue [21]. By incorporating a varactor diode into its CLL-based NFRP element, a frequency-agile version of a passive fixed-value capacitor in the antenna bandwidth is increased by four times and provides good impedance matching, better stability, and stable and uniform radiation pattern over the frequency range [22]. There is a chance of increase in gain and bandwidth based on antenna arrangements like rectangular, triangular, and hexagonal antennas that can work in different frequencies-based variations of radiation angle [23]. For various LTE bands, the authors proposed an antenna that contains parallel strips at side walls and a metal strip at the top face to reduce the size and achieve better MIMO characteristics [24]. By implementing a nonradiating flooded shorting strip between MIMO antenna elements, there are chances to attain the MIMO characteristics and use a technique called mitigating multipath fading, which helps mobile communication [25]. The authors proposed a multielement antenna in a T-shaped slot antenna that is used to enhance the isolation. Better MIMO characteristics show superior robustness and MIMO capabilities under different hand-grip conditions [26]. In this antenna, an inner square ring resonator is embedded in T-shape substrate and uses the dot walls at radiating patches which helps to enhance the MIMO characteristics [27].

Considering the above-given literature review, we will propose a combination of a coaxial antenna and 1 × 3 series-fed linear array antenna using direct coupling with a quarter-wave transformer presented on 4 sides. The proposed antenna is designed at 3.2 GHz S-band and 9.65 X-band. The proposed antenna is analyzed by performing a full-wave simulation using an industry-standardFFT-based CST MWS software 2021. The proposed antenna is fabricated and tested. The proposed antenna structure and design are discussed in Section 2, and the simulated and experimental result is discussed in Section 3. The analysis is discussed in Section 4. Finally, the conclusions are discussed in Section 5.

2. Structure of the Proposed Antenna Representation on Payload

The SAR representation is shown in Figure 1. The configuration of the proposed antenna is the combination of two antennas that are operated in dual-band frequency, i.e., 3.2 GHz for S-band frequency and 9.65 GHz for X-band frequency. It consists of a square-shaped antenna which is operated at 3.2 GHz and that is fed with coaxial feeding; it is placed in the middle of the antenna polarization that is carried out in two directions which are orthogonal to each order, and it also consists of a 1 × 3 linear array antenna which is operated at 9.65 GHz and that is feed with microstrip feeding or direct coupling, and it is situated at corners of the antenna. To reduce the losses of the antenna while transmission, we have chosen the square shape patches in both S-band and X-band antennas. In this work, an FR-4 material is used as a substrate with 1.6 mm height and its relative permittivity is $\varepsilon r = 4.4$ and loss tangent tan $d = 0.03$.

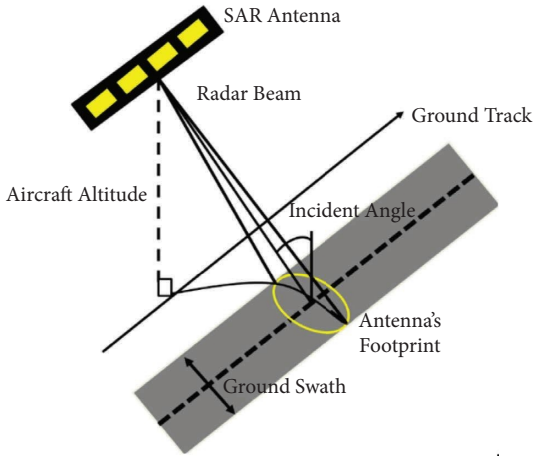

Figure 1: Airborne synthetic aperture radar geometry.

All the metal components which are represented in the work are taken to be copper which is having parameters $\varepsilon r = 1$ and $\mu r = 1$ and bulk conductivity $\sigma = 5.8 \times 107$ s/m.

2.1. Structure of the S-Band Antenna. The configuration of the S-band single patch antenna is displayed in Figure 2 with dual polarization (both vertical and horizontal polarizations) with all parameters. The patch is excited using 50 Ω coaxial feeding for both vertical and horizontal polarizations for better impedance matching; inner and outer pin radius is taken as 0.6 and 2.176, respectively. The final optimized parameters of the S-band antenna are shown in Table 1. The frequency response is shown in Figure3 which indicates antenna resonates at 3.2 GHz at both vertical and horizontal ports. The impedance bandwidth covers from 3.18 GHz to 3.3 GHz and achieves isolation of more than −30 dB.

2.2. Structure of the X-Band Antenna. The configuration of the X-band array antenna is displayed in Figure 4 with single polarization with all physical parameters. The array patch is excited using 50 Ω direct coupled microstrip line feeding for the port. The width of the matching transformer section of the direct coupled fed line is MTW = 2.46 to obtain the 50 Ω impendence to improve the impendence characteristics of a quarter-wave transformer (QTW and QTL) that is connected to the matching transformer which is connected with a directly coupled microstrip feeding. After those three-square-shaped patches, connected in a series in between them, a series connection is introduced. The X-band antenna is placed alone in the four corners of the antenna to transmit and receive the information at the same time. The final optimized parameters of the proposed X-band antenna are shown in Table 2. Figures 5 and 6 show the frequency response of all X-band ports. The impedance bandwidth covers from 9.51 GHz to 9.78 GHz.

2.3. Embedding S/X Shared Aperture Antenna. The geometry configuration of S/X-band SAA with the evolution stage is represented in Figure 7. The proposed contains 3 stages.

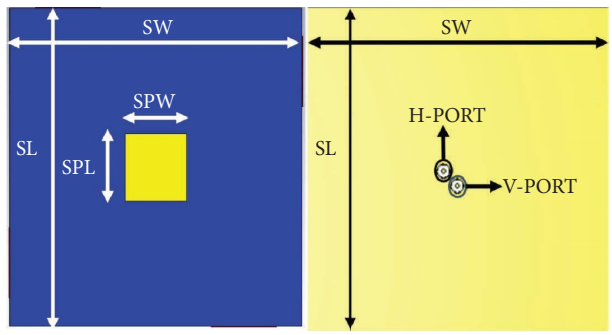

Figure 2: Geometry of S-band dual port element.

Table 1: Dimensions of the antenna design prototype of coaxial antenna.

Coaxial antenna parameters		
Parameters	Description	Value (mm)
HG	Height of the ground	0.035
HS	Height of the substrate	1.6
SPL	Patch length	21
SPW	Patch width	21
SL	Substrate length	100
SW	Substrate width	100
R1	Inner pin	0.65
R2	Outer pin	2.1765
XVF	*X*-coordinate of vertical polarization	0
YVF	*Y*-coordinate of vertical polarization	−4.5
XHF	*X*-coordinate of horizontal polarization	4.5
YHF	*Y*-coordinate of horizontal polarization	0

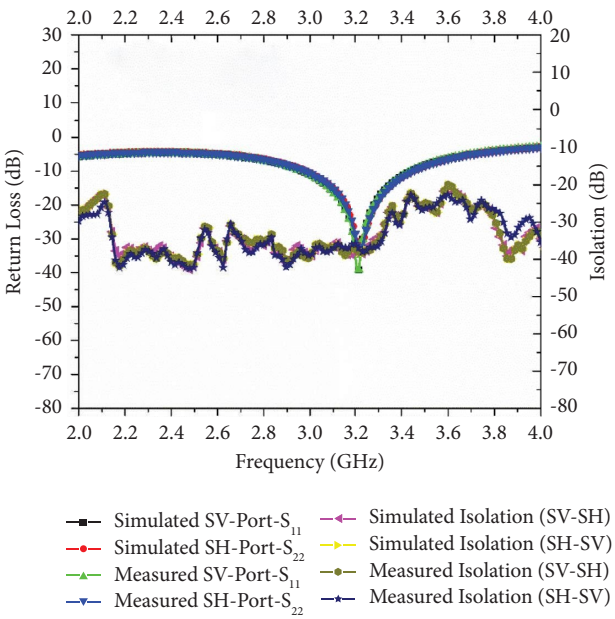

Figure 3: Frequency versus return loss and isolation of SV and SH-ports.

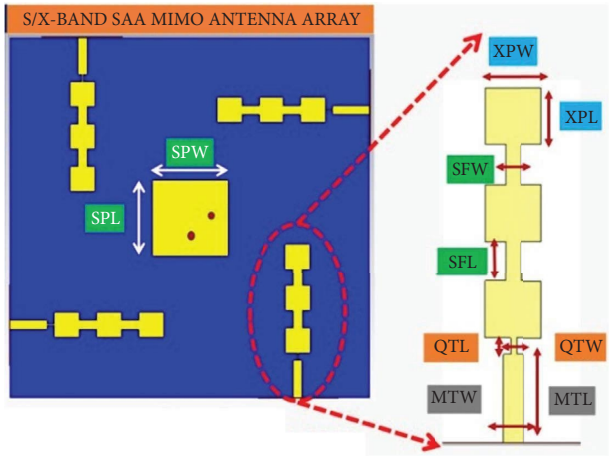

Figure 4: Geometry of X-band port element.

Table 2: Dimensions of the antenna design prototype of the linear array antenna.

1 × 3 linear array antenna		
Parameters	Description	Value (mm)
SL	Substrate length	100
SW	Substrate width	100
XPL	Patch length	6.85
XPW	Patch width	6.85
HG	Height of the ground	0.035
HS	Height of the substrate	1.6
SFW	Connection feed width-1	2.5
QTW	Connection feed width-2	0.28
MTW	Connection feed width-3	2.46
SFL	Connection feed length-1	4.85
QTL	Connection feed length-2	2
MTL	Connection feed length-3	10.25

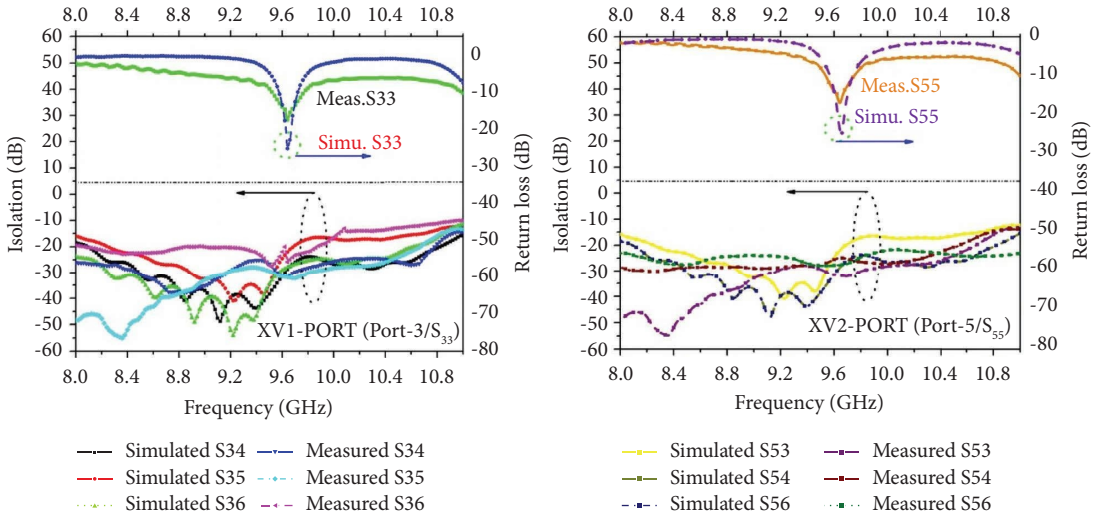

Figure 5: Frequency versus return loss and isolation of XV1 and XV2-ports.

Stage one consists of a single patch antenna which is fed in a coaxial manner both in vertical and horizontal polarizations which resonates at 3.2 GHz (S-band). The array consists of a 1 × 3 vertical series feed presented along four corners of the antenna with the single port which is fed with the direct coupling method and resonates at 9.65 GHz (X-

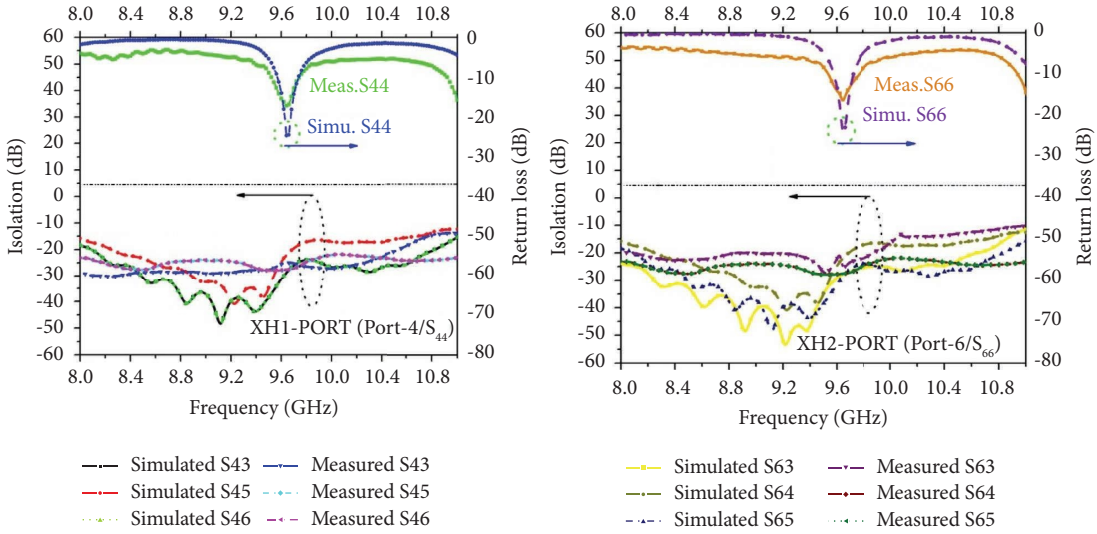

Figure 6: Frequency versus return loss and isolation of XH1 and XH2-ports.

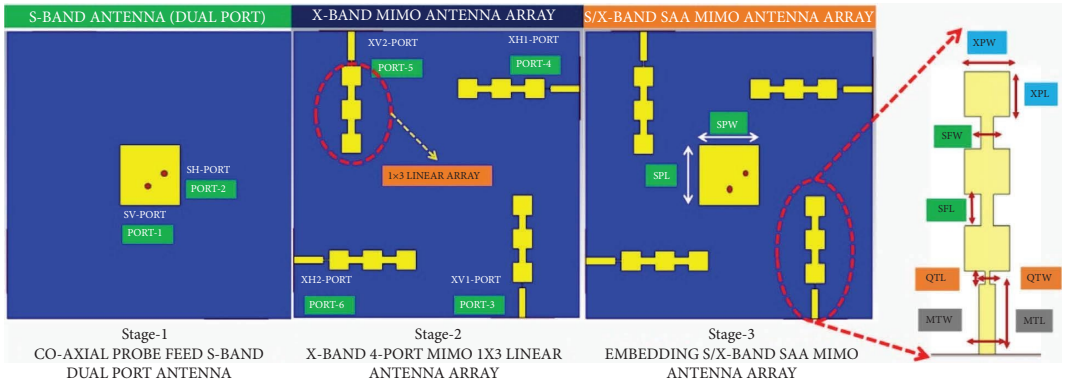

Figure 7: S/X-SAA geometry of evolution stages.

band). The final optimized parameters of the S/X Antenna are shown in Table 3. Figures 8 and 9 show the surface current distribution of S-Band and X-Band SAA at 3.2 GHz and 9.65 GHz, respectively. Figures 8(a) and 8(b) represent the surface current distribution of vertical and horizontal ports, respectively. Figures 9(a)–9(d) represent the surface current distribution of X-Band ports, i.e., XV1, XH1, XH2, and XV2, respectively.

3. Simulated and Experimental Results and Analysis

The S/X dual band dual polarization array prototype with frequencies of 3.2 GHz and 9.65 GHz for S- and X-bands, respectively, is fabricated and measured to verify the design as shown in Figure 10; the prototype is indulged with S/X-bands. The S-parameters are measured using a keysight microwave vector network analyzer.

The measured return loss S11 of the proposed S/X-band SAA is presented in Figure 11. The results show measured return loss bandwidth from 3.18–3.30 GHz at S-band for both vertical and horizontal polarizations and 9.51–9.78 GHz at X-band for both vertical and horizontal polarizations with a resonant frequency of 3.2 GHz and 9.65 GHz, respectively. The results agree well with simulated and measured antenna parameters. Isolation higher than 25 in both S- and X-bands is obtained. Figures 3, 5, and 6 represent S-parameter result of the S-band which resonates at 3.2 GHz of both vertical and horizontal polarizations as well as it also represents simulated and measured S-parameter results of remaining all X-Band ports, i.e., XV-1 Port (Port 3), XV-2 Port (Port-5), XH-1 Port (Port-4), and XH-2 Port (Port-6).

3.1. SV-Port (Port 1) and SH-Port (Port 2). SV-Port is used to resonate at a frequency of 3.2 GHz (S-band), and it is vertically polarized for the square shape antenna which is presented in the middle of the antenna. The return loss of port 1 is −22.8 dB at 3.2 GHz and isolation between the ports is −32 dB. Radiation patterns of the antenna system are simulated at either port at both S- and X-bands, as shown as radiation patterns of the S-band antenna at port-1 (V-port) at 3.2 GHz, which is two orthogonal planes (Phi = 0° and Phi = 90°) as shown in Figure 12(a). SH-Port is used to

Table 3: Dimensions of the antenna design prototype of the S/X antenna.

S/X antenna parameters		
Parameters	Description	Value (mm)
HG	Height of the ground	0.035
HS	Height of the substrate	1.6
SPL	Patch length	21
SPW	Patch width	21
LG	Substrate length	100
WG	Substrate width	100
R1	Inner pin	0.65
R2	Outer pin	2.17
XVF	*X*-coordinate of vertical polarization (SV-PORT)	0
YVF	*Y*-coordinate of vertical polarization (SV-PORT)	−4.5
XHF	*X*-coordinate of horizontal polarization (SH-PORT)	4.5
YHF	*Y*-coordinate of horizontal polarization (SH-PORT)	0
XPL	Patch length of array	6.85
XPW	Patch width of the array	6.85
SFW	Connection feed width-1	2.5
QTW	Connection feed width-2	0.28
MTW	Connection feed width-3	2.46
SFL	Connection feed length-1	4.85
QTL	Connection feed length-2	2
MTL	Connection feed length-3	10.25

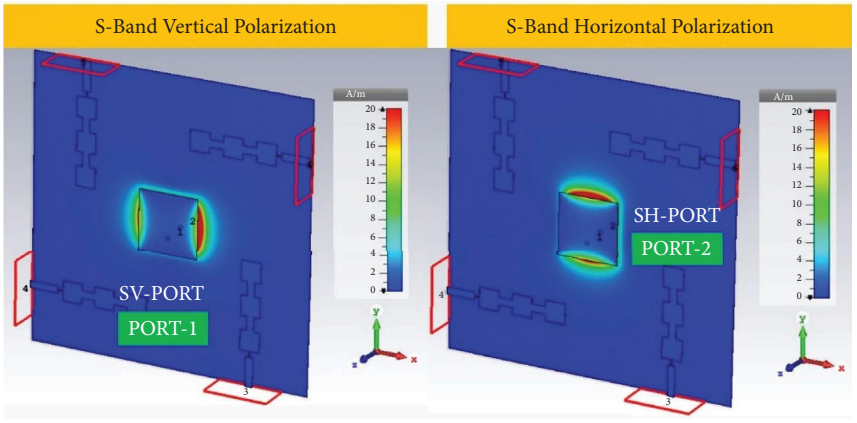

(a) (b)

Figure 8: (a) Surface current distribution of S-band port 1 (SV-PORT). (b) Surface current distribution of S-band port 2 (SH-PORT).

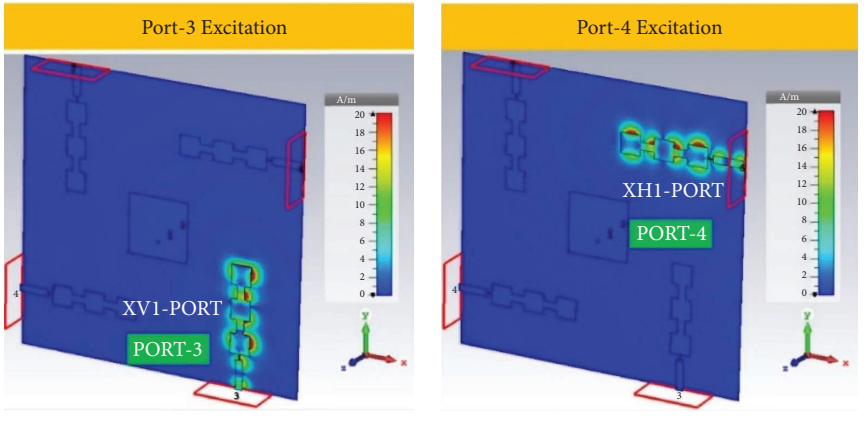

(a) (b)

Figure 9: Continued.

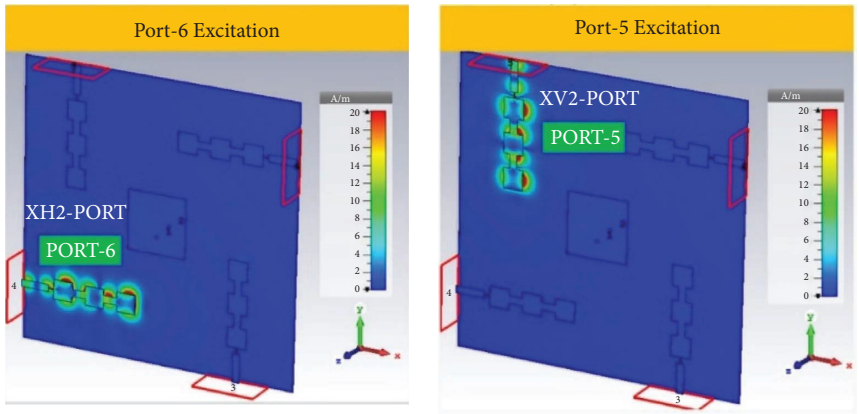

(c) (d)

Figure 9: (a) Surface current distribution of XV1-port (port-3). (b) Surface current distribution of XH1-port (port-4). (c) Surface current distribution of XH2-port (port-6). (d) Surface current distribution of XV2-Port (port-5).

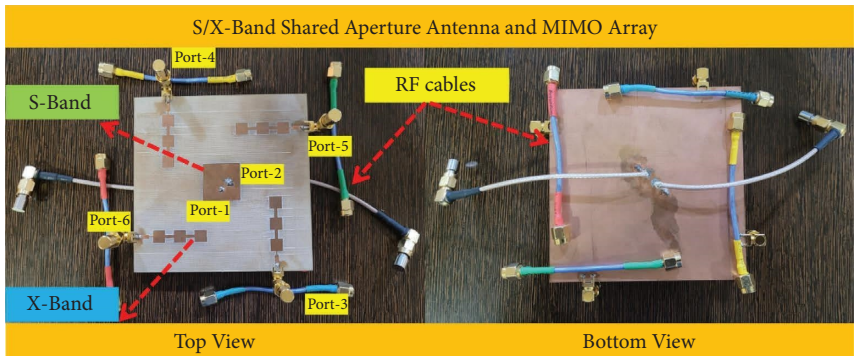

(a) (b)

Figure 10: Fabricated prototype top and bottom view photograph of S/X-DBDP SAA.

resonate at a frequency of 3.2 GHz (S-band), and it is horizontally polarized for the square shape antenna which is presented in the middle of the antenna. The return loss of port 2 is −22.8 dB at 3.2 GHz and the isolation between the ports is −32 dB. Simulated radiation patterns of the S-band antenna at port-2 (horizontal Port) at 3.2 GHz are two orthogonal planes (Phi = 0° and Phi = 90°) and are shown in Figure 12(b). Frequency versus return loss and isolation of SV and SH-Ports is represented in Figure 3.

3.2. XV1-Port (Port 3) and XV2-Port (Port 5). XV1 Port is used to resonate at a frequency of 9.65 GHz (X-band). It is in series fed with microstrip feeding, and it is situated in one of the corners of the final antenna. The return loss of port 3 is −45 dB at 9.65 GHz. Simulated radiation patterns of the X-band antenna at port-3 at 9.65 GHz are two orthogonal planes (Phi = 0° and Phi = 90°) and are shown in Figure 13(a). XV2-Port is used to resonate at a frequency of 9.65 GHz (X-band), and it is in series fed with microstrip feeding and situated in one of the corners of the final antenna. The return loss of port 5 is −40 dB at 9.65 GHz. Simulated radiation patterns of the X-band antenna at port-5 at 9.65 GHz are two orthogonal planes (Phi = 0° and Phi = 90°) and are shown in Figure 13(b). Frequency versus return loss and isolation of XV1 and XV2-Ports is represented in Figure 5.

3.3. XH1-Port (Port 4) and XH2-Port (Port 6). XH1-Port is used to resonate at a frequency of 9.65 GHz (X-band), and it is in series fed with microstrip feeding and is situated in one of the corners of the final antenna. The return loss of port 4 is −40 dB at 9.65 GHz. Simulated radiation patterns of the X-band antenna at port-4 at 9.65 GHz are two orthogonal planes (Phi = 0° and Phi = 90°) and are shown in Figure 14(a). XH2-port is used to resonate at a frequency of 9.65 GHz (X-band), and it is in series fed with microstrip feeding and is situated in one of the corners of the final antenna. The return loss of port 6 is −44 dB at 9.65 GHz. Simulated radiation patterns of the X-band antenna at port-6 at 9.65 GHz are two orthogonal planes (Phi = 0° and Phi = 90°) and are shown in Figure 14(b). Frequency versus return loss and isolation of XH1 and XH2-Ports is represented in Figure 6.

Good agreement between the simulated and measured results is obtained with directional characteristics. It can be found that the peak radiation happens in the broadside direction at these two frequencies. The polarization levels at 3.2 GHz in the Phi = 0° and Phi = 90°-planes in both vertical

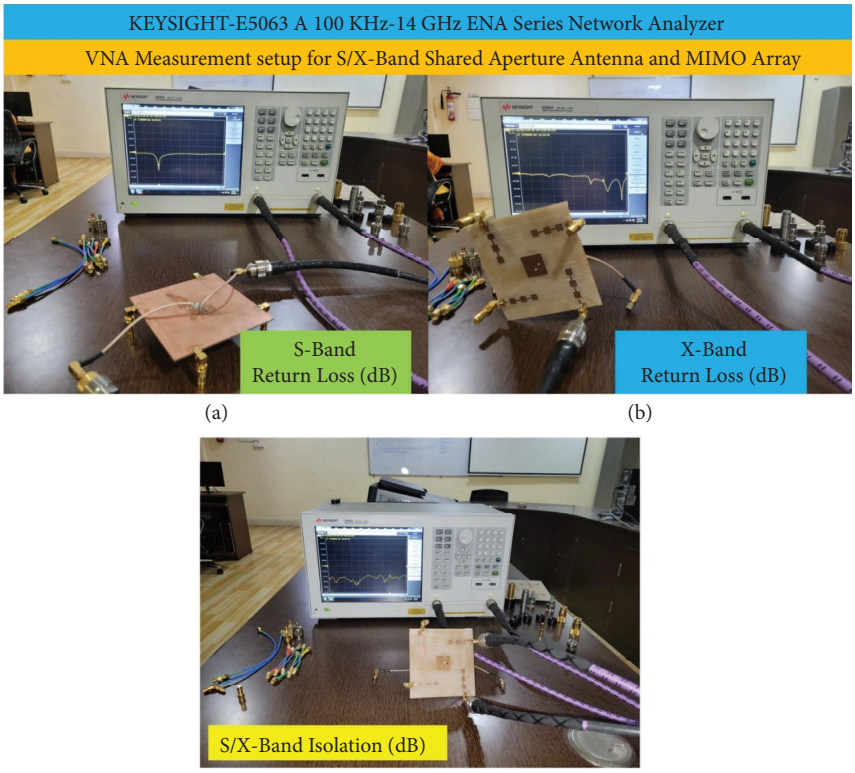

(a) (b)

(c)

Figure 11: (a) Experimental setup for testing the S-band element. (b) Experimental setup for testing the X-band element. (c) Testing the S/X-band isolation.

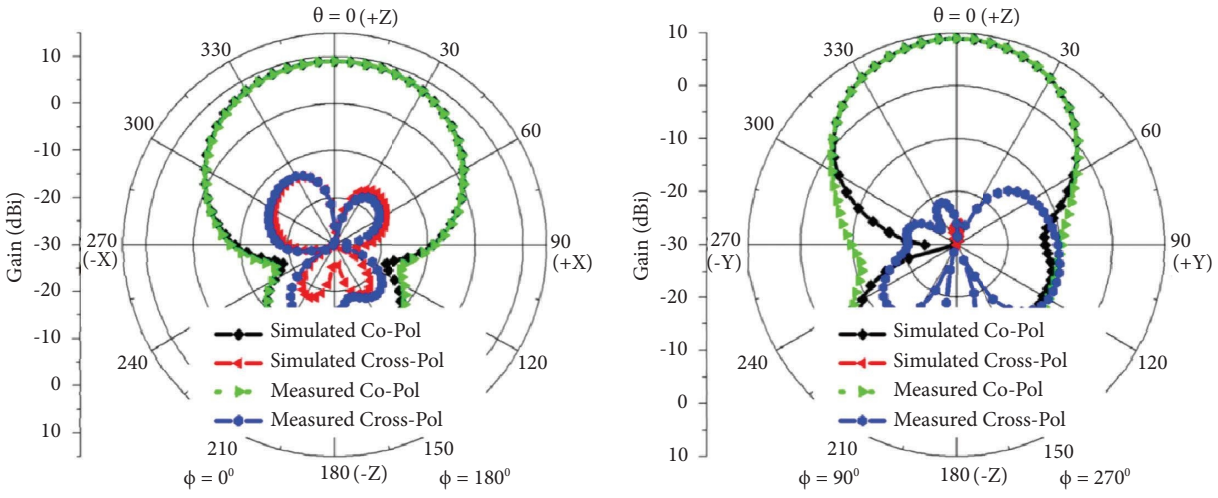

(a)

Figure 12: Continued.

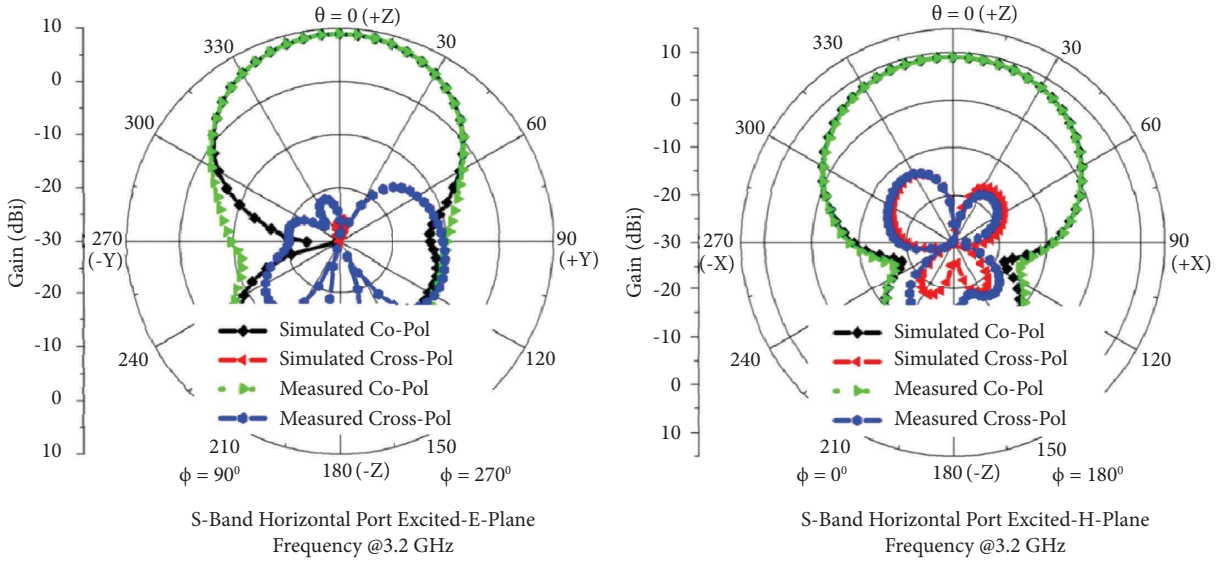

(b)

Figure 12: (a) Simulated and measured radiation pattern of port-1 excited phi = 0°-plane @3.2 GHz and port-1 excited phi = 90°-plane @3.2 GHz. (b) Simulated and measured radiation pattern of port-2 excited phi = 90°-plane @3.2 GHz and port-2 excited phi = 0°-plane @3.2 GHz.

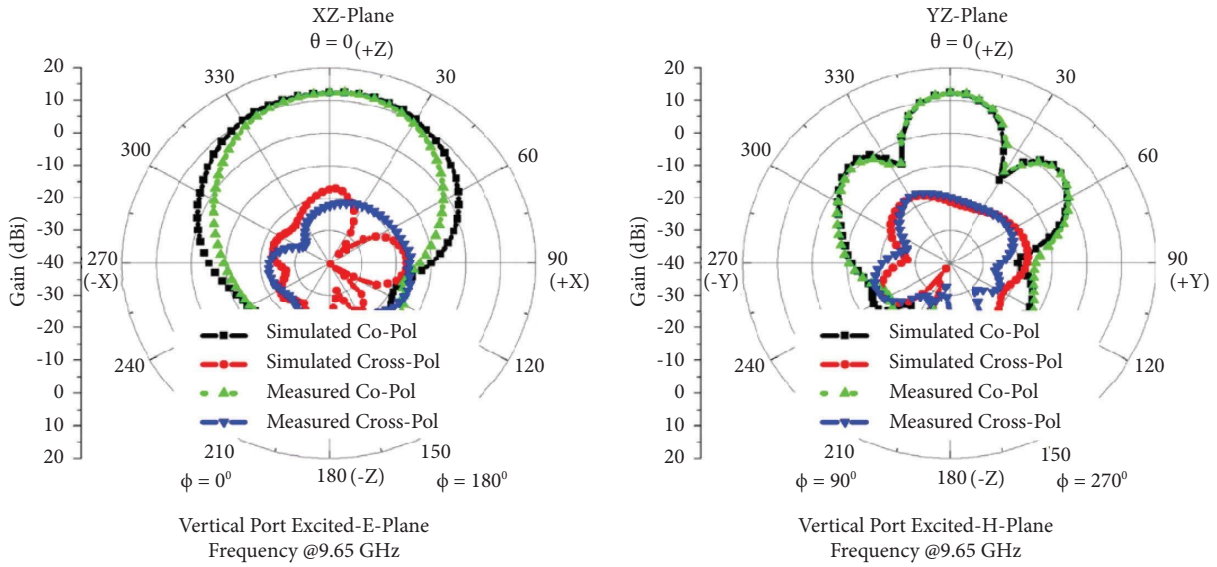

(a)

Figure 13: Continued.

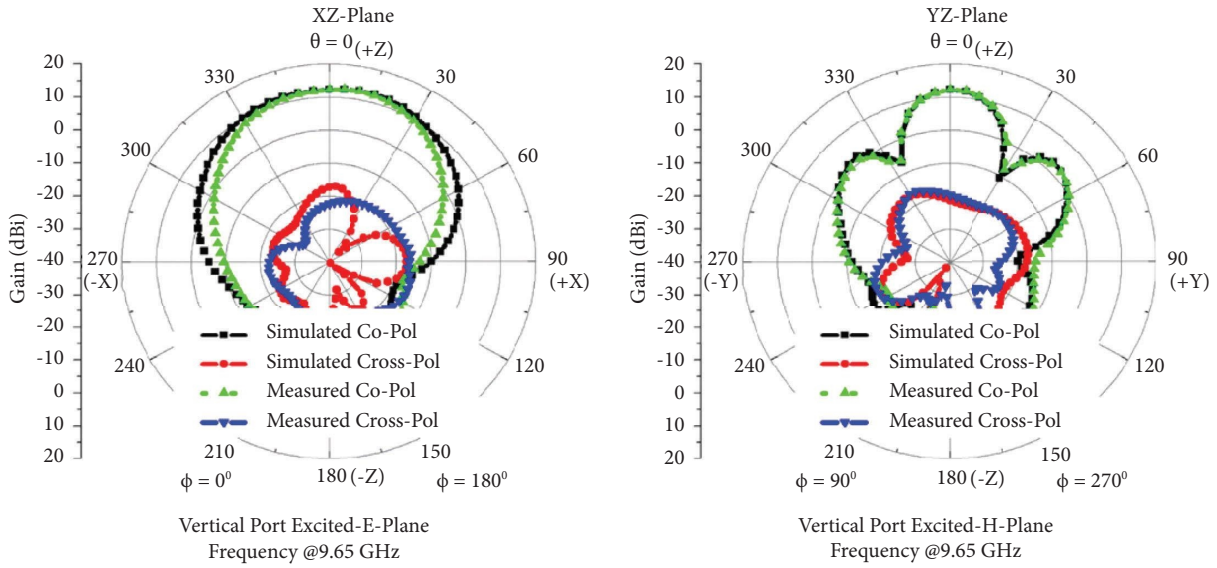

(b)

Figure 13: (a) Simulated and measured radiation pattern of port-3 excited phi = 0°-plane @9.65 GHz and port-3 excited phi = 90°-plane @9.65 GHz. (b) Simulated and measured radiation pattern of port-5 excited phi = 0°-plane @9.65 GHz and Port-5 excited phi = 90°-plane @9.65 GHz.

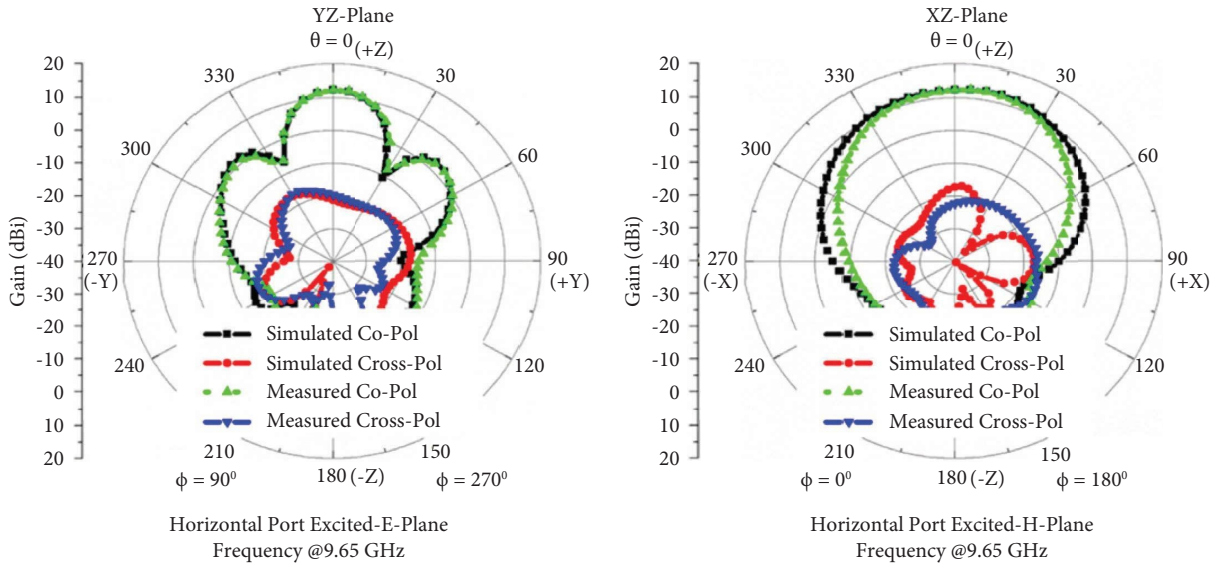

(a)

Figure 14: Continued.

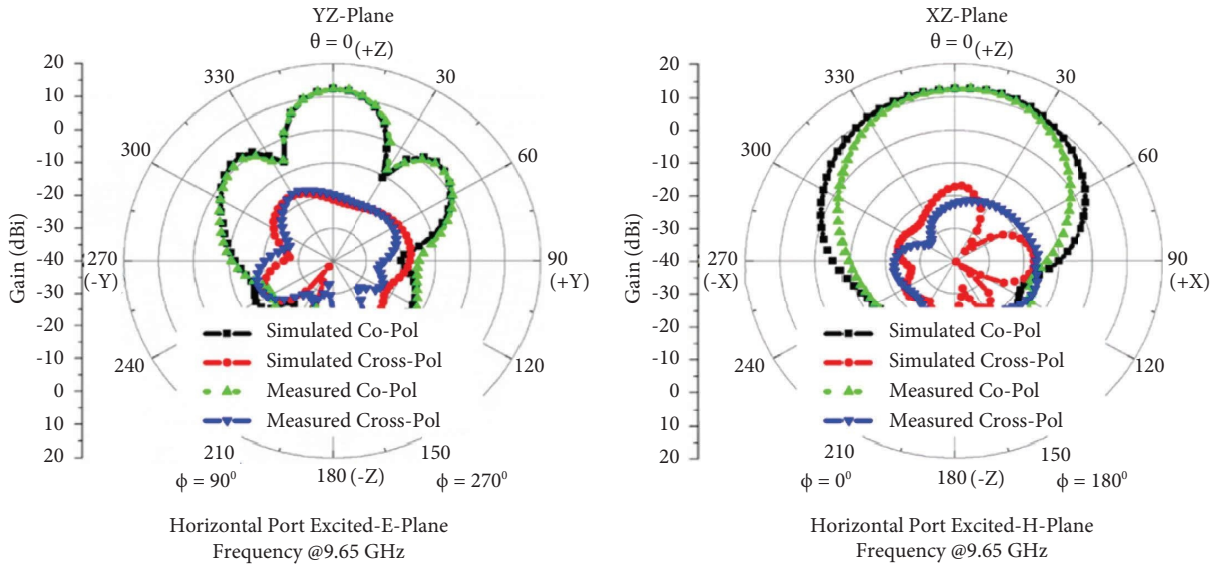

(b)

Figure 14: (a) Simulated and measured radiation pattern of port-4 excited phi = 90°-plane @9.65 GHz. and port-4 excited phi = 0°-plane @9.65 GHz. (b) Simulated and measured radiation pattern of port-6 excited phi = 90°-plane @9.65 GHz and port-6 excited phi = 0°-plane @9.65 GHz.

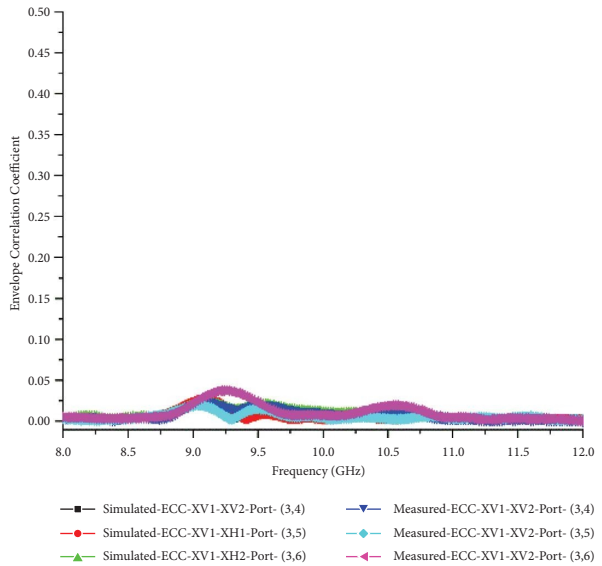

Figure 15: MIMO-Freq vs. ECC.

and horizontal polarizations are below −20 dB. The SLL level at 9.3 GHz in the Phi = 0° and Phi = 90° planes in all ports is below −15 dB. The simulated SLL is at −17.5 dB in both Phi = 0° and Phi = 90°-planes at 3.2 GHz in H-polarization and V-polarization at 9.65 GHz; the SLL remains below −21.5 dB in the Phi = 0° and Phi = 90°.

4. Analysis of MIMO Characteristics

MIMO is a technology related to the antenna for a wireless communication system in which multiple transmitters and receivers are present. The primary usage of the MIMO antenna is to optimize the data speed and minimize errors, and it can also boost the radiofrequency simultaneously, providing the most stable connection. The most significant advantage of having MIMO character is that it decreases packet loss, contains the following characteristics, and presents the analysis of the proposed antenna with respect to the following mentioned characteristics:

(1) Envelope correlation coefficient (ECC)
(2) Diversity gain (DG)
(3) Channel capacity loss (CCL)
(4) Mean effective gain

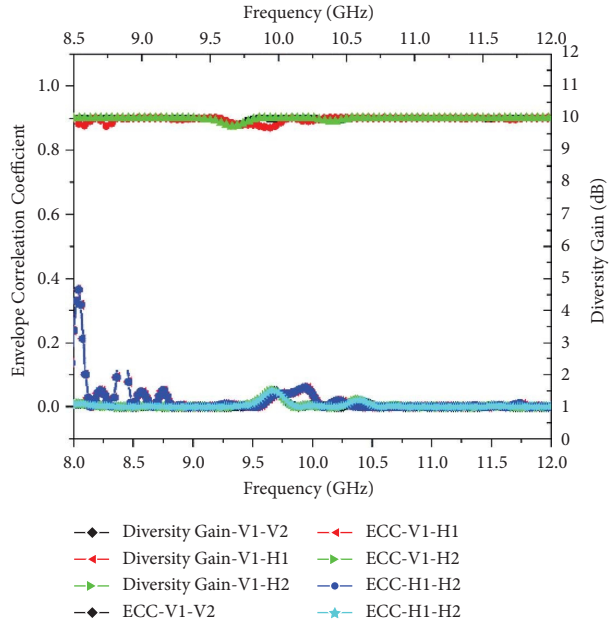

Figure 16: MIMO-Freq vs. ECC vs. DG.

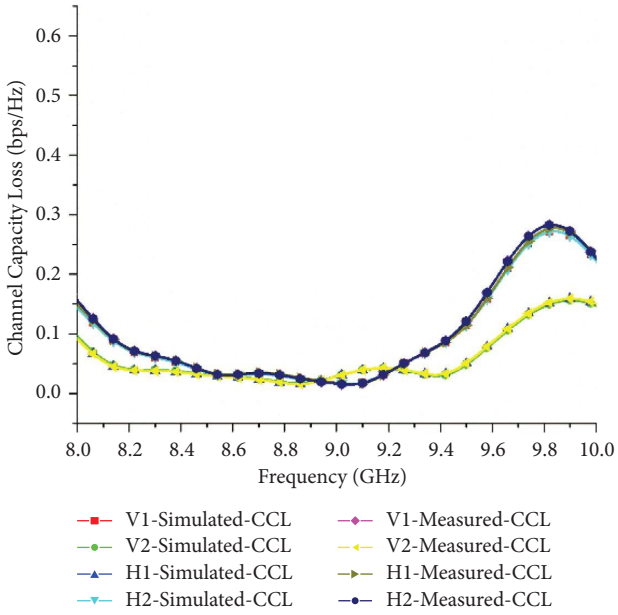

Figure 17: Freq vs. CCL.

(5) Mutual coupling

4.1. Envelope Correlation Coefficient. The envelope correlation coefficient is the correlation between two independent antennas polarized in two different directions, i.e., vertically and horizontally polarized. ECC value is considered while calculating the antenna radiation pattern, polarization, and relative phase of the fields between the two antennas. Equation (1) represents the envelope correlation coefficient present in mathematical form:

$$\mathrm{ECC} = \frac{\left(\left|S_{11}^{*}S_{12} + S_{21}^{*}S_{22}\right|^{2}\right)}{\left(\left(1 - \left|S_{11}\right|^{2} - \left|S_{21}\right|^{2}\right)\left(1 - \left|S_{22}\right|^{2} - \left|S_{12}\right|^{2}\right)\right)}. \quad (1)$$

Equation (1) shows that ECC can be measured with network analyzer and 2-ports-parameter measurements. And, the values of simulated and measured values of ECC is

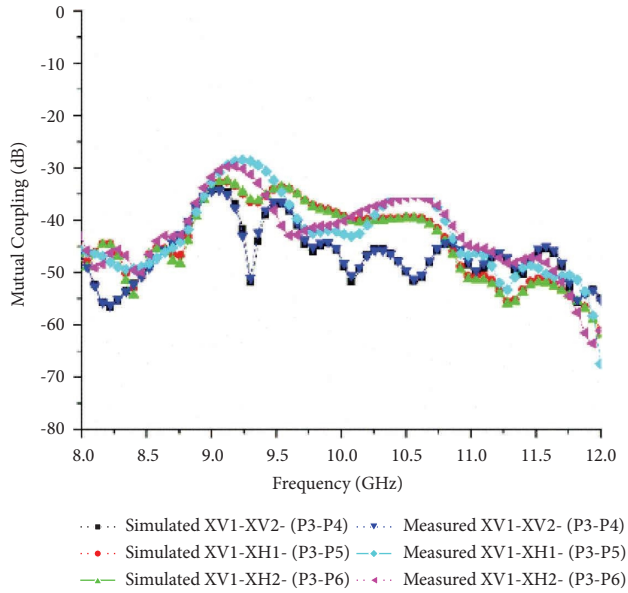

Figure 18: Mutual coupling.

good in agreement; i.e., both simulated and measured ECC value is less than 0.05 as shown in Figure 15.

4.2. Diversity Gain

$$\mathrm{DG} = 10\sqrt{\left(1 - \mathrm{ECC}^2\right)}. \tag{2}$$

Diversity gain is the value talk about the transmission power which can be reduced when a diversity scheme is introduced without a performance loss. Moreover, it is expressed in decibels. Specifically, this is the reduction in the fading margin obtained by reducing the fading with the smart antenna. Moreover, equation (2) represents diversity gain. Here, a diversity scheme is a technique used to enhance the message signal in a more reliable manner by using two or more communication channels with different characteristics. Diversity gain is achieved as below 9.5 dB for all X-band Ports which was represented in Figure 16.

4.3. Mean Effective Gain. Diversity performance analysis mean effective gain is an important parameter and is defined as the mean received power in the fading environment.

$$\mathrm{MEG} = 0.5\left(1 - \sum_{j=1}^{k}\left|S_{ij}\right|\right) = \mu i\mathrm{rad}. \tag{3}$$

Here, K denotes the number of antennas, i represents the antenna under observation, and $\mu i\mathrm{rad}$ is the radiation efficiency. For good diversity performance, the practical standard followed is that MEG should be $-3 \le \mathrm{MEG}\ (\mathrm{dB}) < -12$.

4.4. Channel Capacity Loss. It was enlisted among the MIMO performance parameters, thereby providing details of channel capacity losses of the system during the correlation effect. The CCL is calculated numerically by equations (4) and (5). Simulated and measured results of channel capacity loss are similar in a manner such that the CCL is obtained as below as 0.5 bps/Hz which is shown in Figure 17.

$$C(\mathrm{loss}) = -\det(\beta_R), \tag{4}$$

$$\beta_R = [R11\ R12\ R13\ R14\ R21\ R22\ R23\ R24\ R31\ R32\ R33\ R34\ R41\ R42\ R43\ R44], \tag{5}$$

where $Rii = 1 - (\Sigma Nj = 1|Sij|2)$ and $Rij = -(S * iiSij + S * jiSij)$

4.5. Mutual Coupling. Mutual coupling in two different antennas is related to the current distribution on the surface antenna; if the current flows in the same direction on the adjacent sides of both antennas, the mutual coupling increases. Similarly, if the currents are in the opposite direction, the induced mutual coupling is suppressed such that, for all X-band ports, mutual coupling is measured and simulated that was represented in the following figure, and it shows a very good agreement between them. Mutual coupling is obtained in the range of −30 dB to −55 dB as shown in Figure 18.

Table 4 shows the comparison of the author's work with the already existing works related to the proposed design. The antennas proposed in the article [1–8, 10, 15, 16] are operated in dual-band frequency. Still, all of them achieve low isolation compared to the proposed antenna in which

Table 4: Comparison of the previous works with proposed antenna.

Article	Year	Frequency (S/X)	Antenna element	Size W × L × T	Gain (dB)	Side lobe level (dB)	Co-polarization (S/X)	Isolation	Bandwidth	Application
1	1995	2.85 GHz/ 8.65 GHz	RT duroid 5880	$38 \times 8 \times 0.8\ mm^3$	11.6	NA	NA	NA	NA	SAR/GPS
2	2007	3.05 GHz/ 9.6 GHz	Multiple elements	$160 \times 100 \times 7.1\ mm^3$	NA	−10	−26 dB/−31 dB	−20 dB	1.75 GHz	Radar
3	2009	3 GHZ/ 10 GHz	RT duroid 5880	$183 \times 106 \times 0.13\ mm^3$	18.3	−13 (X) No SL (S)	−20 dB/−17 dB	>25 dB	1 GHz (S, X)	Aircraft
4	2010	3~3.3 GHz/ 9~11 GHz	RT duroid 5880	$196 \times 128 \times 6.5\ mm^3$	10 (S) 20.3 (X)	−19 (S) −10 (X)	−21 dB/−20 dB	>15 dB	300 MHz (S) 2 MHz (X)	Radar
5	2012	3.25 GHz/ 9.2 GHz	Taconic TLC	$28.5 \times 28.5 \times 2.7\ mm^3$	11 (S) 18.5 (X)	−17 (S) −10 (X)	−18 dB/−17.5 dB	>15 dB	0.62 GHz (S) 2.7 GHz (X)	Radar
6	2017	2.5 GHz/ 8.2 GHz	RT duroid 5880, air gap	$95 \times 95 \times 2.5\ mm^3$	7.5 dB (S) 10.5 dB (X)	NA	−35 dB/−12 dB	38 dB	0.23 GHz (S) 0.8 GHz (X)	SAR
7	2017	2.5 GHz/ 8 GHz	RT duroid 5880	$140 \times 140 \times 64\ mm^3$	8 dB (S) 11.5 dB (X)	NA	−8 dB/−20 dB	30 dB	0.18 GHz (S) 0.94 GHz (X)	Radar
8	2018	2.5 GHz/ 7 GHz	Arlon	—	8.5 dB (S) 10.8 dB (X)	NA	NA	32 dB	0.59 GHz (S) 1.26 GHz (X)	Aircraft
9	2017	NA	NA	NA	NA	NA	NA	NA	NA	SAR
10	2017	3.2 GHz/ 9.3 GHz	RT duroid 5880	$100 \times 100 \times 1.6\ mm^3$	8.4 dB (S) 10.5 dB (X)	−17.9 (S) −22.4 (v/X), −13.5 (h/X)	−20 dB/−15 dB	30 dB	0.3 GHz (S) 0.16 GHz (X)	SAR
11	2018	9.65 GHz (X)	RT duroid 5880	$80 \times 180 \times 0.8\ mm^3$	19 dB	−10 (v), −22 (h)	−30 (X)	−25 dB	0.5 GHz (X)	SAR
12	2018	9.65 GHz (X)	RT duroid 5880	$60 \times 60 \times 1.5\ mm^3$	11.04 dB	(−27, −25) (v) (−13.3, −12.3) (h)	−30 (X)	−20 dB	0.16 GHZ (X)	SAR
13	2019	21 GHz	RT duroid 5880	$15 \times 120 \times 1.5\ mm^3$ (UAD) $15 \times 100 \times 0.787\ mm^3$ (CAD)	15.3 dB (UAD) 17.4 dB (CAD)	15.3 (UAD) 17.4 (CAD)		NA	1.1 GHz (X)	Airborne
14	2019	9.65 GHz	RT duroid 5880	$50 \times 80 \times 1.5\ mm^3$	12.2 dB	−25.1 (E), −10.5 (H)	−31 (E), −28 (H)	NA	0.2 GHz (X)	SAR
15	2020	9.65 GHz (X), 21 GHz (K)	NA	$150 \times 150 \times 1.6\ mm^3$	20 dB (X), 15 dB (K)	−15 dB (X), −25 dB (K)	>25 dB (X, K)	>25 dB (X, K)	200 MHz	Airborne
16	2021	2.7 GHz (S), 9.7 GHz (X)	RT duroid 5880	$125 \times 125 \times 8\ mm^3$	8.4 dB (S), 21.7 dB (K)	−13.7 (v/S), −14.6 (h/S), −11.8 (v/X), −11.3 (h/X)	−24 (E/S), −26.1 (H/S), −33 (E/X), −20 (H/X)	>25 dB (S, X)	0.2 GHz (S) 0.5 GHz (X)	SAR
17	2022	5 GHz	RT duroid 5880	$6.75 \times 14.37 \times 0.32\ mm^3$	5.9 dB	NA	NA	−21.3	0.16 GHz	5 G
18	2022	6 GHz	NA	$30 \times 30 \times 1.6\ mm^3$	4.65 dB	NA	NA	−18	0.46 GHz 2.45 GHz	5 G
19	2022	6 GHz	NA	$75 \times 75 \times 18.75\ mm^3$	5.44 dB	NA	NA	−11	2 GHz	5 G
20	2007	NA	NA	NA	NA	NA	NA	NA	NA	NA

Table 4: Continued.

Article	Year	Frequency (S/X)	Antenna element	Size W × L × T	Gain (dB)	Side lobe level (dB)	Co-polarization (S/X)	Isolation	Bandwidth	Application
21	2022	5.57 GHz	RT duroid 5880	$160 \times 70\ mm^2$	6.6–12.4 dB	−13.8 dB	NA	−30	0.05 GHz	5 G
22	2014	1.75 GHz 3 GHz 4.5 GHz 6 GHz	FR-4	NA	1.35 dB 4.08 dB 4.22 dB 7.34 dB	NA	NA	−10–15	0.25 GHz	Wireless communication
23	2021	Sub-6 GHz	FR-4	$280.5 \times 56.1 \times 2\ mm^3$	12.95 dB	NA	NA	NA	140 MHz	5 G
24	2014	1.8 GHz	FR-4	$90 \times 90 \times 1.6\ mm^3$	9.9 dB	NA	NA	−18	246 MHz	4 G
25	2014	2.45 GHz 3.5 GHz 5.25 GHz	FR-4	$8.8 \times 9 \times 1.6\ mm^3$	4.3 dB 6 dB 7.6 dB	NA	NA	−10	0.11 GHz 0.47 GHz 1.1 GHz	WiMAX
26	2018	3.2 GHz 5.5 GHz	FR-4	$14 \times 15 \times 1\ mm^3$	7-8 dB	NA	NA	>−10 dB	0.4 GHz 0.5 GHz	5G
27	2022	2.6 GHz 3.5 GHz	RT duroid 5880	NA	11.25 dB	NA	−20 dB	>−27 dB	0.22 GHz	5G
28	**Proposed work**	3.2 GHz (S) 9.65 GHz (X)	FR-4	$100 \times 100 \times 1.6\ mm^3$	7.2 dB (S) 12.4 dB (X)	−16.9 (v/S), −17.2 (h/S), −18.2 (3/X), −16.1 (4/X) −21.2 (5/X), −19.7 (6/X)		−39.4 dB	0.12 GHz (S) 0.27 GHz (X)	SAR

X = X-band frequency, S = S-band frequency, UAD = uniform amplitude distribution, CAD = chebyshev amplitude distribution, E = electric field plane, H = magnetic field plane, V = vertical polarization, H = horizontal polarization, mm = millimetre, L = length, W = width, and H = height.

Table 5: Comparison of the previous works with proposed antenna in terms of MIMO parameters.

Article	Frequency	Antenna element	ECC	DG	CCL	Mutual coupling
[17]	Sub 6 GHz	RT-duroid 5880	<0.05 dB	10 dB	NA	NA
[18]	LTE and sub 6-GHz	FR-4	<0.012 dB	9.98 dB	0.3 bits/Hz	<18 dB
[19]	Sub 6 GHz	FR-4	<0.02	NA	85 bps/Hz	NA
[20]	NA	NA	NA	NA	NA	NA
[21]	Sub 6 GHz	RT-duroid 5880	<0.05 dB	~10 dB	NA	NA
[22]	1.75 GHz 3, 4.5, 6 GHz	FR-4	<0.5 dB	NA	0.3 bits/Hz	NA
[23]	Sub 6 GHz (3.3–3.8 GHz)	FR-4	NA	NA	NA	12.3 dB
[24]	1.8 GHz	FR-4	0.004 dB	~10 dB	NA	NA
[25]	2.46–2.6 GHz, 3.37–3.75 GHz, 5.2–5.87 GHz	FR-4	<0.1 dB	−9.75 (EDG)	NA	NA
[26]	Sub 6 GHz (LTE bands 42/43 and LTE band 46)	FR-4	<0.15 dB	NA	11.5–15.7 bps/Hz	NA
[27]	Sub 6 GHz (4.25 GHz)	RT-duroid 5880	<0.10 dB	10 dB	NA	NA
Proposed work	3.2 GHz 9.65 GHz	FR-4	<0.05 dB	9.5 dB	0.5 bps/Hz	−30 dB to −55 dB

ECC = envelope correlation coefficient, DG = diversity gain, EDG = effective diversity gain, and CCL = channel capacity loss.

isolation is performed at more than 38 dB. While comparing the bandwidth in [4], the S-Band is relatively low compared to our proposed antenna, which achieves a frequency of 0.12 GHz when compared to X-Band frequency, i.e., 0.27 GHz, which is superior bandwidth compared to the articles [4, 10, 12, 14, 15]. Regarding the application concern, we need to take the antenna size. Size complexity is present in terms of length, breadth, and thickness when comparing the dimensions of the proposed antenna with the antennas of articles [2–8, 10–16]. Our antenna is small in size and produces better compatibility. As we know, the reduction of the side lobe level is the secondary target, but in [2–5, 10, 12, 14] research articles, they proposed an antenna with minimal side lobe level; when comparing to the antennas, our antenna achieves a better side lobe level which helps the transmission works effectively in their respective bands. The use of Lossy Substrate FR-4 with 4.4 permittivity results in less gain and reasonable isolation. It can be enhanced by changing the antenna element with RT-DUROID 5880, which has a permittivity of 2.2.

Table 5 represents the comparison of MIMO characteristics with X-band antenna. Since while comparing to all 5G MIMO antenna which are cited in Table 5 with X-Band, MIMO antenna is achieved better MIMO characteristics such that it is capable to perform multi-input and multi-output operation while used in real time application.

5. Conclusion

The proposed antenna operating at both S and X-bands for SAR applications is included in this paper. In this proposed antenna, single square-shaped element with coaxial feeding is used to operate at the S-band frequency band and the remaining four 1×3 series fed antenna is used to operate at the X-band frequency band. Square-shaped coaxial fed S-band antenna is fed in a dual-polarized manner which is orthogonal to each other. The proposed antenna is simulated in computer simulation tool–2021 (CST-2021). Since X-band antenna is MIMO based antenna, we achieved results such as ECC is obtained as <0.05, diversity gain as 9.5 dB, channel capacity loss as 0.5 bps/Hz, and mutual coupling obtained as in the range −30 dB to −55 dB in the desired band. By using RT-Duroid 5880 as an antenna element, we can achieve better return loss in both the S-band and X-band. The total size of the proposed antenna is $100\ \text{mm} \times 100\ \text{mm} \times 1.6\ \text{mm}$ which occupies less area.

Data Availability

The data used to support the study are available from the first author upon request.

Conflicts of Interest

The authors declare that there are no conflicts of interest.

References

[1] C. Salvador, L. Borselli, S. Maci, and A. Falciani, "Dual frequency planar antenna at S and X bands," *Electronics Letters*, vol. 31, no. 20, pp. 1706-1707, 1995.

[2] X. Qu, S.-S. Zhong, and Y.-M. Zhang, "Dual-banddual-polarised microstrip antenna array for SAR applications," *Electronics Letters*, vol. 42, pp. 1376-1377, 2006.

[3] S.-H. Hsu, Y.-J. Ren, and K. Chang, "A dual-polarizedplanar-array antenna for S-band and X-band airborne applications," *IEEE Antennas and Propagation Magazine*, vol. 51, no. 4, pp. 70–78, 2009.

[4] M.-S. Han, J. M. Kim, D. S. Park, H. J. Kim, and J. H. Choi, "Dual polarized array antenna for S/X band active phased array radar application," *Journal of electromagnetic engineering and science*, vol. 10, no. 4, pp. 309–315, 2010.

[5] L. Youngki, "Design of a bandwidth enhanced dual-banddual-polarized array antenna," *IEICE Proceeding Series*, vol. 15, pp. 4A2–1, 2012.

[6] P. Mathur and G. Kumar, "Antenna at S-band as ground for array at X-band in dual frequency antenna at S/X-bands," *Progress In Electromagnetics Research Letters*, vol. 71, pp. 15–22, 2017.

[7] P. Mathur and G. Kumar, "Dual-frequency microstrip antenna at S and X bands with higher-order mode suppression technique," *IET Microwaves, Antennas & Propagation*, vol. 12, no. 4, pp. 583–587, 2018.

[8] K. Wang, X. Liang, W. Zhu et al., "A dual-widebanddual-polarizedaperture-shared patch antenna with high isolation," *IEEE Antennas and Wireless Propagation Letters*, vol. 17, no. 5, pp. 735–738, 2018.

[9] V. K. Kothapudi and V. Kumar, "Shared aperture antenna technology for SAR: a review of the theory and applications," *Journal of Engineering Science and Technology Review*, vol. 10, pp. 41–54, 2017.

[10] V. K. Kothapudi and V. Kumar, "A single layer S/X-band series-fed shared aperture antenna for SAR applications," *Progress in Electromagnetics Research C*, vol. 76, pp. 207–219, 2017.

[11] V. K. Kothapudi and V. Kumar, "A 6-porttwo-dimensional 3×3 series-fed planar array antenna for dual-polarizedX-band airborne synthetic aperture radar applications," *IEEE Access*, vol. 6, Article ID 12001, 2018.

[12] K. Venkata Kishore and V. Kumar, "Compact 1× 2 and 2× 2 dual polarized series-fed antenna arrays for X-band airborne synthetic aperture radar applications," *Journal of electromagnetic engineering and science*, vol. 18, no. 2, pp. 117–128, 2018.

[13] V. K. Kothapudi and V. Kumar, "SFCFOS uniform and Chebyshev amplitude distribution linear array antenna for K-band applications," *Journal of electromagnetic engineering and science*, vol. 19, no. 1, pp. 64–70, 2019.

[14] V. K. Kothapudi and V. Kumar, "Vertical polarized 1× 3 series-fed linear array with gain and front-to-back ratio enhancement for airborne SAR-X applications," *Progress in Electromagnetics Research M*, vol. 80, pp. 169–179, 2019.

[15] V. K. Kothapudi and V. Kumar, "Hybrid fed shared aperture antenna array for X/K-band airborne synthetic aperture radar applications," *IET Microwaves, Antennas & Propagation*, vol. 15, no. 1, pp. 93–102, 2021.

[16] V. K. Kothapudi and V. Kumar, "A multi-layer S/X-band shared aperture antenna array for airborne synthetic aperture radar applications," *International Journal of RF and Microwave Computer-Aided Engineering*, vol. 31, no. 8, Article ID e22720, 2021.

[17] I. S. Masoodi, I. Ishteyaq, and K. Muzaffar, "Extra compact two element sub 6 GHz MIMO antenna for future 5G wireless applications," *Progress In Electromagnetics Research Letters*, vol. 102, no. 2022, pp. 37–45, 2022.

[18] D. Sharma, R. Kumar, and K. V. Rajesh, "Four-portdual-band MIMO antenna for LTE and sub 6-GHz 5G applications," *Journal of Engineering. Research*, vol. 10, 2022.

[19] T. G. Abouelnaga, I. Zewail, and M. Shokair, "16-Ports indoor base station MIMO array for sub-6 GHz 5G applications," *Telecommunication Systems*, vol. 80, 2022.

[20] S. H. Chae, S.-K. Oh, and S.-O. Park, "Analysis of mutual coupling, correlations, and TARC in WiBro MIMO array antenna," *IEEE Antennas and Wireless Propagation Letters*, vol. 6, pp. 122–125, 2007.

[21] J. Khan, S. Ullah, F. A. Tahir, F. Tubbal, and R. Raad, "A sub-6 GHz MIMO antenna array for 5G wireless terminals," *Electronics*, vol. 10, p. 3062, 2021.

[22] Y. K. Choukiker, S. K. Sharma, and S. K. Behera, "Hybrid fractal shape planar monopole antenna covering multiband wireless communications with MIMO implementation for handheld mobile devices," *IEEE Transactions on Antennas and Propagation*, vol. 62, no. 3, pp. 1483–1488, 2014.

[23] R. Darwin and P. Sampath, "Sub-6 GHz band massive MIMO antenna system for variable deployment scenarios in 5G base stations," *Microsystem Technologies*, vol. 28, no. 9, pp. 2047–2059, 2022.

[24] J. Nasir, M. H. Jamaluddin, M. Khalily, M. R. Kamarudin, I. Ullah, and R. Selvaraju, "A reduced size dual port MIMO DRA with high isolation for 4G applications," *International Journal of RF and Microwave Computer-Aided Engineering*, vol. 25, no. 6, pp. 495–501, 2015.

[25] H. S. Singh, G. K. Pandey, P. K. Bharti, and M. K. Meshram, "Design and performance investigation of a low profile MIMO/Diversity antenna for WLAN/WiMAX/HIPERLAN applications with high isolation," *International Journal of RF and Microwave Computer-Aided Engineering*, vol. 25, no. 6, pp. 510–521, 2015.

[26] Y. Li, C. Y. D. Sim, Y. Luo, and G. Yang, "Multiband 10-antenna array for sub-6 GHz MIMO applications in 5-G smartphones," *IEEE Access*, vol. 6, pp. 28041–28053, 2018.

[27] M. Alibakhshikenari, S. V. Bal, B. Harry et al., "An innovative antenna array with high inter element isolation for sub-6 GHz 5G MIMO communication systems," *Scientific Reports*, vol. 12, no. 1, pp. 1–13, 2022.

Hindawi
International Journal of Antennas and Propagation
Volume 2022, Article ID 8456936, 11 pages
https://doi.org/10.1155/2022/8456936

Research Article

A Wideband Eight-Element MIMO Antenna Array in 5G NR n77/78/79 and WLAN-5GHz Bands for 5G Smartphone Applications

Jun-Yi Jiang and Hsin-Lung Su

Department of Computer and Communication, National Pingtung University, Pingtung 900392, Taiwan

Correspondence should be addressed to Hsin-Lung Su; hlsu@mail.nptu.edu.tw

Received 19 August 2022; Accepted 5 October 2022; Published 16 November 2022

Academic Editor: Chow-Yen-Desmond Sim

In this paper, a wideband eight-element multiple-input multiple-output (MIMO) antenna array for 5G smartphone applications is presented. Each antenna is composed of a dual-arm tortuous monopole radiating element with a double-stub tuner and an open slot on the ground plane. Tuning stub microstrip lines are utilized to improve impedance matching. The operating bandwidth of the single antenna element is from 3200 to 6000 MHz with three resonant frequencies. The operating bandwidth covers the 5G new radio (NR) bands (n77/n78/n79) and the WLAN-5GHz band. The isolation of the proposed MIMO antenna array is above 10 dB in the entire operating band without any isolation elements. Furthermore, the proposed MIMO array was manufactured and measured. The measured results validate that the MIMO antenna array has a wide 6-dB impedance bandwidth from 3.2 to 6 GHz and the isolations are all more than 10 dB. The total efficiency ranges from 38% to 83%. The above results show that this MIMO antenna array can support 5G applications in smartphones.

1. Introduction

In recent years, people have pursued higher access rates and lower latency in the wireless network experience. Because the 4G LTE is no longer satisfied with current users, the 5G NR is proposed and rapidly expanding. The 3rd Generation Partnership Project (3GPP) has released some frequency bands, named n77 (3300–4200 MHz), n78 (3300–3800 MHz), and n79 (4400–5000 MHz) in its new specification for 5G NR. However, different countries have their own 5G frequency bands, but the selected frequency bands are always within those three mentioned frequency bands. Therefore, it is a good approach to design a wideband antenna that covers all 5G NR bands to comply with the specifications in the different countries.

MIMO technology is adopted to improve the access rate of mobile devices. The MIMO technology is widely used in 5G communication, and the access rate has been significantly improved by increasing the number of antenna array elements at the transmitting and receiving ends. It is easier to increase the number of antennas on the base station but is not in the smartphone. Because of the limited volume size of the smartphone, it is not easy to achieve high isolation of adjacent antennas without using any isolation elements and increasing the number of antennas simultaneously.

Some literature shows that the antenna itself is small but the distances between adjacent antennas are not close. Therefore, the isolation can reach more than 10 dB [1–8]. Some common techniques such as the neutralization line [9–11], self-isolated [12], polarization diversity [13], and decoupling by adding parasitic branches [9] or slots [14, 15] have been proposed and applied. Until now, many MIMO antenna array designs have been reported [1–16], and most of these papers proposed between 8 and 12 antenna elements array. It is not easy to obtain a wide-frequency bandwidth antenna with only one resonant mode to cover all 5G NR bands. Several articles have presented wideband antennas using multiple resonant modes [4–8, 15, 16]. For example, some papers present a wideband antenna composed of several individual elements which generated multiple and close resonant frequencies [4, 5, 7, 8]. In [6], this article presents a wideband loop antenna with creates a new

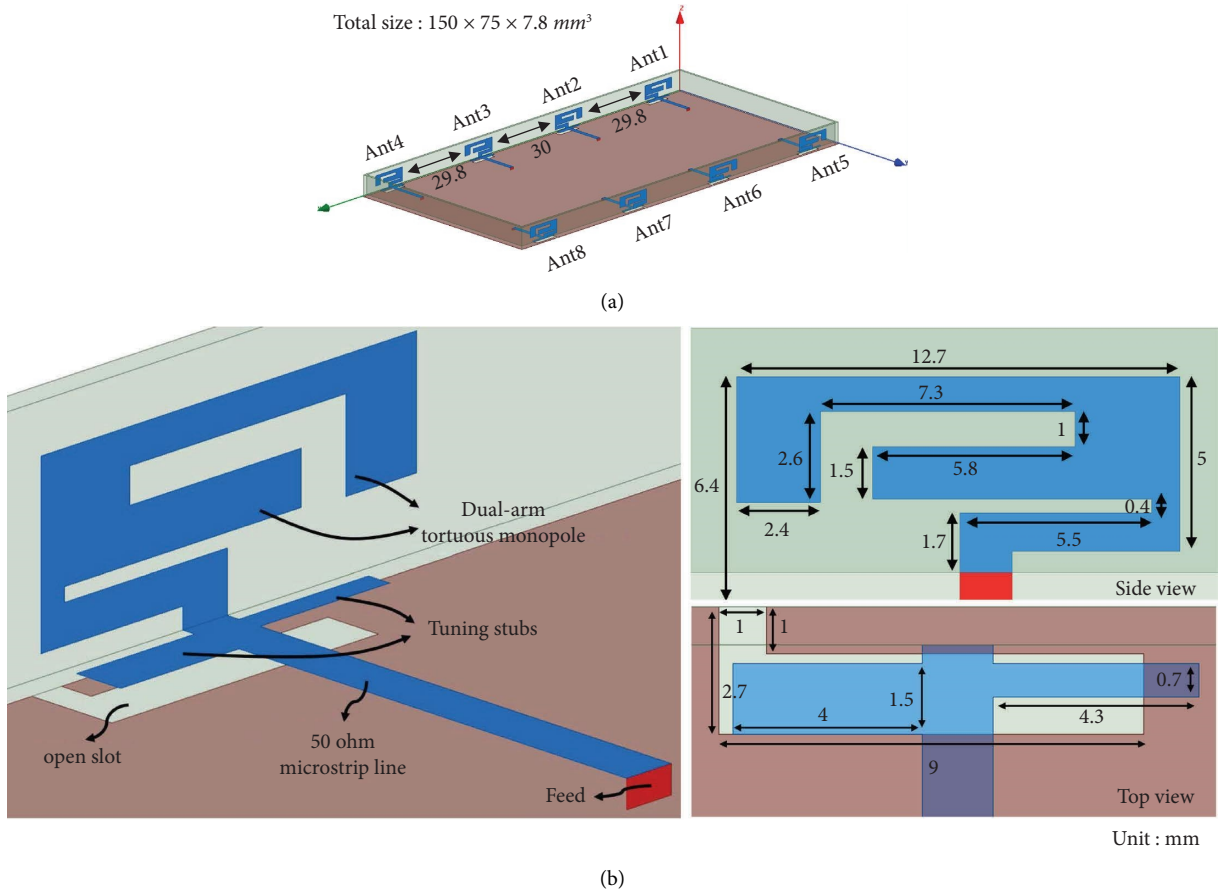

Figure 1: (a) The configuration of the MIMO antenna array and (b) the detailed parameters of the single antenna element.

resonant mode between the fundamental mode and the second harmonic mode. Therefore, this antenna creates three resonant modes which are 0.5 λ, 0.75 λ, and 1.0 λ, respectively, to obtain a wide frequency band. Creating different current paths on a single antenna element generates different resonant modes, such as the PIFA mode, the loop mode, and the slot mode, to compose a wide frequency band [16]. Most of the above studies fully cover the 5G NR bands (n77/n78/n79) and agree with the specification of 5G communications in different countries.

This article presents a wideband eight-element MIMO array with a simple structure for 5G NR smartphone applications. A dual-arm tortuous monopole antenna with an open slot to obtain a wide frequency bandwidth ranging from 3.3 to 5.95 GHz covers the 5G NR frequency bands and the WLAN-5 GHz band. The MIMO antenna array has isolation over 10 dB and is without any isolation elements or techniques.

2. Antenna Geometry and Design Steps

2.1. The Geometry of the Single Antenna Element. As shown in Figure 1(a), an eight-element antenna array is printed on the inner surface of two side edges of the smartphone with $150 \times 75 \times 7.8\,mm^3$. The antenna array is designed on a 0.8 mm thick FR4 substrate (relative permittivity 4.4 and loss tangent 0.02). The ground plane is installed on the bottom side of the smartphone substrate. The geometry and detail parameters of the single antenna element are depicted in Figure 1(b). The single antenna element includes two major parts, a dual-arm tortuous monopole element and an open slot on the ground plane, as shown in Figure 1(b). The single antenna element is fed by a 50 Ω microstrip line and the three-dimensional size of the proposed single antenna is $12.7 \times 6.4 \times 2.7\,mm^3$. The distances of each antenna are also depicted in Figure 1(a).

2.2. Design Steps of the Proposed Antenna Element. The design steps of this antenna and its corresponding S parameters are shown in Figure 2. Reference antenna 1 (Ref. 1) in Figure 2(a) is a tortuous monopole structure fed by a 50 Ω microstrip line, and it has one resonant frequency at approximately 3.8 GHz as the blue line shown in Figure 2(b). Worse impedance matching can be observed on the resonant frequency excited by the tortuous monopole structure. Therefore, Ref. 1 with loading a double-stub tuner on the feeding line to improve impedance matching, which forms reference antenna 2 (Ref. 2). The impedance matching of the resonant frequency at 3.8 GHz of Ref. 2 is greatly improved as the green line shown in Figure 2(b). Next, a dual-arm monopole structure is proposed in reference antenna 3 (Ref. 3) by etching an inverted-L slot on the tortuous monopole in

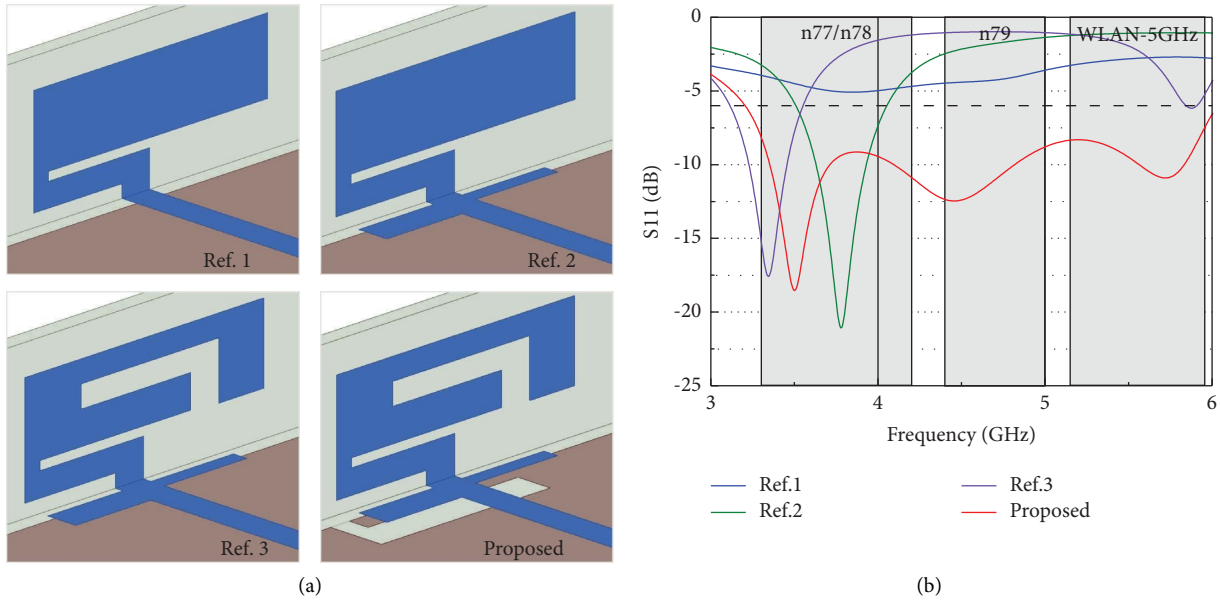

Figure 2: (a) The design steps and (b) its corresponding S parameters of the proposed antenna element.

Ref. 2. This introduces an additional resonant frequency at 5.9 GHz as the purple line in Figure 2(b). The resonant frequency at 3.8 GHz will shift to the lower frequency of approximately 3.4 GHz due to the lengthened electrical path caused by the inverted-L slot. Finally, the addition of an open slot on the ground plane forms the proposed antenna. An additional resonant frequency at 4.5 GHz is excited as the red line shown in Figure 2(b). The 6-dB impedance bandwidth of the proposed antenna is from 3200 to 6000 MHz and fully covers the required triple band.

To identify the excitation path of the resonant modes, the surface current distributions at 3.5, 4.5, and 5.7 GHz are shown in Figures 3 and 4. As shown in Figure 3(a), the current path ABCDEF (28.6 mm) of the dual-arm monopole structure excited at 3.5 GHz is approximately one-quarter wavelength long. However, the current distribution at 5.7 GHz consists of two current paths, as shown in Figure 3(b). The first one is the path ABCDFGH (28.6 mm) and two maximum currents with one current null can be observed on the path. The one-half-wavelength excitation can be inferred. The second one is the path ABCDE (19.1 mm), approximately one-quarter wavelength long. Because one maximum current on the path and a weak point at the end of the path can be observed. From the current path mentioned above, the resonant frequency at 3.5 GHz is generated by the longer arm of the dual-arm monopole structure. The resonant frequency at 5.7 GHz is collaboratively excited by the longer arm and the shorter arm of the dual-arm monopole structure. Next, the electric field and the current distribution of the open slot excited at 4.5 GHz are shown in Figures 4(a) and 4(b), respectively. There have some features that are worth mentioning. First, the direction of the electric field is perpendicular to the open slot path ABC, as shown in Figure 4(a). Second, the intensity of the electric field gradually decreases from the opening section to the closed section, and the current distribution gradually increases from the opening section to the closed section conversely, as shown in Figures 4(a) and 4(b). From those two features mentioned above, we can infer that the resonant frequency at 4.5 GHz is excited by the open slot on the ground plane.

2.3. Parametric Studies. To validate that the dual-arm monopole structure is responsible for the excitation of the resonant frequencies at 3.5 and 5.7 GHz and the open slot is responsible for the excitation of the resonant frequency at 4.5 GHz, parametric studies on L_1 (length of the longer arm), W_1 (width of the longer arm), L_2 (length of the shorter arm) and L_3 (length of the open slot) are investigated here. The corresponding location of the parameters is shown in Figure 5(a). Tuning L_1 will only affect the center frequency of the resonant frequency (f_1) at 3.5 GHz, which decreasing L_1 from 9.9 to 8.9 mm and the f_1 will shift from approximately 3.4 to 3.6 GHz, as shown in Figure 5(b). The optimum L_1 is chosen to be 9.4 mm because it can achieve a wide enough impedance bandwidth to cover the n77/78 bands and a good impedance matching (S_{11} reaches −15 dB) at the same time.

As shown in Figure 5(c), tuning W_1 will affect the f_1 and the resonant frequency (f_3) at 5.7 GHz simultaneously. When W_1 decreased from 1.5 to 0.5 mm, the f_1 and the f_3 will shift to the lower frequency without affecting the resonant frequency (f_2) at 4.5 GHz. The optimum W_1 is chosen to be 1 mm because the impedance bandwidth can fully cover the desired bands with the optimum performance both on bandwidth and impedance matching. If the W_1 is chosen to be 1.5 mm, then those resonant frequencies f_1 and f_3 are shifting to higher frequency but cannot cover the n77/78 bands.

Figure 5(d) shows that tuning L_2 will only affect the f_3 without affecting other resonant frequencies. When the L_2 increases from 5.3 to 6.1 mm, the resonant frequency f_3 will

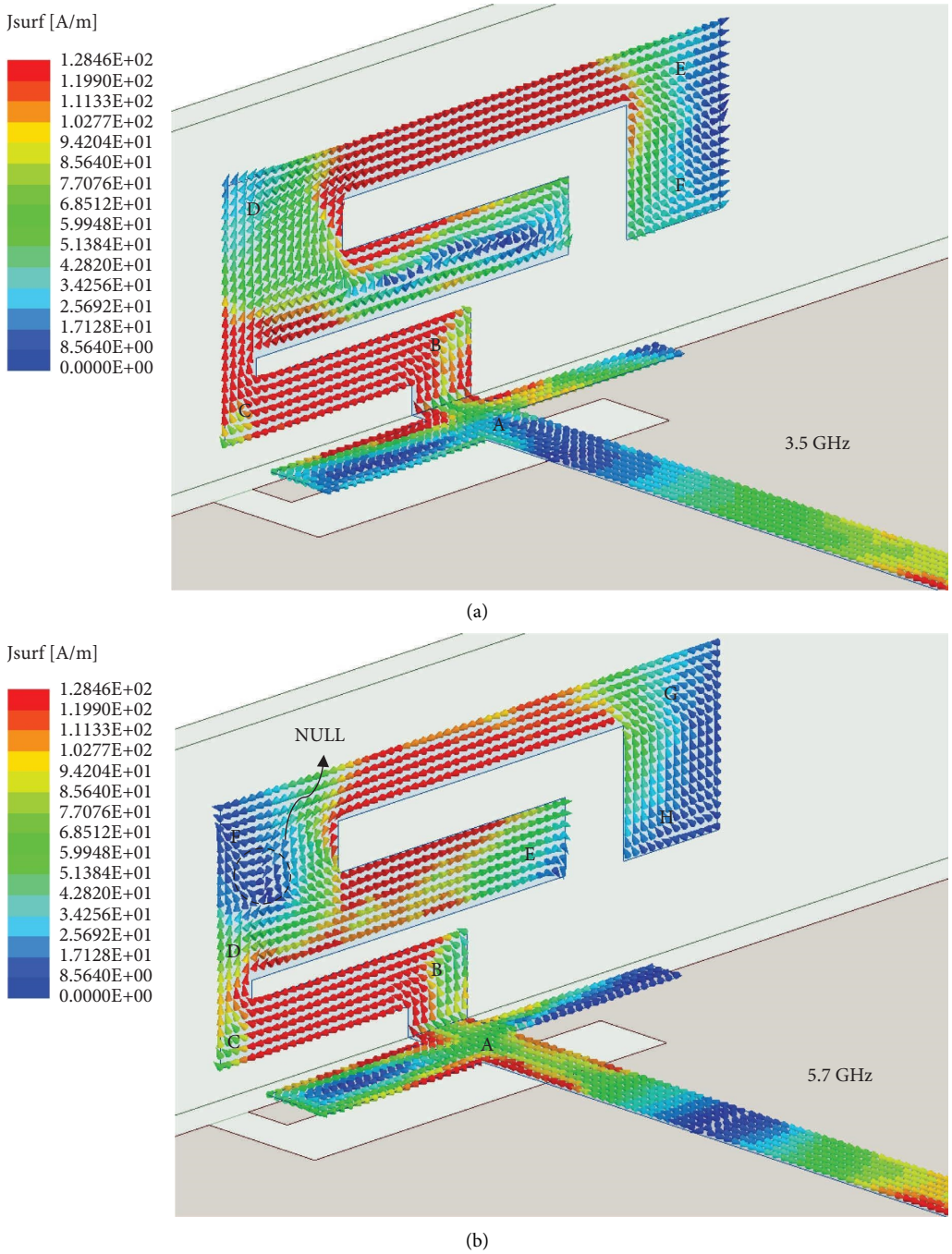

Figure 3: Current distributions of the dual-arm monopole structure at (a) 3.5 GHz and (b) 5.7 GHz.

shift from approximately 5.9 to 5.6 GHz. The optimum L_2 is chosen to be 5.8 mm because the bandwidth of the antenna is already wide enough to cover all the desired bands and it also shows that the proposed antenna has good frequency tunable performance.

From the studies mentioned above, we can verify that the f_1 is excited by the longer arm of the dual-arm monopole structure independently and the f_3 is excited by the longer arm and the shorter arm of the dual-arm monopole structure simultaneously. Finally, tuning L_3 will only affect the f_2 and without affecting those frequencies of the f_1 and f_3 as shown in Figure 5(e). When the L_3 increases from 8.5 to 9.5 mm, the f_2 will shift from approximately 4.6 to 4.2 GHz. The optimum L_3 is chosen to be 9 mm because there has the best reflection coefficient of these three results in all desired bands and 6-dB impedance bandwidth can

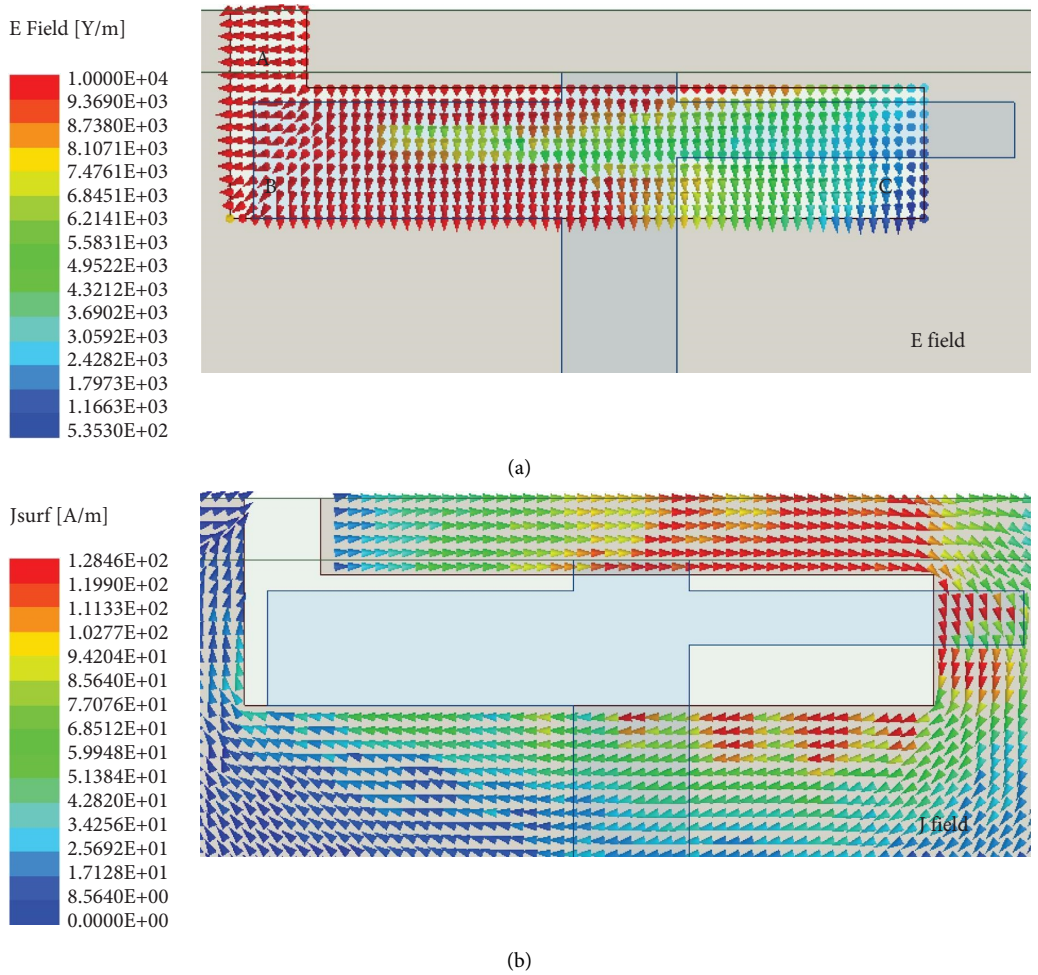

Figure 4: (a) The electric field intensity and (b) the current distribution of the open slot at 4.5 GHz.

fully cover the desired bands. Based on the result of the L_3, we can validate that the open slot is responsible for the f_2 independently.

3. Results and Discussion

The arrangement of the proposed eight-element antenna array is placed on the two side edges of the device as shown in Figure 6(a). The three-dimensional size of the device is $150 \times 75 \times 7.8\,mm^3$. In this case, Ant. 1–4 are the mirror of Ant. 5–8. Both the distances between Ant. 1 and Ant. 2, and between Ant. 3 and Ant. 4 are 29.8 mm. The distance between Ant. 2 and Ant. 3 is 30 mm. The photograph of the fabricated antenna array is shown in Figure 6(b). In this project, the simulations were performed by using Ansys HFSS.

The simulated and measured reflection coefficients and transmission coefficients of the proposed MIMO antenna array are shown in Figures 7 and 8, respectively. Good agreement between the simulated and measured results can be observed in these two figures. Figure 7 shows that the proposed MIMO antenna array has a wide 6-dB impedance bandwidth from approximately 3.2 to 6 GHz. The simulated transmission coefficients are all less than −12.6 dB across the desired bands, as shown in Figure 8. Furthermore, the measured results of the manufactured MIMO antenna array are also plotted in Figures 7 and 8. The measured results of the reflection coefficient validated that the proposed MIMO antenna array can cover the desired bands with a 6-dB impedance bandwidth of approximately 3.25 to over 6 GHz, and the transmission coefficients are all less than −10 dB without any isolation structure. The above results show that the proposed MIMO antenna array can support 5G smartphone applications in the 5G NR n77/n78/n79 and WLAN5-GHz bands.

The simulated and measured 2D radiation patterns of those Ant. 1–4 across different frequencies (3.7, 4.7, and 5.5 GHz) at the xy-plane are plotted in Figure 9. Because those Ant. 5–8 are symmetric to those Ant. 1–4, the radiation patterns of those Ant. 5–8 are not plotted, for brevity. One can see that the measured radiation patterns are highly consistent with the simulated results and each antenna has a unique radiation pattern with the orientation of the maximum gain pointing in different directions. However, the Ant. 1–4 at 4.7 and 5.5 GHz are mainly scattering toward the $-y$-direction and away from the system ground can be observed, which means that the antenna array has good MIMO performance and good isolation between the

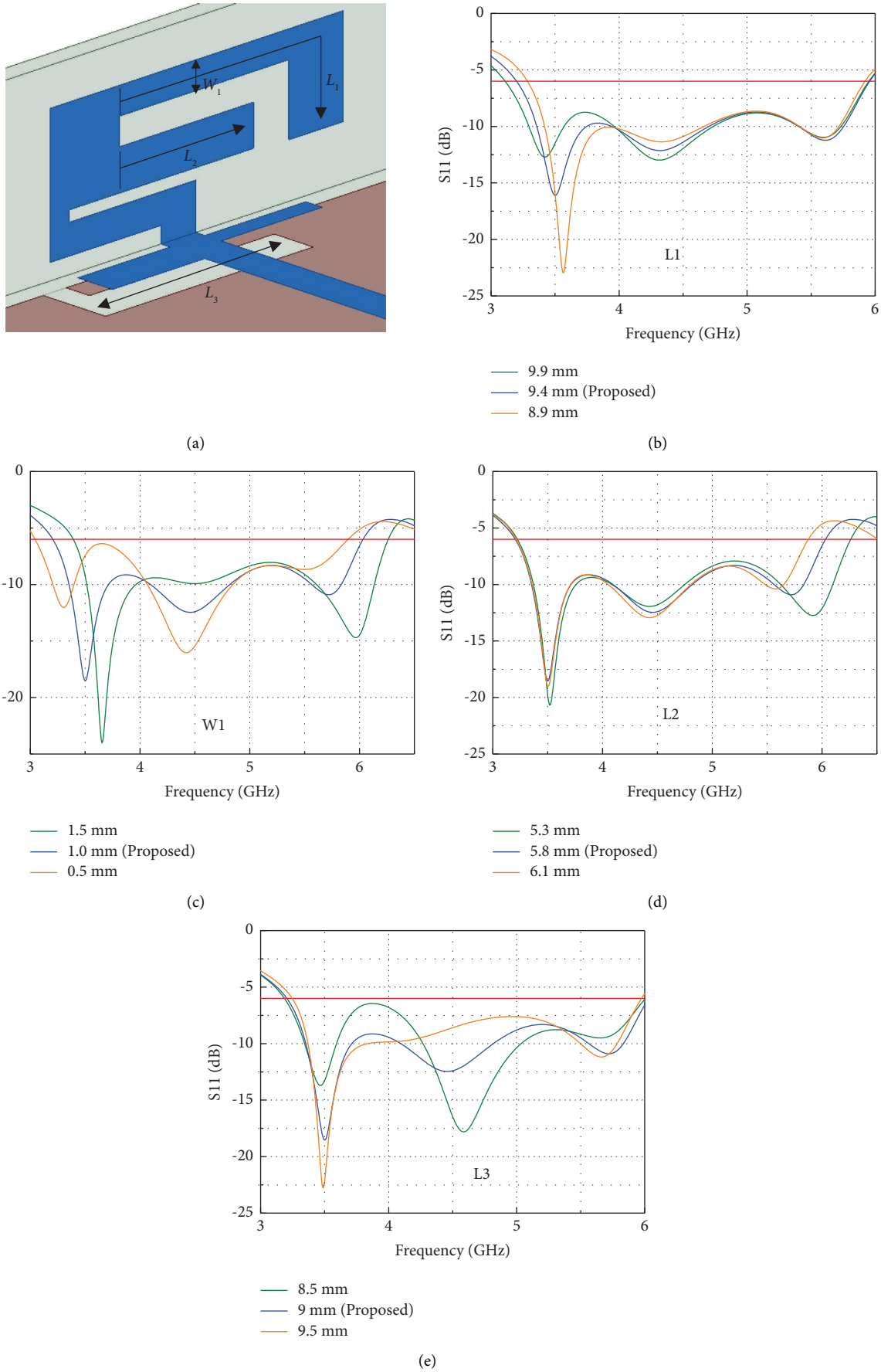

Figure 5: (a) Corresponding location of the parameters and the variety of the S parameter when tuning variables of (b) L_1, (c) W_1, (d) L_2, and (e) L_3.

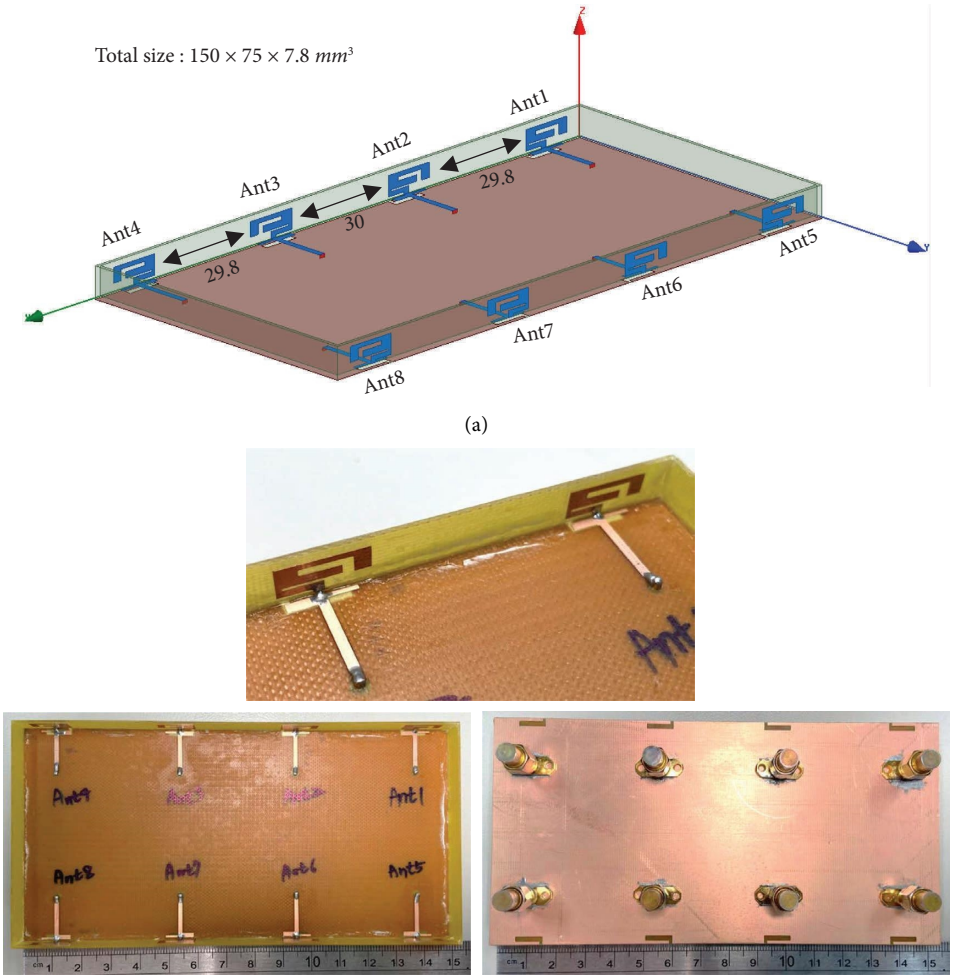

Figure 6: (a) The configuration of the MIMO antenna array and (b) the photograph of the fabricated MIMO antenna array.

opposite of the antennas at 4.7 and 5.5 GHz. Furthermore, the measured total efficiency of the proposed antenna ranges from 38% to 83% across the desired bands as shown in Figure 10.

To validate the MIMO performance of the proposed antenna array, the simulated ECCs and diversity gains are shown in Figure 11. The simulated ECCs of Ant. 1 and Ant. 2, Ant. 2 and Ant. 3, Ant. 1 and Ant. 5, and Ant. 2 and Ant. 6 are plotted in Figure 11(a). We chose these antenna pairs because they are the closest of the other antenna pairs and because of the symmetrical structure, the other antenna pairs are not included for brevity. The results of simulated ECCs show that most of those antenna pairs have ECC values less than 0.1 except the antenna pair of Ant. 1 and Ant. 5, but overall the ECCs of the proposed MIMO antenna array can still achieve less than 0.31 across the desired bands. The diversity gains [17, 18] of the proposed antenna array are shown in Figure 11(b) and for brevity, only a relatively close antenna pair has been plotted. According to industry standards, the DG values should be kept around 10 dB. One can see that all the values in the required bands are lies around the 10 dB line, except the result of Ant.1 and Ant. 5 at around 3.4 GHz is slightly deviating from the 10 dB line due to the isolation a little bit lower than the others and relatively high ECC value.

To validate the performance of the proposed antenna array, Table 1 shows the comparison of the performance between the antennas in the previously published literature and the proposed one. Here, the proposed antenna shows a very wide operating bandwidth from 3.3 to 6 GHz that can cover the 5G NR n77/78/79 and WLAN-5GHz bands. Moreover, the isolation and efficiency are also comparable to the references. The isolation of the proposed antenna array can reach 12.6 dB without any decoupling element and the efficiency can reach up to 83%. Even though the proposed antenna may have shown a slightly higher ECC value than the other references, but it just happens in the antenna pair of Ant. 1 and Ant. 5 in the frequency range of 3.3 to 3.5 GHz. In conclusion, the proposed antenna array has superior bandwidth performance compared to the other references.

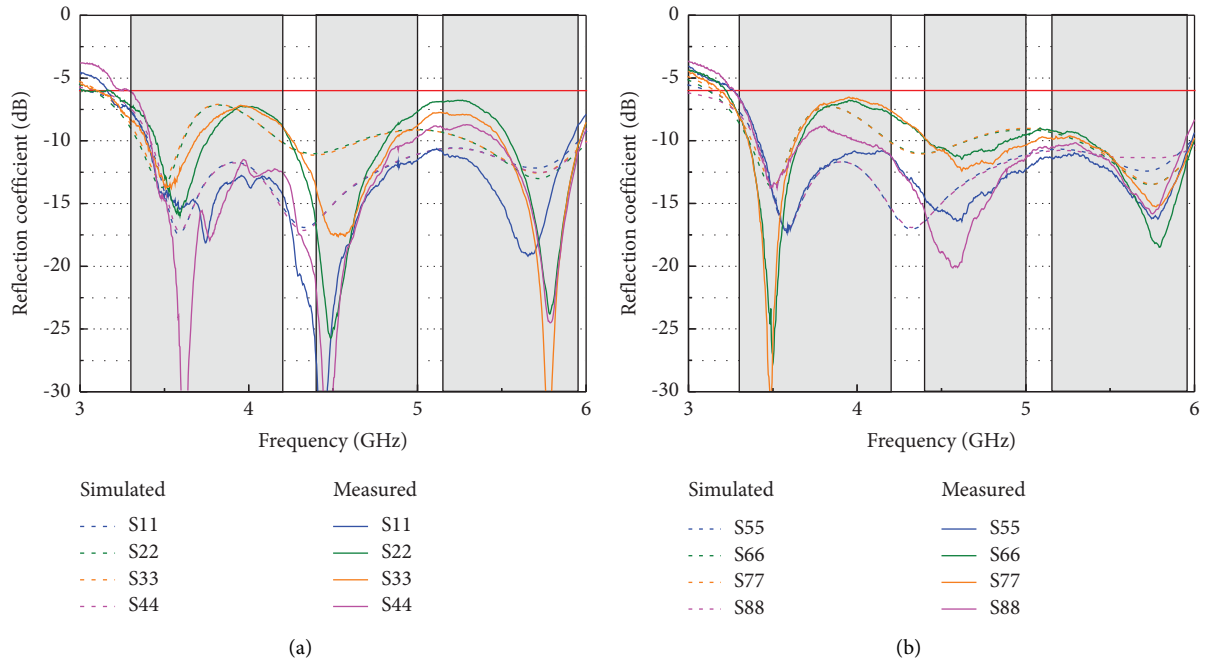

Figure 7: Simulated and measured reflection coefficients of the (a) antenna 1 to antenna 4 and (b) antenna 5 to antenna 8.

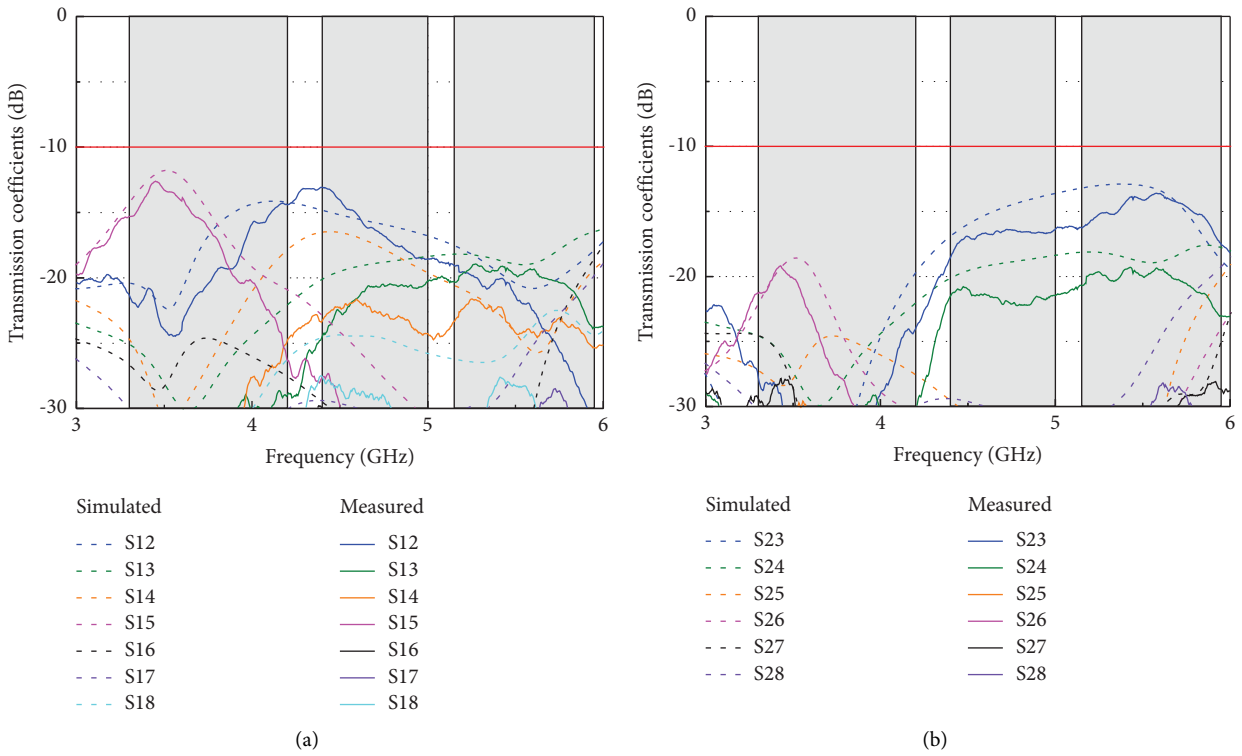

Figure 8: Simulated and measured transmission coefficients (a) between antenna 1 and the other antennas and (b) between antenna 2 and the other antennas.

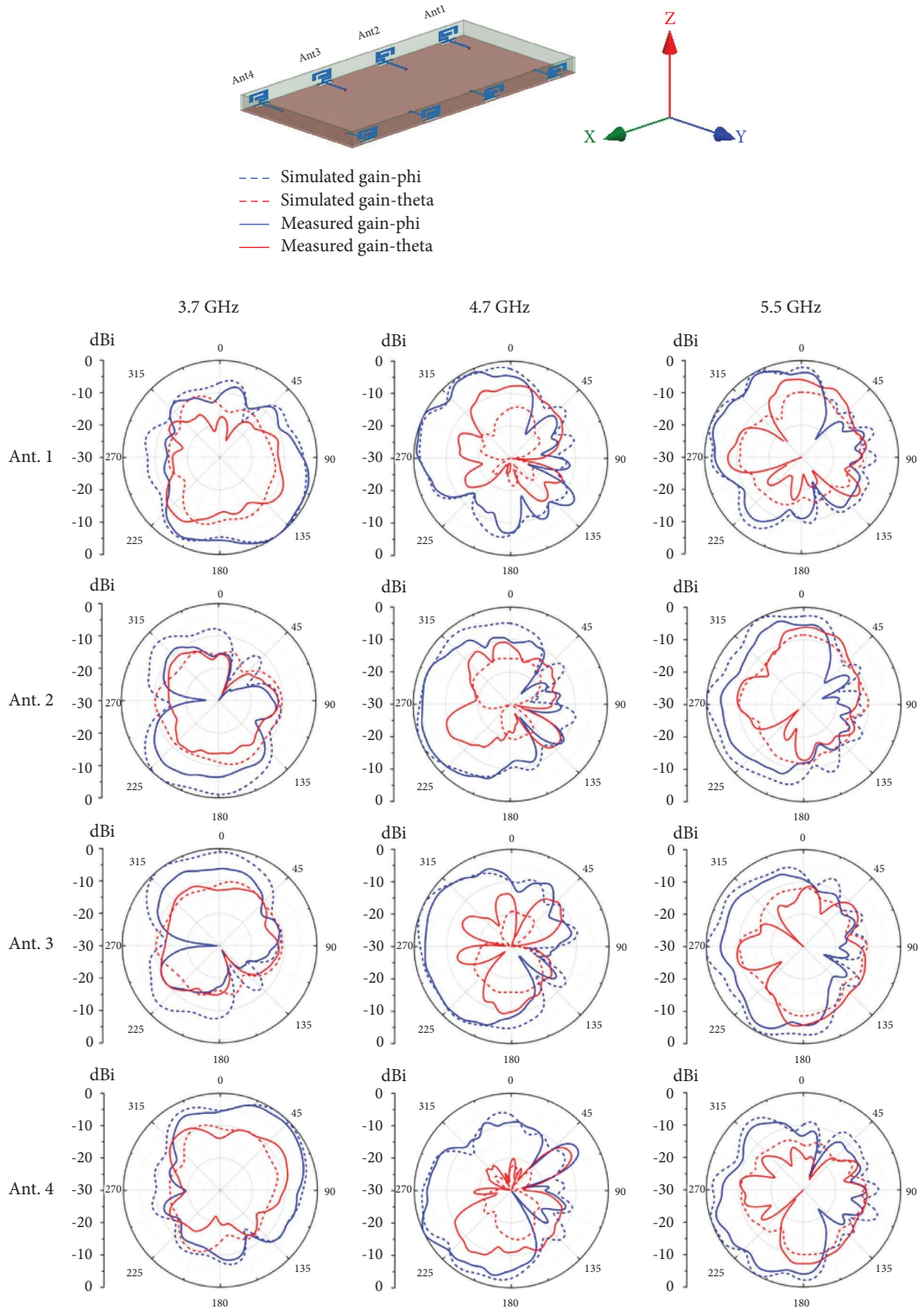

Figure 9: Simulated and measured 2D radiation patterns of Ant. 1–4 at the xy-plane in 3.7, 4.7, and 5.5 GHz.

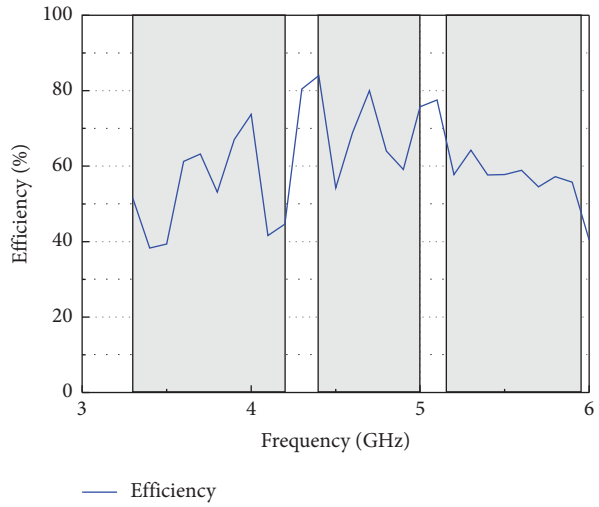

Figure 10: Measured antenna total efficiency.

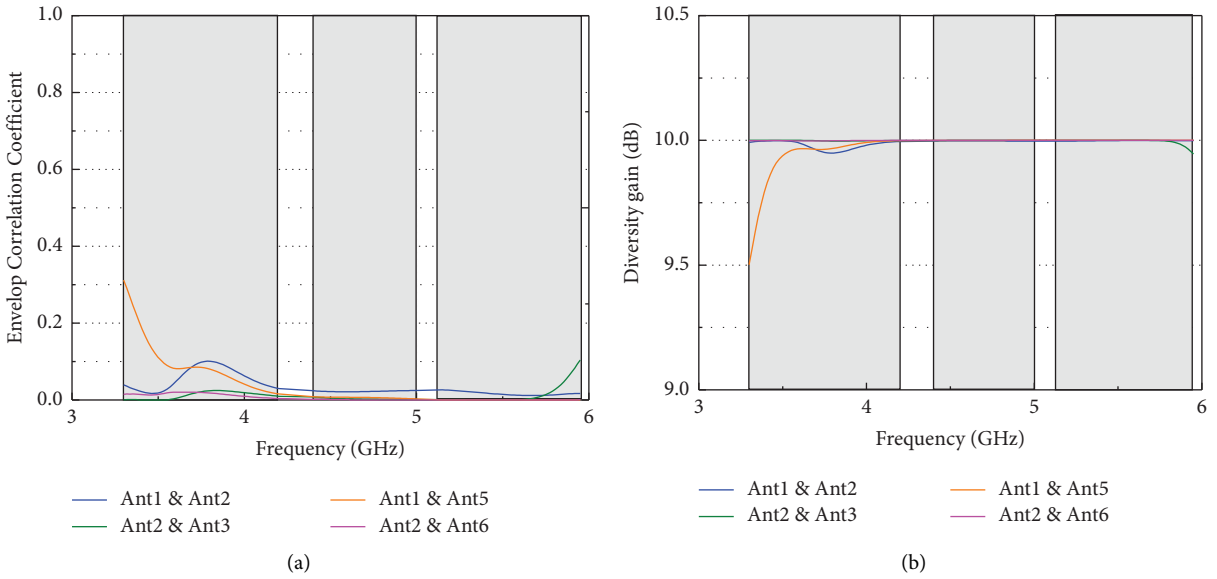

Figure 11: (a) Simulated ECCs and (b) diversity gains.

Table 1: Comparison with previously published literature.

Ref.	Bandwidth (6-dB/GHz)	Decoupling element	Efficiency (%)	Isolation (dB)	MIMO order	ECC
[1]	3.3–3.8, 4.8–5.0, 5.15–5.925	No	43–73	>10.5	8	<0.12
[2]	3.4–3.6, 5.725–5.825 (10-dB)	No	41–59	>10	12	<0.2
[3]	3.4–3.6 (10-dB)	No	40–52	>10	8	<0.15
[5]	3.3–5.8 (10-dB)	No	55–87	>15	4	<0.03
[6]	3.3–5.0	No	46–76	>14.5	8	<0.1
[7]	3.3–7.1	No	47–70	>11	8	<0.09
[8]	3.25–5.93 (10-dB)	No	41–69	>10	8	<0.1
[9]	3.3–3.6, 4.8–5.0	Yes	45–78	>12	10	<0.15
[10]	3.3–3.6	Yes	45–60	>15	8	<0.15
[11]	3.4–3.6, 4.8–5.1	Yes	41–72	>11.5	8	<0.08
[12]	3.4–3.6	No	60–68	>19.1	8	<0.0125
[13]	3.4–3.6	No	38–64	>12.7	4	<0.13
[14]	3.38–3.82, 4.8–5.6	Yes	40–85	>15.5	8	<0.07
[15]	3.3–6.0	Yes	40–90	>18	8	<0.05
[16]	3.3–7.5	No	40–78	>10	4	<0.05
Pro.	**3.3–6.0**	**No**	**38–83**	**>12.6**	**8**	**<0.31 (Ant. 1 and 5) <0.1 (others)**

4. Conclusions

A wideband and simple structure MIMO antenna array for 5G smartphone application is presented in this paper. The proposed MIMO antenna array fully covers the entire 5G NR n77/n78/n79 and WLAN-5GHz bands with a 6-dB impedance bandwidth range from 3.2 to 6 GHz, and the isolations are all more than 10 dB without any isolation structure or techniques. To validate the design concept, the proposed MIMO antenna array was fabricated and measured. Good agreement of the reflection coefficients, the isolations, and the 2D radiation patterns are obtained between the simulated and measured results. Furthermore, the total efficiency of the antenna ranges from 38 to 83%. The simulated ECCs are all less than 0.31. Therefore, the above experimental results validate that the proposed MIMO antenna array can support 5G smartphone applications.

Data Availability

The data used to support the findings of this study are included within the article.

Conflicts of Interest

The authors declare that there are no conflicts of interest regarding the publication of this paper.

Acknowledgments

The authors would like to thank the Ministry of Science and Technology (Taiwan) and National Pingtung University for partially sponsoring this work (MOST 106-2633-E-153 -001-).

References

[1] H. Wang, R. Zhang, Y. Luo, and G. Yang, "Compact eight-element antenna array for triple-band MIMO operation in 5G mobile terminals," *IEEE Access*, vol. 8, pp. 19433–19449, 2020.

[2] Z. Tian, R. Chen, and C. Li, "Dual-band inverted F-shaped antenna array for sub-6 GHz smartphones," in *Proceedings of the 2019 IEEE 89th Vehicular Technology Conference (VTC2019-Spring)*, pp. 1–5, Kuala Lumpur, Malaysia, April 2019.

[3] K. L. Wong, C. Y. Tsai, and J. Y. Lu, "Two asymmetrically mirrored gap-coupled loop antennas as a compact building block for eight-antenna MIMO array in the future smartphone," *IEEE Transactions on Antennas and Propagation*, vol. 65, no. 4, pp. 1765–1778, 2017.

[4] H. Wang and G. Yang, "Wideband Antenna system for multi-band 8×8 MIMO operation in the 5G mobile terminals," in *Proceedings of the 2019 International Symposium on Antennas and Propagation (ISAP)*, pp. 1–3, Xi'an, China, October 2019.

[5] Z. Zheng, J. D. Ntawangaheza, and L. Sun, "Wideband MIMO antenna system for sub-6 GHz cell phone," in *Proceedings of the 2021 International Conference on Electronics, Circuits and Information Engineering (ECIE)*, pp. 1–5, Zhengzhou, China, January 2021.

[6] A. Zhao and Z. Ren, "Wideband MIMO antenna systems based on coupled-loop antenna for 5G N77/N78/N79 applications in mobile terminals," *IEEE Access*, vol. 7, pp. 93761–93771, 2019.

[7] Q. Cai, Y. Li, X. Zhang, and W. Shen, "Wideband MIMO antenna array covering 3.3–7.1 GHz for 5G metal-rimmed smartphone applications," *IEEE Access*, vol. 7, pp. 142070–142084, 2019.

[8] C.-Y.-D. Sim, H.-Y. Liu, and C.-J. Huang, "Wideband MIMO antenna array design for future mobile devices operating in the 5G NR frequency bands n77/n78/n79 and LTE band 46," *IEEE Antennas and Wireless Propagation Letters*, vol. 19, no. 1, pp. 74–78, 2020.

[9] W. Hu, X. Liu, S. Gao et al., "Dual-band ten-element MIMO array based on dual-mode IFAs for 5G terminal applications," *IEEE Access*, vol. 7, pp. 178476–178485, 2019.

[10] W. Jiang, B. Liu, Y. Cui, and W. Hu, "High-isolation eight-element MIMO array for 5G smartphone applications," *IEEE Access*, vol. 7, pp. 34104–34112, 2019.

[11] J. Guo, L. Cui, C. Li, and B. Sun, "Side-edge frame printed eight-port dual-band antenna array for 5G smartphone applications," *IEEE Transactions on Antennas and Propagation*, vol. 66, no. 12, pp. 7412–7417, 2018.

[12] A. Zhao and Z. Ren, "Size reduction of self-isolated MIMO antenna system for 5G mobile phone applications," *IEEE Antennas and Wireless Propagation Letters*, vol. 18, no. 1, pp. 152–156, 2019.

[13] L. Chang, Y. Yu, K. Wei, and H. Wang, "Polarization-orthogonal Co-frequency dual antenna pair suitable for 5G MIMO smartphone with metallic bezels," *IEEE Transactions on Antennas and Propagation*, vol. 67, no. 8, pp. 5212–5220, 2019.

[14] W. Hu, L. Qian, S. Gao et al., "Dual-band eight-element MIMO array using multi-slot decoupling technique for 5G terminals," *IEEE Access*, vol. 7, pp. 153910–153920, 2019.

[15] X.-T. Yuan, W. He, K.-D. Hong, C.-Z. Han, Z. Chen, and T. Yuan, "Ultra-wideband MIMO antenna system with high element-isolation for 5G smartphone application," *IEEE Access*, vol. 8, pp. 56281–56289, 2020.

[16] X.-T. Yuan, Z. Chen, T. Gu, and T. Yuan, "A wideband PIFA-pair-based MIMO antenna for 5G smartphones," *IEEE Antennas and Wireless Propagation Letters*, vol. 20, no. 3, pp. 371–375, 2021.

[17] J. Kulkarni, A. G. Alharbi, A. Desai, C.-Y.-D. Sim, and A. Poddar, "Design and analysis of wideband flexible self-isolating MIMO antennas for sub-6 GHz 5G and WLAN smartphone terminals," *Electronics*, vol. 10, no. 23, p. 3031, 2021.

[18] J. Kulkarni, S. Dhabre, S. Kulkarni, C.-Y. D. Sim, R. K. Gangwar, and K. Cengiz, "Six-Port symmetrical CPW-fed MIMO antenna for futuristic smartphone devices," in *Proceedings of the 2021 6th International Conference for Convergence in Technology (I2CT)*, pp. 1–5, Pune, India, April 2021.

Hindawi
International Journal of Antennas and Propagation
Volume 2022, Article ID 6987814, 9 pages
https://doi.org/10.1155/2022/6987814

Research Article

A Fast and Efficient Beamforming Algorithm Imitating Plant Growth Gene for Phased Array Antenna

Jinling Zhang,[1] Chen Han,[1] Zhanqi Zheng,[2] Xiongzhi Zhu,[3] and Xiaohui Li[1]

[1]*School of Electronic Engineering, Beijing University of Posts and Telecommunications, Beijing 100876, China*
[2]*CICT Mobile Equipment Co, Beijing 100029, China*
[3]*National Center for International Joint Research of Electronic Materials and Systems, School of Electrical and Information Engineering, Zhengzhou University, Zhengzhou 450001, China*

Correspondence should be addressed to Xiongzhi Zhu; zhuxiongzhi@zzu.edu.cn

Received 1 September 2022; Accepted 1 October 2022; Published 4 November 2022

Academic Editor: Chow-Yen-Desmond Sim

In this paper, a new beamforming algorithm for phased array antennas is proposed, the plant growth gene algorithm. The algorithm consists of three steps. Firstly, according to the excitation relation of the array unit before and after the local fine-tuning of the antenna radiation pattern, the model for solving the array unit excitation difference is established. Secondly, the Taylor series expansion is used to solve the model, and the growth model is established based on this, and the beam tuning network is designed to realize the growth model. Finally, based on the growth gene obtained by the neural network algorithm, the growth model is called multiple times for high-precision beamforming. This algorithm converts the complex optimization process of array antenna excitation by the classical optimization algorithm into a simple process of fine-tuning the gain at any angle on the beam to make it grow and approach the target pattern. The growth gene is used to weigh the target angle and gain to achieve beamforming, which greatly reduces the complexity of the algorithm and improves its accuracy of the algorithm. Taking a 1×16 linear array as an example, a cosecant square beam pattern with a coverage range of -31° to 31° and a maximum gain direction of 17° is designed using the algorithm proposed in this paper. The experimental results show that the proposed algorithm can easily fine-tune the gain of any angle to achieve precise beamforming. Importantly, the growth genes trained by the algorithm are universal to the phased array antenna with the same topology.

1. Introduction

Beamforming is an important technology for array antennas to realize long-distance high-quality communication and high-resolution target detection. A lot of research work on array antenna beamforming has been carried out at home and abroad [1–8]. Among them, based on the target beam pattern, there are many research studies on using algorithms to optimize the excitation amplitude and phase of each array unit or optimizing the arrangement of array units to realize beamforming, such as genetic algorithm [5], model order reduction [6], weed algorithm [7], and particle swarm optimization algorithm [8]. The method of using the algorithm for beamforming is to make the gains of all angles of the original beam approach the target pattern, so as to minimize the error between the original and target beam pattern. In these algorithms, the errors of all angles are counted, and the overall errors are aimed at minimizing. However, it is difficult to optimize the errors of a single-angle to the minimum, which leads to the failure of the antenna radiation pattern to accurately fit with the target pattern at a single angle, and it is difficult to achieve further improvement. In addition, for the antenna whose topology is determined, or without changing the antenna structure, when the target pattern needs to be changed or improved according to engineering applications or other reasons, even if only one angle gain needs to be changed, the optimization algorithm needs to be rerun to calculate the excitation corresponding to the new beam pattern. Therefore, the beamforming by the current algorithm has low efficiency and accuracy, high cost, poor generality, and no correction mechanism for local errors, so it is impossible to fine-tune the results of the beamforming.

With the development of deep learning technology, the neural network method is used to model the nonlinear relationship between the antenna radiation pattern and the excitation of the array units, and the coupling effect between the array units is considered in the beamforming process [9–11]. In [12], a convolutional neural network is used to model the beamforming problem of a phased array. The processed two-dimensional pattern image is used as input of the model and the output of the model is the phase of each array unit. In [13], the antenna is placed in a space with obstacles, the neural network is used to deal with the beamforming problem, and the interaction between array units and the existence of obstacles are considered, which is more in line with the practical application scenarios. Besides excitation, the position of each array unit also affects the beam pattern. In [14], the coupling effects of different array unit positions in beamforming are analyzed through the neural network, and the array unit position distribution and excitation are simultaneously optimized by combining optimization algorithms. The transfer learning method is used in [15] to reduce the amount of data required for training and obtains better results than traditional DNN methods.

In this paper, we propose a beamforming algorithm that imitates the plant growth gene (Growth Gene Algorithm (GGA)) and train a set of growth gene parameters by a neural network. Using the growth gene to weigh any target angle and target gain can easily control the gain of any angle on the known antenna radiation pattern and gradually increase the gain of that angle by a certain step size, just as a plant grows a new branch in a local area. The specific process is as follows: firstly, by analyzing the parameter information involved in the gain change of a certain angle of the phased array antenna, a growth model for beam fine-tuning of the single-angle gain of the antenna radiation pattern is proposed. Secondly, the Beam Tuning Network (BTNet) is designed based on the neural network and growth model structure. Finally, the data obtained by an improved genetic algorithm [16] and the growth gene of the phased array antenna are obtained. Accurate beamforming is realized based on the growth gene parameters. Experimental verification shows that we can fine-tune the beam gain at any angle based on the growth gene parameters and can be applied to the phased array antenna of any antenna unit structure. It has universality, greatly reduces the complexity of pattern configuration, and improves the efficiency and precision of array antenna synthesis.

2. The Theory of Gain Fine-Tuning

A method of expressing beamforming with excitation difference is proposed, which converts the array antenna beamforming into high-precision beamforming for any target pattern by gradually fine-tuning the gain at any angle in the antenna radiation pattern. Each of these fine-tuning of the gain at an angle is achieved by adding an excitation difference ∂W corresponding to the pattern difference to the known excitation W^{ori}.

Assuming that the excitation corresponding to the original pattern of the n-unit array antenna is $W^{ori} = \left[w^{ori}(1), w^{ori}(2), \ldots, w^{ori}(n), \ldots, w^{ori}(N) \right]^T$, and the excitation corresponding to the pattern after fine-tuning is $W = [w(1), w(2), \ldots, w(n), \ldots, w(N)]^T$, then the relationship between the corresponding excitation before and after pattern fine-tuning can be expressed as follows:

$$\begin{bmatrix} w(1) \\ w(2) \\ \cdots \\ w(n) \\ \cdots \\ w(N) \end{bmatrix} = \begin{bmatrix} w^{ori}(1) \\ w^{ori}(2) \\ \cdots \\ w^{ori}(n) \\ \cdots \\ w^{ori}(N) \end{bmatrix} + \begin{bmatrix} \partial w(1) \\ \partial w(2) \\ \cdots \\ \partial w(n) \\ \cdots \\ \partial w(N) \end{bmatrix}, \tag{1}$$

where $\partial w(n)$ represents the difference of excitation before and after beamforming of the nth array unit. The above expression is only related to the excitation of the antenna unit and does not involve the antenna array unit. Therefore, for an array antenna with any antenna unit structure, the relationship between the excitations of the array units before and after beamforming can be expressed by (1).

For any beamforming problem, there are corresponding W and $\partial W = [\partial w(1), \partial w(2), \ldots, \partial w(n), \ldots, \partial w(N)]^T$ on the basis of any original excitation W^{ori}. The key of traditional array antenna beamforming is to search for appropriate excitation W. The growth gene algorithm proposed in this paper is to solve ∂W instead of searching W and obtains the excitation corresponding to the target pattern indirectly by using the general model among W, W^{ori}, and ∂W.

3. Materials and Methods

3.1. Growth Gene Algorithm (GGA). As shown in Figure 1, the excitation difference $\partial w(n)$ corresponding to the gain change at a certain angle of the phased array antenna radiation pattern is only related to the following three parameters: the angle to be adjusted, θ (in radians), the original gain of the pattern at the angle θ, $G^{ori}(\theta)$ (in dBi), and the expected gain change, s (in dB). According to the three parameters $\theta, G^{ori}(\theta)$, and s to solve ∂W, the mathematical solution model of ∂W is assumed as follows:

$$\partial w(n) = f(s) g\left(G^{ori}(\theta)\right) h(\theta, n), \tag{2}$$

where $\partial w(n)$ represents the excitation difference of the nth array element before and after the pattern fine-tuning, $f(s)$ and $g(G^{ori}(\theta))$ are unknown functions about s and $G^{ori}(\theta)$ respectively, and $h(\theta, n)$ is the array factor of the target angle of the nth array element

$$h(\theta, n) = e^{-j2\pi d(n-1)\cos(\theta)}. \tag{3}$$

When beamforming the phased array antenna, since the fine-tuned pattern can be arbitrary compared to the original pattern, the gain $G^{ori}(\theta) + s$ of the fine-tuned pattern at angle θ is also arbitrary compared to the gain $G^{ori}(\theta)$ of the original pattern. That is, the expected gain change s at the angle θ is independent of the original gain $G^{ori}(\theta)$. Therefore, in (2), two unary functions $f(s), g(G^{ori}(\theta))$ instead of

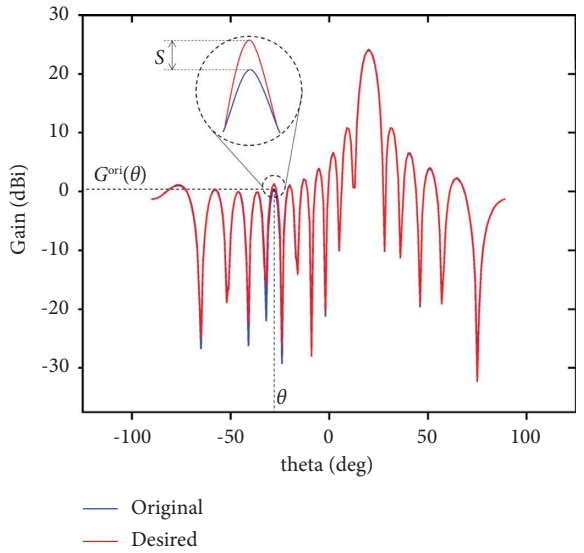

FIGURE 1: When there is only a local difference between the target pattern and the original pattern at the angle and the expected gain change is small, it is difficult to use the optimization algorithm for accurate beamforming.

binary functions $f(s, G^{ori}(\theta))$ are used to represent ∂W model.

Although $f(s)$ and $g(G^{ori}(\theta))$ are unknown in the ∂W model, according to the definition of Taylor series, $f(s)$ can be expressed as follows:

$$f(s) = \sum_{m=0}^{\infty} \frac{f^{(m)}(0)}{m!} s^m = f(0) + f'(0)s + \frac{f''(0)}{2!}s^2 + \ldots + \frac{f^{(m)}(0)}{m!}s^m + \ldots. \tag{4}$$

Let $a_0 = f(0), a_1 = f'(0), a_2 = (f''(0)/2!), \ldots, a_m = (f^{(m)}(0)/m!), \ldots$, then $f(s)$ can be expressed as follows:

$$f(s) = a_0(n) + a_1(n)s^1 + a_2(n)s^2 + \ldots + a_m(n)s^m + \ldots, \tag{5}$$

where n represents the nth array element. Similarly, $g(G^{ori}(\theta))$ can be expressed as follows:

$$g\left(G^{ori}(\theta)\right) = b_0(n) + b_1(n)G^{ori}(\theta) + b_2(n)G^{ori}(\theta)^2 + \ldots + b_m(n)G^{ori}(\theta)^m + \ldots. \tag{6}$$

The higher the order of the Taylor series, the higher the approximation of the function expression. The experimental simulation results show that the fifth-order Taylor series can already meet the accuracy requirements of beamforming. So in this paper, the functions $f(s)$ and $g(G^{ori}(\theta))$ are expanded into the fifth-order Taylor series. The ∂W model can be expressed as follows:

$$\begin{aligned}\partial w(n) = &\left(a_0(n) + a_1(n)s^1 + a_2(n)s^2 + a_3(n)s^3 + a_4(n)s^4 + a_5(n)s^5\right) \times \left(b_0(n) + b_1(n)G^{ori}(\theta)\right. \\ &\left. + b_2(n)G^{ori}(\theta)^2 + b_3(n)G^{ori}(\theta)^3 + b_4(n)G^{ori}(\theta)^4 + b_5(n)G^{ori}(\theta)^5\right) \times e^{-j2\pi d(n-1)\cos(\theta)}.\end{aligned} \tag{7}$$

Since the even and odd powers of negative numbers are opposite numbers, the same ∂W model cannot accurately express the two cases of expected gain change $s > 0$ and $s < 0$. However, the expansion of Taylor series shows that for both cases, the ∂W model has different weights but has similar forms. When $s > 0$, ∂W model can be expressed as follows:

$$\begin{aligned}\partial w(n) = &\left(a_0^+(n) + a_1^+(n)s^1 + a_2^+(n)s^2 + a_3^+(n)s^3 + a_4^+(n)s^4 + a_5^+(n)s^5\right)\\ &\times \left(b_0^+(n) + b_1^+(n)G^{ori}(\theta) + b_2^+(n)G^{ori}(\theta)^2 + b_3^+(n)G^{ori}(\theta)^3\right.\\ &\left.+ b_4^+(n)G^{ori}(\theta)^4 + b_5^+(n)G^{ori}(\theta)^5\right) \times e^{-j2\pi d(n-1)\cos(\theta)}.\end{aligned} \tag{8}$$

When $s < 0$, ∂W model can be expressed as follows:

$$\begin{aligned}\partial w(n) = &\left(a_0^-(n) + a_1^-(n)s^1 + a_2^-(n)s^2 + a_3^-(n)s^3 + a_4^-(n)s^4 + a_5^-(n)s^5\right)\\ &\times \left(b_0^-(n) + b_1^-(n)G^{ori}(\theta) + b_2^-(n)G^{ori}(\theta)^2 + b_3^-(n)G^{ori}(\theta)^3\right.\\ &\left.+ b_4^-(n)G^{ori}(\theta)^4 + b_5^-(n)G^{ori}(\theta)^5\right) \times e^{-j2\pi d(n-1)\cos(\theta)}.\end{aligned} \tag{9}$$

It can be seen from (8) and (9) that for the problem of fine-tuning the gain of the single-angle in beamforming, as long as the weights $(a_0^+(n), \ldots, a_5^+(n), b_0^+(n), \ldots, b_5^+(n); a_0^-(n), \ldots, a_5^-(n), b_0^-(n), \ldots, b_5^-(n))$ in the ∂W model are appropriate, the excitation corresponding to each array element after the gain fine-tuning can be calculated according to s and $G^{ori}(\theta)$. Since the positive fine-tuning of the gain at an angle $(s > 0)$ is similar to the plant gradually growing a new branch in a certain part, the weights $(a_0^+(n), \ldots, a_5^+(n), b_0^+(n), \ldots, b_5^+(n))$ that plays a key role in the process of positive fine-tuning of gain are called positive growth gene, and the weights $(a_0^-(n), \ldots, a_5^-(n), b_0^-(n), \ldots, b_5^-(n))$ that play a role in the process of negative fine-tuning $(s < 0)$ are called negative growth gene, and the gain fine-tuning model ∂W is named "Growth Model."

In this paper, the method of using the growth model to adjust the gain of any angle of the radiation pattern to realize the precise beamforming of the phased array antenna is named the Growth Gene Algorithm (GGA). The beamforming of GGA only involves simple matrix multiplication and addition operation, so the complexity is much lower than other beamforming algorithms. The solution of GGA is $\partial w(n)$ of a single array element after beamforming. Each array element corresponds to a growth model and two sets of gene parameters. Taking 1×16 linear array antenna as an example, a total of $2 \times 12 \times 16 = 384$ gene parameters need to be determined. Since the growth model does not involve the radiation pattern of the array element, for the 1×16 linear array antenna with the same topology, these 384 gene parameters are applicable to the antenna element of any structure.

In the next section, Beam Tuning Network (BTNet) is designed based on a growth gene algorithm and neural network, and the growth genes of 1×16 linear array antenna are trained to verify the effectiveness of the algorithm proposed in this paper for fine-tuning gain at any angle and high-precision beamforming.

3.2. Beam Tuning Network (BTNet). The neural network model designed to train the growth model of each array element is shown in Figure 2.

In BTNet, the weight training by the convolutional layer of sub network 1 corresponds to the gene parameter $a_1(n), a_2(n), a_3(n), a_4(n), a_5(n)$ related to $f(s)$, and the trained bias corresponds to the gene parameter $a_0(n)$. The activation function used by the convolutional layer is "identity mapping," that is, $y = \sigma(x) = x$. The architecture of subnetwork 2 is similar to that of subnetwork 1, in that the weight and bias trained by the convolutional layer correspond to the gene parameters related to $g(G^{ori}(\theta))$, and the activation function is also "identity mapping." In order to make the output of the neural network consistent with the growth model, sub network 3 uses the "multiplicator layer" designed for the structure of the growth model. Its input is $f(s)$ and $g(G^{ori}(\theta))$ learned by the network, and the output is $f(s) \times g(G^{ori}(\theta))$. According to the form of array factor in the growth model, the activation function in the sub network 3 is designed as $y = \sigma(x) = h(\theta, n)x$, so that the output of the activation function is the growth model $\partial w(n)$ of the nth array element.

To sum up, the process of beamforming by the GGA is shown in Figure 3. The gene parameters of the growth model corresponding to each array element are trained through BTNet, and the growth model obtained by training is used to calculate the excitation of each array element corresponding to the target pattern to complete the beamforming. The algorithm can fine-tune the gain at any angle on any radiation pattern, achieve high-precision beamforming, decouple the main lobe and side lobe, and have the characteristics of high computing efficiency and real-time data feedback.

4. Algorithms and Model Validation

4.1. Training Strategy. Taking the 1×16 linear array antenna as an example to verify the algorithm, BTNet is used to train the gene parameters of the growth model of each array element, and the Adam optimizer is used in the training [17]. In the experiment, the data pair (θ, s) composed of random angles and gain change values is used as the optimization target pattern, and the improved genetic algorithm [16] is used to generate 20,000 sets of data in the format of $(\theta, G(\theta), s, \partial W)$, in which the ratio of $s > 0$ to $s < 0$ is 1 : 1.

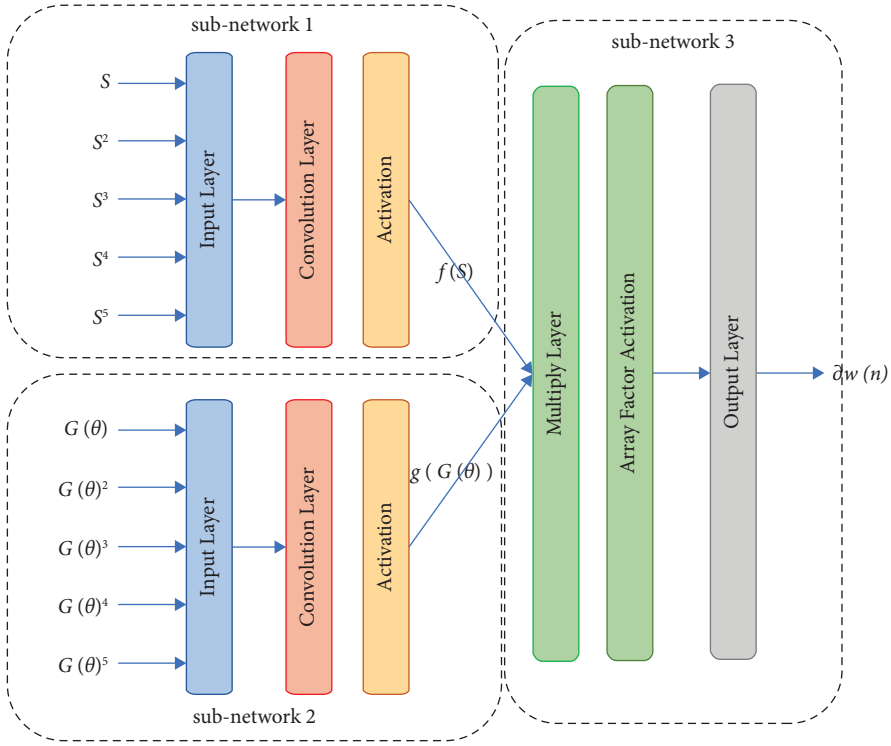

Figure 2: BTNet is a general model structure designed based on the neural network combined with the antenna gain fine-tuning problem. Different from the traditional neural network, it has two input layers and its network structure can be divided into three subnetworks.

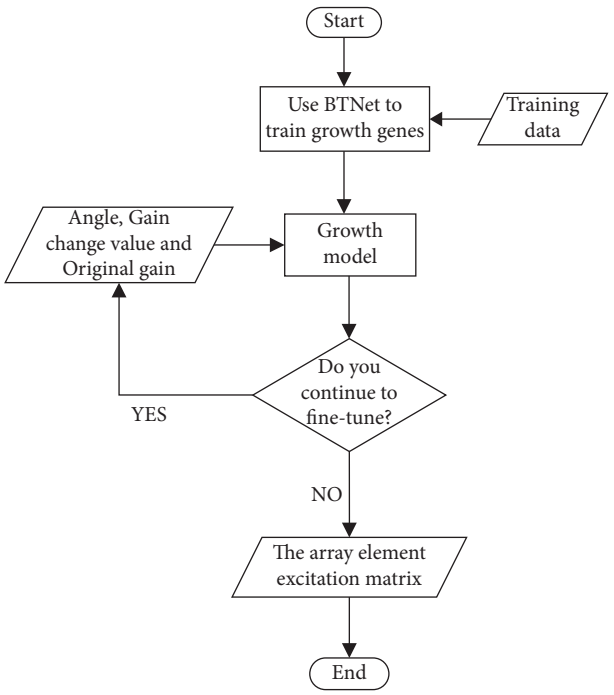

Figure 3: Flow chart of beamforming using growth model; in the process of beamforming, the gene parameters of the growth model corresponding to each array element were first trained by BTNet. Then, use the trained growth model to calculate the excitation of each array element corresponding to the target pattern and complete the beamforming.

BTNet is trained with 8000 sets of data, and 2000 sets of data are used for validation. Set the number of training times (epochs) to 400 and batch size to 100, and use the CPU version of TensorFlow 1.8.0 for simulation. In order to improve the efficiency of training, the transfer learning [18] strategy is adopted in training. Except that the initial weights are randomly generated in the first training, the weights trained in the previous training are used as the initial weights in the rest of the training. For the 1×16 linear array antenna, in order to obtain 2 sets of gene parameters of the growth model of each array element, BTNet was used for 32 times of training. Under the condition of Intel(R) Core(TM) I5-7300HQ CPU @ 2.50 GHz processor and 8 Gb memory, the first training takes about 7 minutes, and the rest training takes about 1 minute and 27 seconds on average due to the strategy of transfer learning.

4.2. Experimental Results of Growth Genes. Under the condition of 20000 sets of data, BTNet was used to train the growth model of 1×16 linear arrays, and the obtained 192 positive growth gene parameters and negative growth gene parameters are shown in Tables 1 and 2, respectively.

The gene parameters in this table are applicable to the 1×16 linear array antenna of any antenna element structure. By using the growth model to fine-tune the gain at any angle on the radiation pattern, the corresponding excitation of each array element can be calculated quickly.

Table 1: 1×16 linear array positive growth gene parameters.

	a0	a1	a2	a3	a4	a5	b0	b1	b2	b3	b4	b5
$n=1$	0	0.115134	0.006719	0.000341	0.000090	0.000010	1	0.007226	0.000444	0.000088	0.000014	0.000072
$n=2$	0	0.115141	0.006695	0.000299	0.000088	0.000072	1	0.007290	0.000499	0.000053	0.000070	0.000020
$n=3$	0	0.115133	0.006704	0.000300	0.000058	0.000090	1	0.007261	0.000472	0.000106	0.000081	0.000058
$n=4$	0	0.115148	0.006654	0.000339	0.000013	0.000049	1	0.007217	0.000508	0.000091	0.000050	0.000047
$n=5$	0	0.115136	0.006698	0.000254	0.000017	0.000052	1	0.007210	0.000492	0.000102	0.000072	0.000015
$n=6$	0	0.115196	0.006682	0.000347	0.000075	0.000080	1	0.007245	0.000453	0.000103	0.000008	0.000013
$n=7$	0	0.115147	0.006669	0.000333	0.000090	0.000006	1	0.007240	0.000463	0.000062	0.000066	0.000063
$n=8$	0	0.115159	0.006673	0.000252	0.000108	0.000017	1	0.007211	0.000447	0.000040	0.000049	0.000034
$n=9$	0	0.115225	0.006722	0.000255	0.000084	0.000027	1	0.007242	0.000465	0.000114	0.000042	0.000098
$n=10$	0	0.115160	0.006700	0.000317	0.000064	0.000070	1	0.007267	0.000428	0.000033	0.000100	0.000017
$n=11$	0	0.115133	0.006686	0.000338	0.000077	0.000019	1	0.007237	0.000456	0.000118	0.000016	0.000086
$n=12$	0	0.115194	0.006668	0.000269	0.000053	0.000048	1	0.007212	0.000469	0.000043	0.000038	0.000058
$n=13$	0	0.115155	0.006659	0.000312	0.000037	0.000082	1	0.007298	0.000483	0.000054	0.000058	0.000011
$n=14$	0	0.115221	0.006718	0.000332	0.000036	0.000059	1	0.007202	0.000453	0.000051	0.000016	0.000018
$n=15$	0	0.115172	0.006639	0.000310	0.000057	0.000070	1	0.007270	0.000474	0.000023	0.000007	0.000032
$n=16$	0	0.115183	0.006695	0.000291	0.000092	0.000072	1	0.007297	0.000463	0.000053	0.000011	0.000061

Table 2: 1×16 linear array negative growth gene parameters.

Gene	a0	a1	a2	a3	a4	a5	b0	b1	b2	b3	b4	b5
$n=1$	0	0.115199	−0.006574	0.000290	−0.000004	0.000078	1	0.007234	0.000471	0.000094	0.000010	0.000013
$n=2$	0	0.115185	−0.006581	0.000339	0.000070	0.000073	1	0.007205	0.000417	0.000029	0.000080	0.000094
$n=3$	0	0.115198	−0.006617	0.000322	0.000001	0.000012	1	0.007264	0.000443	0.000085	0.000075	0.000058
$n=4$	0	0.115204	−0.006607	0.000323	0.000087	0.000087	1	0.007209	0.000447	0.000057	0.000069	0.000060
$n=5$	0	0.115209	−0.006593	0.000271	−0.000001	0.000077	1	0.007221	0.000449	0.000075	0.000023	0.000064
$n=6$	0	0.115178	−0.006615	0.000328	0.000000	0.000029	1	0.007224	0.000463	0.000029	0.000041	0.000010
$n=7$	0	0.115141	−0.006552	0.000279	0.000050	0.000096	1	0.007243	0.000479	0.000096	0.000043	0.000066
$n=8$	0	0.115141	−0.006537	0.000269	0.000017	0.000080	1	0.007249	0.000487	0.000060	0.000027	0.000004
$n=9$	0	0.115197	−0.006587	0.000295	0.000051	0.000006	1	0.007232	0.000487	0.000090	0.000013	0.000013
$n=10$	0	0.115139	−0.006629	0.000292	0.000056	0.000072	1	0.007253	0.000421	0.000083	0.000013	0.000013
$n=11$	0	0.115140	−0.006616	0.000267	0.000010	0.000032	1	0.007232	0.000432	0.000045	0.000089	0.000070
$n=12$	0	0.115186	−0.006612	0.000271	−0.000002	0.000091	1	0.007271	0.000466	0.000051	0.000017	0.000062
$n=13$	0	0.115229	−0.006613	0.000276	0.000030	0.000007	1	0.007268	0.000450	0.000118	0.000040	0.000062
$n=14$	0	0.115145	−0.006592	0.000266	0.000066	0.000087	1	0.007235	0.000479	0.000049	0.000053	0.000083
$n=15$	0	0.115190	−0.006596	0.000280	0.000035	0.000042	1	0.007236	0.000466	0.000094	0.000042	0.000043
$n=16$	0	0.115142	−0.006628	0.000279	0.000022	0.000065	1	0.007296	0.000504	0.000066	0.000024	0.000076

4.3. Experimental Verification of Beam Fine-Tuning. The antenna structure and unit structure of the 1×16 linear arrays used to verify the growth gene algorithm are shown in Figure 4 and Figure 5. The antenna unit adopts a patch structure with a length of 37.26 mm and a width of 28 mm. The unit spacing is d, feeding from the coaxial line, and the feeding point is located 7 mm above the center of the patch antenna. The relative dielectric constant and thickness of substrate FR4 are 4.4 and 1.6 mm respectively. The working frequency of the antenna is 2.45 GHz, and the working air wavelength is $\lambda = 122$ mm. Figure 6(a) shows a flat-topped beam pattern of the 1×16 array antenna under the condition of array spacing $d = 0.5\lambda$. The amplitude and phase of the excitation corresponding to the flat-topped beam pattern are shown in Table 3.

As shown in Figure 6(a), the gain of the flat-topped beam pattern at $\theta = 18^{\circ}$ is 8dBi. In the experiment, the growth model trained by BTNet is used to fine-tune the gain at this angle by decreasing 3 dB and increasing 3 dB, respectively.

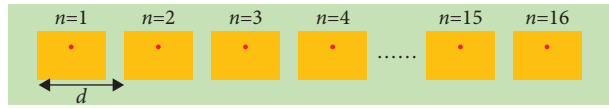

Figure 4: 1×16 linear array antenna.

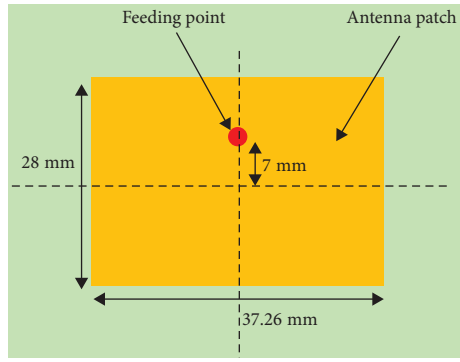

Figure 5: Patch antenna element.

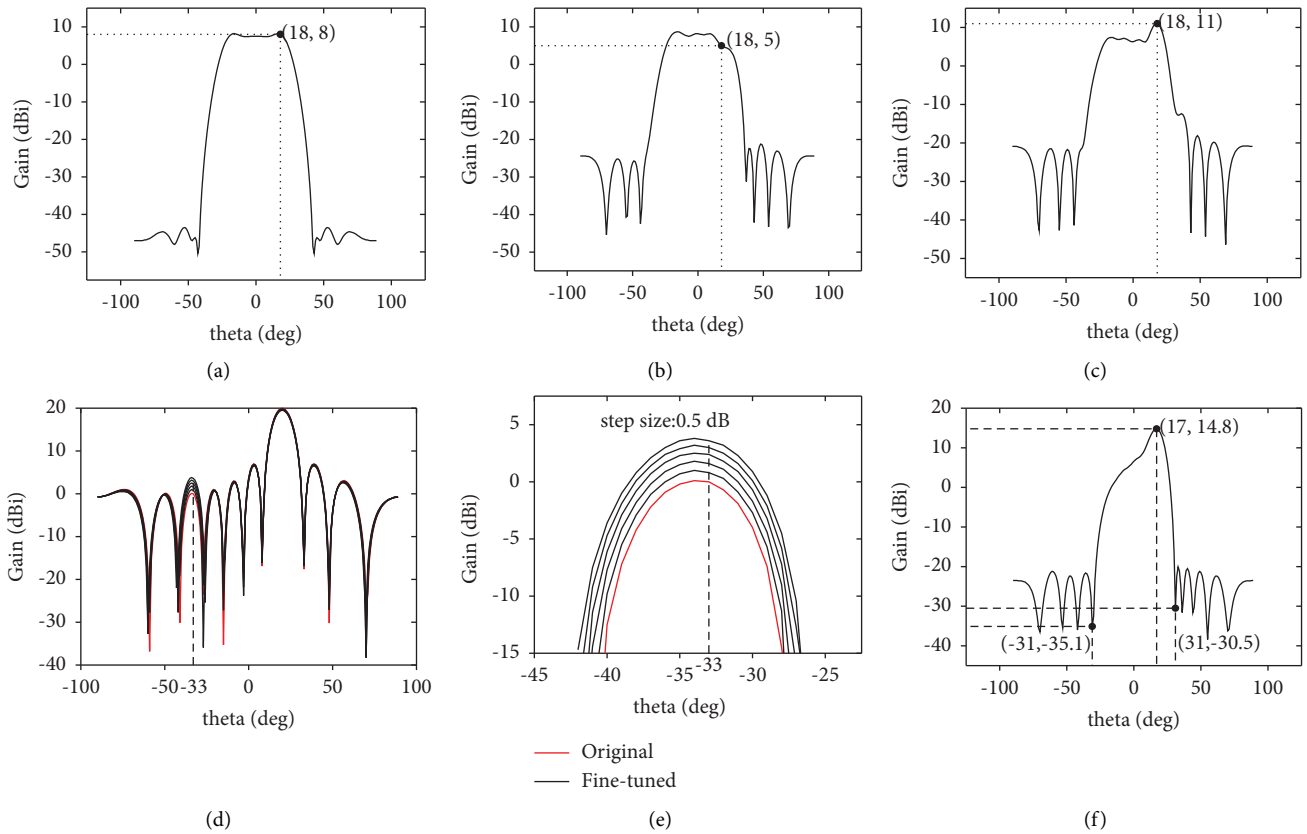

Figure 6: (a) The flat-topped beam pattern of the 1 × 16 antenna array under the condition of array spacing $d = 0.5\lambda$ and gain $G(\theta) = 8$ dBi at angle $\theta = 18^{\circ}$(b) the fine-tuned pattern has a gain of 5dBi at $\theta = 18^{\circ}$, which is 3 dB lower than the original flat-topped beam pattern; (c) the fine-tuned pattern has a gain of 11dBi at $\theta = 18^{\circ}$, which is 3 dB higher than the original flat-topped beam pattern. The random pattern of the 1 × 16 array antenna with array spacing $d = 0.5\lambda$ was taken as the initial pattern, and the growth model was used to carry out continuous fine-tuning of the side lobe gain at $\theta = -33^{\circ}$ with equal step size; (d) the general view of pattern tuning; (e) the detail view; (f) the cosecant squared pattern designed using the growth model, the coverage range of the formed pattern is -31°~31°, and the maximum gain direction is $\theta = 17^{\circ}$.

Table 3: The excitation corresponding to the flat-top beam.

Num	Amplitude (V)	Phase
1	0.80304	0deg
2	2.6395	0deg
3	3.6352	0deg
4	5.1516	−180deg
5	17.3215	180deg
6	6.1928	−180deg
7	28.7732	0deg
8	35.5739	0deg
9	19.9924	180deg
10	88.6058	−180deg
11	100	−180deg
12	57.2576	−180deg
13	14.716	180deg
14	0.68384	0deg
15	0.99359	0deg
16	0.14001	0deg

Table 4: The excitation after gain fine-tuning.

Num	Gain decreased by 3 dB		Gain increased by 3 dB	
	Amplitude	Phase	Amplitude	Phase
1	4.672 V	167.6122deg	8.4425 V	−9.5788deg
2	4.0511 V	−105.728deg	9.5885 V	34.7518deg
3	7.2696 V	−48.0397deg	7.8159 V	75.7985deg
4	2.2398 V	−100.0909deg	12.2195 V	165.3479deg
5	13.9121 V	167.903deg	22.9001 V	−169.7203deg
6	8.3639 V	138.906deg	9.7894 V	−128.0798deg
7	26.1478 V	7.2343deg	33.0671 V	−8.0232deg
8	32.3632 V	−3.1515deg	40.2185 V	3.5551deg
9	23.1728 V	−166.7736deg	18.0008 V	155.6163deg
10	90.0087 V	−177.3203deg	86.9729 V	176.1113deg
11	100V	179.685deg	100V	−179.5584deg
12	57.9555 V	175.2204deg	56.9624 V	−173.1756deg
13	18.6731 V	164.7761deg	12.2061V	−145.7311deg
14	4.7879 V	171.4933deg	8.3389 V	−6.8373deg
15	4.8673 V	−122.5324deg	8.3516 V	43.5287deg
16	5.5395 V	−74.6664deg	7.6825 V	102.9145deg

The corresponding excitation of each array element calculated by the growth model is shown in Table 4. The electromagnetic simulation software CST is used to simulate the excitation in Table 4, and the simulation results are shown in Figure 6(b) and Figure 6(c), respectively. It can be observed that the gains of the fine-tuned beam pattern at $\theta = 18^{\circ}$ are 5dBi and 11dBi, respectively, indicating that the growth model is very accurate for the fine-tuning pattern at any angle.

Table 5: Comparison of the growth model with different algorithms.

Year/Ref	Algorithm	Antenna array	Optimization objectives	Computational time
[2020]/[5]	Generic algorithm	10-circular	Beamforming	110 s
[2015]/[6]	Model order reduction	Rectangular	Beamforming	644 s
[2020]/[7]	Invasive weed optimization	10-circular	Beamforming	114.5 s
[2019]/[8]	Particle swarm optimization	8 × 1 Patch	Beamforming	31.7 s
[2019]/[8]	Firefly algorithm	8 × 1 Patch	Beamforming	55.4 s
[2019]/[8]	Taguchi's method	8 × 1 Patch	Beamforming	194.8 s
Proposed	Growth model	1 × 16-Linear	Gain fine-tuning	<10 ms

Figure 6(d) and Figure 6(e) show the results of continuously fine-tuning the side lobe gain of the 1×16 linear array antenna at $\theta = -33^{\circ}$ with 0.5 dB steps using the growth model. It can be found that using the growth model to fine-tune the side lobes of the antenna radiation pattern will not affect the gain of the main lobe of the pattern and vice versa. This conclusion is also verified in Figure 6(b) and Figure 6(c).

The fine-tuning of the gain at any angle by the above growth model takes an average of less than 10 ms, which verifies the high efficiency of the growth gene algorithm for fine-tuning patterns, which is convenient for real-time application in engineering. Table 5 shows the comparison of the computational times between the growth model and some beamforming algorithms in the literature. The growth model uses G (θ) (in dBi, the original gain at the angle θ) and s (in dB, the expected gain change at the angle θ) as inputs, where s is the step size of beam fine-tuning.

5. Experimental Verification of Cosecant Squared Beamforming

The beamforming of the array antenna can be achieved by fine-tuning the gain at multiple angles of the array radiation pattern using the growth model. In the experiment, the cosecant squared pattern with the pattern coverage range of -30° to 30° and the maximum gain direction of 16° to 18° is taken as the target, and the growth model is used to synthesize the beam pattern. The corresponding excitation of each element calculated by the growth model is shown in Table 6, and the radiation pattern simulated by using this excitation is shown in Figure 6(f).

As can be seen from Figure 6(f), the coverage range of the formed beam pattern is -31° to 31°, and the maximum gain direction is 17°, which well meets the design requirements of the cosecant squared pattern. Moreover, compared with the complex steps needed to be performed when using the optimization algorithm to perform the beamforming, the growth gene algorithm only needs to input the original gain $G^{ori}(\theta)$ and the expected gain change s at the corresponding angle θ into the growth model to calculate the excitation corresponding to the target pattern. It reduces the difficulty for antenna designers to implement high-precision beamforming.

Table 6: The excitation corresponding to the cosecant squared.

Num	Amplitude (V)	Phase
1	5.7913	126.8469deg
2	10.8134	−166.273deg
3	14.2734	−102.7381deg
4	22.9186	−40.2313deg
5	26.7167	14.9124deg
6	37.0708	87.1692deg
7	54.3422	138.6947deg
8	5.7913	126.8469deg
9	58.1583	−168.3989deg
10	75.653	−107.6462deg
11	100	−69.8895deg
12	90.6976	−45.7976deg
13	48.0395	−23.0731deg
14	8.2269	47.2888deg
15	16.8154	166.8038deg
16	13.9234	−158.1047deg

6. Conclusions

In this paper, a beamforming algorithm, called the growth gene algorithm, which imitates plant growth genes, is proposed. By establishing the growth model, the algorithm can fine-tune the gain of the antenna radiation pattern at any angle to achieve high efficiency and accurate beamforming of the target pattern. By fine-tuning multiple angles of the radiation pattern of 1×16 linear arrays, the cosecant square beamforming with a coverage range of -31° to 31° and maximum gain direction of 17° is realized. The process of fine-tuning the gain of the growth gene algorithm only involves simple matrix multiplication and addition operations, so the complexity of achieving precise beamforming is low. The growth model is only related to the gain value before and after the gain fine-tuning and the angle of the gain fine-tuning, but not to the array spacing and the array element radiation pattern. Therefore, these gene parameters can be applied to other 1×16 linear array antennae. More importantly, the growth gene algorithm proposed in this paper can be easily extended to the beamforming of area array antennas.

Data Availability

The data used to support the findings of this study are included in the article.

Conflicts of Interest

The authors declare that they have no conflicts of interest.

Acknowledgments

This work was supported by the Fundamental Research Funds for the Central Universities (No. 2019XD-A07), the National Natural Science Foundation of China (No. 62271063), the Director Fund of Beijing Key Laboratory of Space Ground Interconnection and Convergence, and the National Key Laboratory of Science and Technology on Vacuum Electronics.

References

[1] A. K. Pandey, "Phased Array Antenna with Beamforming Network for 5G mmWave Communication System," in *Proceedings of the 2020 50th European Microwave Conference (EuMC)*, pp. 364–367, Utrecht, Netherlands, January 2021.

[2] G. Zhou, "Energy efficiency beamforming design for UAV communications with broadband hybrid polarization antenna arrays," *IEEE Access*, vol. 7, pp. 34521–34532, 2019.

[3] A. H. Hussein, H. S. Fouda, H. H. Abdullah, and A. A. M. Khalaf, "A highly efficient spectrum sensing approach based on antenna arrays beamforming," *IEEE Access*, vol. 8, pp. 25184–25197, 2020.

[4] H. Li, Y. Chen, and S. Yang, "Harmonic beamforming in antenna array with time-modulated amplitude-phase weighting technique," *IEEE Transactions on Antennas and Propagation*, vol. 67, no. 10, pp. 6461–6472, 2019.

[5] A. Hamza and H. Attia, "Fast beam steering and null placement in an adaptive circular antenna array," *IEEE Antennas and Wireless Propagation Letters*, vol. 19, no. 9, pp. 1561–1565, 2020.

[6] Y. Sato, F. Campelo, and H. Igarashi, "Fast shape optimization of antennas using model order reduction," *IEEE Transactions on Magnetics*, vol. 51, no. 3, pp. 1–4, Article ID 7204304, 2015.

[7] G. G. Roy, S. Das, P. Chakraborty, and P. N. Suganthan, "Design of non-uniform circular antenna arrays using a modified invasive weed optimization algorithm," *IEEE Transactions on Antennas and Propagation*, vol. 59, no. 1, pp. 110–118, 2011.

[8] L. A. Greda, A. Winterstein, D. L. Lemes, and M. V. T. Heckler, "Beamsteering and beamshaping using a linear antenna array based on particle swarm optimization," *IEEE Access*, vol. 7, pp. 141562–141573, 2019.

[9] R. G. Ayestaran, F. Las-Heras, and L. F. Herran, "High-accuracy neural-network-based array synthesis including element coupling," *IEEE Antennas and Wireless Propagation Letters*, vol. 5, pp. 45–48, 2006.

[10] R. G. Ayestaran, F. Las-Heras, and L. F. Herran, "Neural modeling of mutual coupling for antenna array synthesis," *IEEE Transactions on Antennas and Propagation*, vol. 55, no. 3, pp. 832–840, 2007.

[11] J. H. Kim and S. W. Choi, "A deep learning-based approach for radiation pattern synthesis of an array antenna," *IEEE Access*, vol. 8, pp. 226059–226063, 2020.

[12] R. Lovato and X. Gong, "Phased antenna array beamforming using convolutional neural networks," in *Proceedings of the 2019 IEEE International Symposium on Antennas and Propagation and USNC-URSI Radio Science Meeting*, pp. 1247-1248, Atlanta, GA, USA, July 2019.

[13] R. G. Ayestaran and F. Las-Heras, "Obstacle modeling in array synthesis using neural networks," *IEEE Transactions on Antennas and Propagation*, vol. 54, no. 8, pp. 2420–2424, 2006.

[14] Y. Gong, S. Xiao, and B.-Z. Wang, "An ANN-based synthesis method for nonuniform linear arrays including mutual coupling effects," *IEEE Access*, vol. 8, pp. 144015–144026, 2020.

[15] H. Yang, J. Jee, G. Kwon, and H. Park, "Deep transfer learning-based adaptive beamforming for realistic communication channels," in *Proceedings of the 2020 International Conference on Information and Communication Technology Convergence*, pp. 2162–1233, Jeju, Korea, December 2020.

[16] J. L. Zhang, W. G. Wan, Z. Zhan-Qi, X. Gan, and X. Y. Zhu, "Research on X band extended cosecant squared beam synthesis of micro-strip antenna arrays using genetic algorithm," *Acta Physica Sinica*, vol. 64, no. 11, Article ID 110504, 2015.

[17] D. Kingma and J. Ba, "Adam: A Method for Stochastic Optimization," ICLR, San Diego, pp. 2162–1233, Article ID 1412.6980, 2015.

[18] S. J. Pan and Q. Yang, "A survey on transfer learning," *IEEE Transactions on Knowledge and Data Engineering*, vol. 22, no. 10, pp. 1345–1359, 2010.